

# Growth and investigation of Argon thin films adsorbed on graphite by means of Ultrafast Electron Diffraction

Présentée le 27 avril 2023

Faculté des sciences de base  
Laboratoire pour la microscopie et la diffusion d'électrons  
Programme doctoral en physique

pour l'obtention du grade de Docteur ès Sciences

par

**Paolo USAI**

Acceptée sur proposition du jury

Prof. O. Yazyev, président du jury  
Prof. F. Carbone, directeur de thèse  
Prof. G. Mancini, rapporteuse  
Prof. J. Weissenrieder, rapporteur  
Prof. F. Stellacci, rapporteur



*To my dearest*



*I don't care what anything was designed to do,  
I care about what it can do.*  
— Gene Kranz (Apollo 13)



# Acknowledgements

Firstly, I would like to thank Prof. Fabrizio Carbone for giving me the chance of working in his group and trusting me with that delicate setup. I hope your faith in my skills has been repaid and I can't thank you enough for your guidance and advice, especially during the most difficult moments of this crazy project.

A huge thank you to Dr. Siham Benhabib. I know that without you this project wouldn't have had a very high chance of success. I thank you for sharing your knowledge and expertise, for all the good moments we worked together, the struggles with the experiment, the crazy ideas we tested and all the problem-solving involved in the experimental development, on top of your patience with me and your help for anything I ever needed it for.

I thank Rémi for working together on the Argon project, for your help and contribution with discussions, simulations and also the experimental work with the optics and the UED itself.

A thank you to Benoit, for working together on the Magnetite project, on top of all the discussions and exchanges and funny moments during this PhD.

A special thank you to Prof. Giulia Mancini, for building this setup from the ground up, for all the explanations on how it works and also for giving me the opportunity to work on other projects involving other techniques. I hope that when you look at the setup after I put my hands on it you won't think: *"Look how they massacred my boy"*.

I thank Dr. Malte Oppermann and Dr. Ahmad Ajdar for taking care of the laser and making all this work possible.

I thank Dr. Luca Piazza and Dectris for the opportunity to work together and adapt the new detector to this particular setup.

A thank you to Dr. Thomas La Grange for your suggestions and invaluable expertise in electron techniques, diffraction, and many other subjects. And how can I not mention the wonderful grillades and astrophotography?

I would like to thank Dr. Francesco Pennacchio and Prof. Giovanni Maria Vanacore (taaac) for introducing me to the lab and teaching me the basics of this technique, their upgrades to the setup, their suggestions, and advice.

A special thank you to the members of the Office who, apart from being exceptional colleagues, have been also wonderful friends.

## Acknowledgements

---

To Simone, for being part of the non-serious side of the room, for the interminable discussions ranging from physics to philosophy to the animal world, for sharing so many thoughts instead of working, and participate in the highest moments of popular culture.

To Francesco, for being the inspiring muse of many songs and poems, and other branches of human culture, from culinary art to ornithology. And as well for your expertise in physics and data analysis and programming.

To Veronica, for always being patient with me and all my questions, and also for showing me, in a scientific and reproducible way, that whenever things are not going well, they can always get worse!

I would like to thank all the other LUMES members: Ivan, Alexey, Phoebe, Bruce, Kjeld, Le, Lukas, Daniel, Paolo, Michele, and Samuele for all your support, the exchange of ideas and experience, sharing of knowledge and all the patience you showed me. I know I'm not easy to deal with.

Thank you, Leonor, for always being available for a chat and discussing more life-related problems, on top of all the support you gave to this group.

I thank the entire LUMES group for everything and all the fun we shared during events like retreats and conferences, as well as more casual sorties and daily life at EPFL.

I want to thank Oliviero for all our cooperation, without you I may have never discovered Python and all its magic. Michele, for your diverse knowledge and your counsel on how to tackle various problems.

Thank you to Prof. Majed Chergui and the LSU group for allowing me to work together in the labs and for their help on a multitude of different subjects.

A deep thank you to my family: you believed in me and supported me from the second I decided to leave you and my motherland to start this career, through the good and bad moments, despite the distance and not enough occasions to rejoin. I hope I made you proud.

To Karin, for bringing new joy to my life, for sharing so many adventures together, for supporting me through the most difficult times and for being always there for me, even when I don't expect you to.

I don't know what would have happened if I had chosen a different path, but I know that if I achieved what I did, and if I am who I am, as a human and as a scientist, I owe it in great part to you.

Thank you all.



# Abstract

Starting from our big universe to the microscopic world, phase transitions play an important role in nature. Just after the Big Bang our universe experienced multiple phase transitions, from high-temperature plasma to the matter we know today.

Phase transitions involve many properties, including mechanical, thermal, optical, electric, and magnetic, which represent the bedrock of our scientific and technological advances. Understanding the phase transitions and revealing their mechanism is a key step to controlling them and manipulating the desired properties of matter.

It has been demonstrated that the dimensionality of a system is a crucial parameter in the involvement of phase transformations. The 3D phase transformations are classified into two categories: discontinuous ones, called first-order, and continuous ones, called second-order. In contrast to 3D systems, 2D ones admit intermediate phases which are not present in purely 3D systems, for example, a mixed state between solid and liquid, which is known by the name of hexatic phase.

In this thesis, two systems with different dimensionality, 2D and 3D, are studied.

In the 2D system, the phase diagram of a prototypical 2D material, which is argon adsorbed on graphite, is investigated. This system exhibits a complex phase diagram of pressure vs. temperature which is explored at low temperatures and low pressures constructing a deposition kinetic diagram. The presence of a mixed configuration exhibiting characters common to hexatic and liquid crystal configurations is hypothesized. The melting process of this material is explored in two ways: quasi-adiabatic and out-of-equilibrium driven by ultrafast laser pulses. The ultrafast dynamics in a timescale of picoseconds revealed an expansion of the argon films as a reaction to the dynamics of the substrate (graphite) photoexcited at 1.55 eV.

In the 3D case, the first-order transition in magnetite, which involves structural and electronic transitions, the so-called Verwey transition is investigated. Following the transition from cubic to monoclinic in the quasi-adiabatic regime (temperature dependence) allowed tracking the symmetry of the order parameter involved in this structural transition. Photoexciting magnetite with two different photoexcitations, 1.55 and 3.10 eV, in the monoclinic phase below Verwey temperature, revealed two different processes, each one involving metastable intermediate states that are thermodynamically inaccessible. The photoexcitation at 1.55 eV promoted a phase separation

## Abstract

---

between cubic metallic islands and monoclinic insulating zones. The photoexcitation at 3.10 eV reinforced the monoclinic insulating state by optimizing the long-range network of the trimerons.

These investigations are conducted by means of Ultrafast Electron Diffraction (UED), thanks to the capabilities of this technique of probing the structural properties of crystals based on diffraction phenomena, with femtosecond ( $10^{-15}$  s) and atomic ( $10^{-10}$  m) temporal and spatial resolution.

The results in this thesis validate the capability of this technique of studying complex phenomena, such as phase transitions, in both regimes, thermodynamic equilibrium and out-of-equilibrium.

# Zusammenfassung

Angefangen von unserem großen Universum hinunter bis hin zur mikroskopischen Welt spielen Phasenübergänge in der Natur eine wichtige Rolle. Unmittelbar nach dem Urknall ereigneten sich in unserem Universum mehrere Phasenübergänge, vom Hochtemperaturplasma bis zur Materie, die wir heute kennen. Phasenübergänge involvieren viele Eigenschaften, darunter mechanische, thermische, optische, elektrische und magnetische, die die Grundlage für unsere wissenschaftlichen und technologischen Fortschritte bilden. Das Verständnis der Phasenübergänge und die Aufdeckung ihrer Mechanismen ist ein wichtiger Schritt, um sie zu kontrollieren und die gewünschten Eigenschaften der Materie zu manipulieren. Man konnte zeigen, dass die Dimensionalität eines Systems ein entscheidender Parameter im Prozess von Phasenübergängen ist. Die 3D-Phasenübergänge werden in zwei Kategorien eingeteilt: diskontinuierliche, genannt erste Ordnung, und kontinuierliche, genannt zweite Ordnung. Im Gegensatz zu 3D-Systemen sind in 2D-Systemen Zwischenphasen möglich, die in reinen 3D-Systemen nicht vorkommen, z. B. ein Mischzustand zwischen fest und flüssig, der unter dem Namen hexatische Phase bekannt ist. In dieser Arbeit werden zwei Systeme mit unterschiedlicher Dimensionalität, 2D und 3D, untersucht. Als 2D-System wird das Phasendiagramm eines prototypischen 2D-Materials: Argonadsorbiert auf Graphit, ermittelt. Dieses System zeigt ein komplexes Phasendiagramm als Funktion von Druck und Temperatur, das bei niedriger Temperatur und niedrigem Druck untersucht wurde, indem ein Diagramm der Depositionskinetik erstellt wird. Es wird die Hypothese aufgestellt, dass eine gemischte Konfiguration existiert, die gemeinsame Merkmale von hexatischen und Flüssigkristallkonfigurationen aufweist. Der Schmelzprozess von Argon auf Graphit wird auf zwei Arten untersucht: quasi-adiabatisch und außerhalb des Gleichgewichts, angeregt durch ultraschnelle Laserpulse. Die ultraschnelle Dynamik in einer Zeitskala von Pikosekunden zeigt eine Ausdehnung der Argonfilme als Reaktion auf die Dynamik des Substrats (Graphit), das bei 1.55 eV photoangeregt wurde. Im 3D-Fall wird der Übergang erster Ordnung in Magnetit untersucht, der strukturelle und elektronische Übergänge beinhaltet, den so genannten Verwey-Übergang. Die Verfolgung des Übergangs von kubisch zu monoklin im quasi-adiabatischen Bereich (Temperaturabhängigkeit) ermöglicht es, die Symmetrie des an diesem Strukturübergang beteiligten Ordnungsparameters zu verfolgen.

## Zusammenfassung

---

Die Photoanregung von Magnetit mit zwei verschiedenen Photoanregungen, 1.55 und 3.10 eV, in der monoklinen Phase unterhalb der Verwey-Temperatur, offenbart zwei verschiedene Prozesse, die jeweils metastabile Zwischenzustände einschließen, die thermodynamisch unzugänglich sind. Die Photoanregung bei 1.55 eV erzeugt eine Phasentrennung zwischen kubischen metallischen Inseln innerhalb monoklinen isolierenden Zonen. Die Photoanregung bei 3.10 eV verstärkt den monoklinen isolierenden Zustand durch Optimierung des weitreichenden Netzwerk der Trimerone. Diese Untersuchungen wurden mit Hilfe der ultraschnellen Elektronenbeugung (UED) durchgeführt, da diese Technik die strukturellen Eigenschaften von Kristallen auf der Grundlage von Beugungsphänomenen mit einer zeitlichen und räumlichen Auflösung von Femtosekunden ( $10^{-15}$  s) und atomarer Distanz ( $10^{-10}$  m) untersuchen kann. Die Ergebnisse dieser Arbeit bestätigen die Fähigkeit dieser Technik, komplexe Phänomene wie Phasenübergänge in beiden Regimen, d. h. im thermodynamischen Gleichgewicht und außerhalb des Gleichgewichts, zu untersuchen.

# Résumé

De l'univers infini au monde microscopique, les transitions de phase jouent un rôle important dans la nature. Juste après le Big Bang, notre univers a connu de multiples transitions de phase, du plasma à haute température à la matière que nous connaissons aujourd'hui.

Les transitions de phase impliquent de nombreuses propriétés, notamment mécaniques, thermiques, optiques, électriques et magnétiques, qui constituent le fondement de nos avancées scientifiques et technologiques. Comprendre les transitions de phase et révéler leur mécanisme est une étape clé pour les contrôler et manipuler les propriétés souhaitées de la matière.

Il a été démontré que la dimensionnalité d'un système est un paramètre crucial dans le processus des transformations de phase. Les transformations de phase en 3D sont classées en deux catégories : les transformations discontinues, dites de premier ordre, et les transformations continues, dites de second ordre. Contrairement aux systèmes 3D, les systèmes 2D admettent des phases intermédiaires qui ne sont pas présentes dans un système purement 3D, par exemple un état mixte entre solide et liquide, connu sous le nom de phase hexatique.

Dans cette thèse, deux systèmes de dimensionnalité différente, 2D et 3D, sont étudiés. Dans le système 2D, le diagramme de phase d'un matériau 2D prototypique, l'argon adsorbé sur le graphite, est étudié. Ce système présente un diagramme de phase pression versus température complexe qui est exploré à basse température et à basse pression en construisant un diagramme cinétique de dépôt. L'hypothèse de la présence d'une configuration mixte présentant des caractéristiques communes aux configurations hexatiques et aux cristaux liquides est avancée. Le processus de fusion de ce matériau est exploré de deux manières : quasi-adiabatique et hors équilibre sous l'effet d'impulsions laser ultrarapides. La dynamique ultrarapide sur une échelle de temps de l'ordre de la picoseconde a révélé une expansion des films d'argon en réaction à la dynamique structurelle du substrat (graphite) photoexcité à 1,55 eV.

Dans le cas 3D, la transition du premier ordre dans la magnétite, qui implique des transitions structurelles et électroniques, appelé transition de Verwey, est étudiée. Le suivi de la transition structurelle passant d'une phase cubique à phase monoclinique dans le régime quasi-adiabatique (dépendance en température) a permis de déterminer

## Résumé

---

la symétrie du paramètre d'ordre impliqué dans cette transition structurale. La photoexcitation de la magnétite avec deux énergies de photoexcitation différentes, 1,55 et 3,10 eV, dans la phase monoclinique en dessous de la température de Verwey, a révélé deux processus dynamiques différents, chacun impliquant des états intermédiaires métastables qui sont thermodynamiquement inaccessibles. La photoexcitation à 1,55 eV a favorisé une séparation de phase induisant des îlots métalliques cubiques immergés dans des zones isolantes monocliniques. La photoexcitation à 3,10 eV a renforcé l'état isolant monoclinique en optimisant le réseau à longue portée des trimérons. Ces recherches sont menées au moyen de la diffraction électronique ultrarapide (UED), grâce aux capacités de cette technique à sonder les propriétés structurales des cristaux sur la base des phénomènes de diffraction, avec une résolution temporelle et spatiale de l'ordre de la femtoseconde ( $10^{-15}$  s) et de l'atome ( $10^{-10}$  m). Les résultats de cette thèse valident la capacité de cette technique à étudier des phénomènes complexes, tels que les transitions de phase, dans les deux régimes, à l'équilibre thermodynamique et hors équilibre.

## Sommario

Dal nostro grande universo al mondo microscopico, le transizioni di fase svolgono un ruolo importante in natura. Subito dopo il Big Bang, il nostro universo ha sperimentato molteplici transizioni di fase, dal plasma ad alta temperatura alla materia che conosciamo oggi.

Le transizioni di fase coinvolgono molte proprietà, tra cui quelle meccaniche, termiche, ottiche, elettriche e magnetiche, che rappresentano la base dei nostri progressi scientifici e tecnologici. Comprendere le transizioni di fase e svelarne il meccanismo è un passo fondamentale per controllarle e manipolare le proprietà della materia desiderate.

È stato dimostrato che la dimensionalità di un sistema è un parametro cruciale nel processo delle trasformazioni di fase. Le trasformazioni di fase 3D sono classificate in due categorie: quelle discontinue, dette del primo ordine, e quelle continue, dette del secondo ordine. A differenza dei sistemi 3D, quelli 2D ammettono fasi intermedie che non sono presenti nei sistemi puramente 3D, ad esempio uno stato misto tra solido e liquido, noto con il nome di fase esatica.

In questa tesi vengono studiati due sistemi a diversa dimensionalità, 2D e 3D.

Nel sistema 2D, viene studiato il diagramma di fase di un materiale 2D prototipico, l'argon adsorbito sulla grafite. Questo sistema presenta un complesso diagramma di fase pressione/temperatura che viene esplorato a basse temperature e basse pressioni costruendo un diagramma della cinetica di deposizione. Si ipotizza la presenza di una configurazione mista che presenta caratteri comuni alle configurazioni esatiche e ai cristalli liquidi. Il processo di fusione di questo materiale viene esplorato in due modi: quasi-adiabatico e fuori equilibrio guidato da impulsi laser ultraveloci. La dinamica ultraveloce in tempi di picosecondi ha rivelato un'espansione dei film di argon come reazione alla dinamica del substrato (grafite) fotoeccitato a 1,55 eV.

Nel caso 3D, viene studiata la transizione del primo ordine nella magnetite, che coinvolge transizioni strutturali ed elettroniche, la cosiddetta transizione di Verwey. Seguire la transizione da cubico a monoclino nel regime quasi-adiabatico (dipendenza dalla temperatura) ha permesso di tracciare la simmetria del parametro d'ordine coinvolto in questa transizione strutturale. La fotoeccitazione della magnetite con due diverse fotoeccitazioni, a 1,55 e 3,10 eV, nella fase monoclinica al di sotto della

## Sommario

---

temperatura di Verwey, ha rivelato due diversi processi, ciascuno dei quali coinvolge stati intermedi metastabili che sono termodinamicamente inaccessibili. La fotoeccitazione a 1,55 eV ha promosso una separazione di fase tra isole metalliche cubiche e zone isolanti monocliniche. La fotoeccitazione a 3,10 eV ha rafforzato lo stato isolante monoclinico ottimizzando il reticolo a lungo raggio dei trimeroni.

Queste indagini sono state condotte per mezzo della diffrazione elettronica ultraveloce (UED), grazie alle capacità di questa tecnica di sondare le proprietà strutturali dei cristalli sulla base dei fenomeni di diffrazione, con risoluzione temporale e spaziale di femtosecondi ( $10^{-15}$  s) e atomica ( $10^{-10}$  m).

I risultati di questa tesi convalidano la capacità di questa tecnica di studiare fenomeni complessi, come le transizioni di fase, in entrambi i regimi, equilibrio termodinamico e fuori equilibrio.



# Contents

<b>Acknowledgements</b>	<b>i</b>
<b>Abstract (English, Deutsch, Français, Italiano)</b>	<b>iii</b>
<b>1 Ultrafast Electron Diffraction</b>	<b>1</b>
1.1 Principles of diffraction . . . . .	1
1.2 Electron diffraction . . . . .	4
1.3 Ultrafast Electron Diffraction . . . . .	6
1.4 The UED at LUMES . . . . .	8
1.5 Upgrades to the setup . . . . .	9
1.5.1 Detector upgrade . . . . .	9
1.5.2 Improvements to the DC gun . . . . .	11
1.5.3 Gas injection system . . . . .	13
1.5.4 Cryostat and temperature sensors . . . . .	13
1.5.5 Heating control . . . . .	13
1.5.6 I/O interfaces . . . . .	14
1.5.7 Software . . . . .	14
<b>2 Argon thin films</b>	<b>17</b>
2.1 Introduction . . . . .	17
2.2 Previous works on Argon films adsorbed on graphite . . . . .	20
2.3 Experimental procedure . . . . .	23
2.3.1 Characterization of the substrate . . . . .	23
2.3.2 Calibration of the diffraction patterns . . . . .	25
2.3.3 Deposition of Argon . . . . .	27
2.3.4 Melting of the Argon films . . . . .	27
2.4 Results and discussion . . . . .	28
2.4.1 Deposition process . . . . .	28
2.4.2 Determination of the structure of the adsorbate . . . . .	28
2.5 The possibility of the hexatic phase . . . . .	32
2.6 Deposition kinetics diagram of Argon films . . . . .	33

## Contents

---

2.7	Thermodynamic melting process . . . . .	35
2.8	Conclusions . . . . .	36
2.9	Perspectives and outlook . . . . .	37
<b>3</b>	<b>Ultrafast dynamics of Ar films on graphite</b>	<b>39</b>
3.1	Introduction . . . . .	39
3.2	Experimental procedure . . . . .	39
3.2.1	Spatial and temporal overlap determination . . . . .	40
3.3	Ultrafast dynamics of graphite . . . . .	43
3.4	Ultrafast dynamics of argon thin films . . . . .	45
3.5	Conclusions . . . . .	49
3.6	Outlook . . . . .	49
<b>4</b>	<b>Ultrafast generation of hidden phases via energy-tuned electronic photoex-</b>	
	<b>citation in magnetite</b>	<b>51</b>
4.1	Introduction . . . . .	51
4.2	Verwey transition in equilibrium conditions . . . . .	54
4.3	Verwey transition under out-of-equilibrium conditions . . . . .	59
4.4	Conclusions . . . . .	63
<b>A</b>	<b>Software</b>	<b>65</b>
A.1	Acquisition software . . . . .	65
A.2	Data analysis software . . . . .	68
	<b>Bibliography</b>	<b>83</b>
	<b>Curriculum Vitae</b>	<b>85</b>

# 1 Ultrafast Electron Diffraction

In this chapter, we will illustrate the basic principles of diffraction, as well as Ultrafast Electron Diffraction and its implementation at LUMES.

## 1.1 Principles of diffraction

Let's consider a plane wave of wavelength  $\lambda$  impinging on a crystal: if  $\lambda$  is comparable to the interatomic distance  $d$  every atom hit by the radiation can be considered as a scatterer thus emitting a spherical wave centered on the atom. A representation is depicted in Figure 1.1. These spherical waves propagate in space and can interfere constructively or destructively resulting in a diffraction pattern. The pattern is characteristic of the crystal structure taken into consideration and holds information about its unit cell, lattice parameters, atoms distribution, *etc...*

If we consider a mono-crystalline specimen the diffraction pattern will exhibit sharp and well-defined features called Bragg peaks, each of them representing the interference of all the atomic planes in the same direction. If, instead, we consider a powder where all grains are microscopic monocrystals their random orientation to the incident radiation will produce concentric cones of constructive interference. Projected on a flat screen perpendicular to their propagation direction, these cones originate concentric rings called Debye-Scherrer rings, see Figure 1.6g.

The conditions for which the diffraction occurs can be visualized using the geometrical approach of Henry and Lawrence Bragg, developed in 1913 [1]: when the difference in the pathway between the incident wave and the exit wave diffracted by the same family of lattice planes is an integer multiple of the wavelength the interference is constructive. This concept is visualized in Figure 1.2 for the constructive and destructive cases respectively. This condition can be described by a mathematical

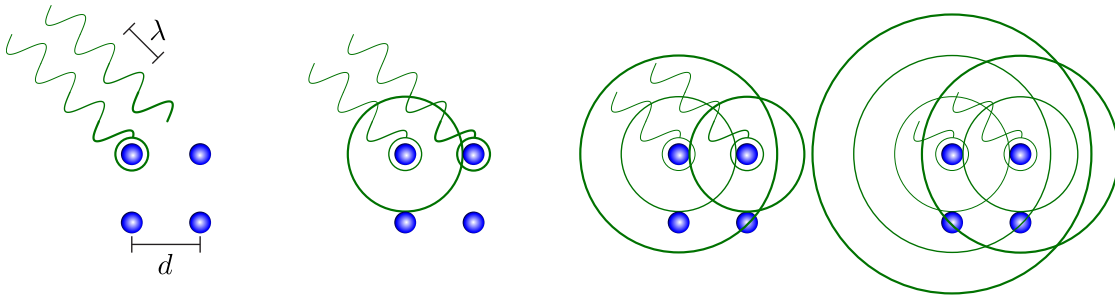


**Figure 1.1:** Schematic of spherical waves originated by the interaction between matter and radiation of wavelength  $\lambda$  comparable to the interatomic distances in the investigated sample. Reprinted with modification from Christophe Dang Ngoc Chan, under GNU Free Documentation Licence.

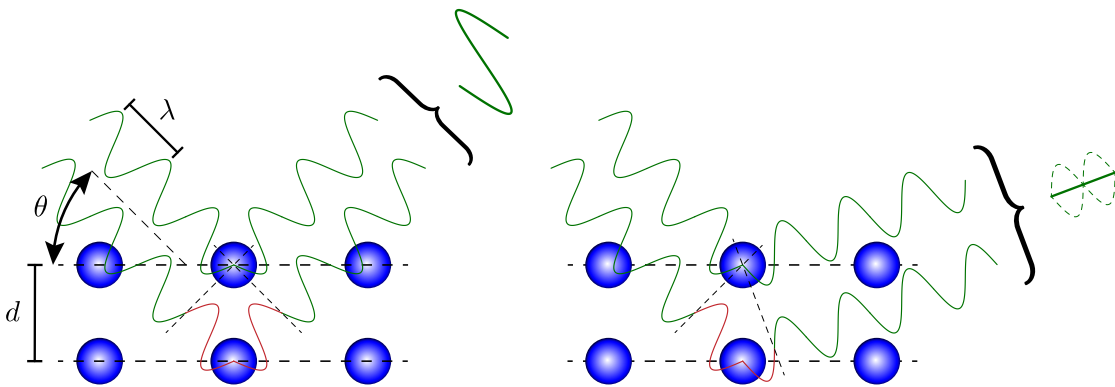


**Figure 1.2:** Geometrical representation of Bragg diffraction for an incident wavelength  $\lambda$  and lattice spacing  $d$ . The two situations represent constructive and destructive interference respectively. Reprinted with modification from Christophe Dang Ngoc Chan, under GNU Free Documentation Licence.

relation, called the Bragg condition:

$$2d \sin \theta = n\lambda \quad (1.1)$$

where  $d$  is the spacing between lattice planes belonging to the same family,  $\theta$  is the angle between the incident wave and the family of planes,  $\lambda$  is the wavelength and  $n$  is an integer number defining the order of diffraction.

The occurrence and angular distribution of diffraction peaks depend on the disposition of the atoms in the crystal. The minimum repeated units (can be atoms but also groups of atoms) are arranged in a periodic array called the Bravais lattice which represents only the geometry of the crystal, regardless of the repeated units. One way to define the Bravais lattice is to consider all the points with a position vector  $\mathbf{R}$  of the form  $\mathbf{R} = n_1 \mathbf{a}_1 + n_2 \mathbf{a}_2 + n_3 \mathbf{a}_3$ , where  $n_1$ ,  $n_2$  and  $n_3$  are integers and  $\mathbf{a}_1$ ,  $\mathbf{a}_2$  and  $\mathbf{a}_3$  are three vectors all not in the same plane called primitive vectors [2].

While the real space describes the position of the units, a lattice describing their periodicity can be constructed by vectors  $\mathbf{K} = k_1 \mathbf{b}_1 + k_2 \mathbf{b}_2 + k_3 \mathbf{b}_3$  satisfying  $e^{i\mathbf{K}\cdot\mathbf{R}}$ , where again  $k_1, k_2$  and  $k_3$  are integers and  $\mathbf{b}_1, \mathbf{b}_2$  and  $\mathbf{b}_3$  are the primitive vectors of the so-called reciprocal lattice.

The incident radiation along a direction  $\hat{\mathbf{n}}$  can be expressed as a wavevector  $\mathbf{k} = \frac{2\pi}{\lambda} \hat{\mathbf{n}}$ . Calling  $\mathbf{d}$  the vector separating two lattice points scattering the incident radiation  $\mathbf{k}, \mathbf{k}'$  the scattered wave, the Bragg condition can be rewritten as:

$$\mathbf{d} \cdot (\mathbf{k} - \mathbf{k}') = 2\pi m \quad (1.2)$$

where  $m$  is an integer. The lattice points are separated by the lattice vectors  $\mathbf{R}$ , so Equation 1.2 will become:

$$\mathbf{R} \cdot (\mathbf{k} - \mathbf{k}') = 2\pi m \quad (1.3)$$

which can be written in an equivalent form as  $e^{i(\mathbf{k}' - \mathbf{k})\cdot\mathbf{R}} = 1$ . Again this implies that, for constructive interference,

$$(\mathbf{k}' - \mathbf{k}) = \Delta\mathbf{k} = \mathbf{R} \quad (1.4)$$

called the Laue condition. A useful way to visualize this condition is the Ewald construction, Figure 1.3

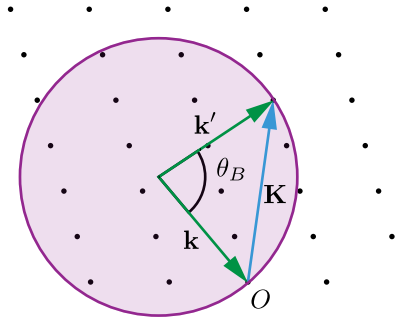


**Figure 1.3:** Scheme of the Ewald construction. Considering a reciprocal lattice point  $O$ , a sphere of radius  $k$  is drawn so  $O$  lies on the circumference. Given a reciprocal lattice vector  $\mathbf{K}$ , diffraction peaks will be observed only if the point corresponding to  $\mathbf{K}$  lies on the circumference. Image adapted from [2].

To show the equivalence between the Bragg and Laue formulations it is sufficient to consider the following relationships:  $|\vec{g}| = 2\pi/d$ ,  $\Delta\vec{K} = 2k \sin\theta_B$  and  $|\vec{k}| = 2\pi/\lambda$ . Once applied the substitution the equivalence is verified.

## 1.2 Electron diffraction

The diffraction condition requires that  $\lambda$  must be comparable to the atomic spacing, which is in the range of 0.1-10 Å. X-rays, with their wavelength in the range of 10-100 Å, can be used for this purpose in conditions of grazing incidence since their penetration through several  $\mu\text{m}$  at higher angles probes mainly the bulk of the substrate and constitutes an important limitation. Alternatively, other sources for the incident radiation can be used, for example, particles such as neutrons and electrons with a de Broglie wavelength tunable with their kinetic energy and smaller than the typical atomic spacing. The penetration depth of neutrons is even longer than the one of x-rays so they may not be the first choice for a surface-sensitive experiment. On the other hand, the penetration depth of electrons can be estimated considering the mean free path (IMFP) of the electrons in the material, which is in the range of 1-10 nm for energies below 50 keV. Considering that, for the energy of tens of keV, the wavelength of an electron is small enough so the Bragg condition is verified for small angles, a few degrees, the probed depth of the specimen can be estimated as the product of the IMFP and the sine of the angle of incidence respect to the surface. Wavelength and IMFP (calculated using the parameters in [3]) are shown in Figure 1.4. For an energy of 30 keV, the wavelength is approximately 0.07 Å and the IMFP is 9.35 nm. Considering an angle of incidence of 4 degrees and that the electrons need to get out of the material, the probed depth will be approximately 0.3 nm, hence the topmost layer of atoms will be probed. With this scale of energy and diffraction condition, this technique is called Reflection High Energy Electron Diffraction (RHEED) and it has been particularly useful for the growth of thin films with different methods [4–7].

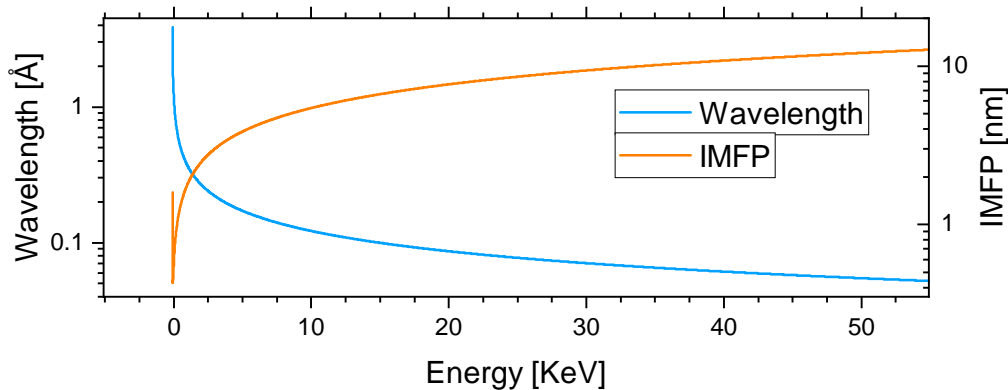


**Figure 1.4:** Blue: the de Broglie wavelength of an electron with different kinetic energies; Orange: inelastic mean free path of an electron through a material.

The intensity of a Bragg peak is defined as:

$$I \propto |F_{hkl}|^2 \quad (1.5)$$

where  $F_{hkl}$  is the structure factor:

$$F_{hkl} = \sum_1^n e^{2\pi i(hx+ky+lz)} f_n \quad (1.6)$$

with  $n$  the number of atoms in the unit cell,  $x$ ,  $y$ , and  $z$  the fractional coordinates of the atoms in the unit cell,  $h$ ,  $k$ ,  $l$  the indexes of the reflection, and  $f_n$  the atomic scattering factor, which for electrons can be retrieved from the X-Rays one through the Mott-Bethe formula [8, 9]. Thus, a change in the atomic structure/positions will be reflected in a change in the intensity of the Bragg peaks. Such a change can occur because of a phase transition, strain, incoherent thermal motion, or coherent lattice vibrations. A phase transition will change the distribution and intensity of the Bragg peaks, while strain will change the lattice parameters and the Bragg peaks will be shifted. The incoherent thermal motion will change the positions of the atoms around their equilibrium positions and the Bragg peaks will be attenuated. This attenuation depends on the temperature and it is described by the Debye-Waller factor  $e^{-2W(T)}$ :

$$e^{-2W(T)} = \langle \exp(i\mathbf{q} \cdot \mathbf{u}) \rangle = \exp(-q^2 \langle u^2 \rangle / 3) \quad (1.7)$$

Where  $\mathbf{q}$  is the scattering vector,  $\mathbf{u}$  is the atomic displacement, which depends on the temperature.

Considering  $d^{[hkl]}$  the distance between the atomic planes, a deformation  $\epsilon^{[hkl]}$  along the  $[hkl]$  direction of the lattice will change such distance modifying the scattering vector  $q$ :

$$\epsilon^{[hkl]} = \frac{q_1 - q_0}{q_0} = \frac{d_1^{[hkl]} - d_0^{[hkl]}}{d_0^{[hkl]}} \quad (1.8)$$

denoting with 0 and 1 the quantities before and after the deformation. Measuring the shift  $q_1 - q_0$  will allow us to retrieve the amount of deformation.

Depending on the physical characteristics of the sample (such as quality and size) the diffraction peaks can appear differently. If the probed specimen is not a single crystal but rather a polycrystal or is amorphous, the Bragg condition will be satisfied for a range of angles leading to the appearance of Debye-Scherrer rings (see Figure 1.6g), allowing to distinguish between an ordered and disordered structure. The thickness of the sample can also play a role in determining the shape of the diffraction peaks. The reciprocal lattice is retrieved by performing the Fourier transform on the real space lattice. In the case of an infinite perfect crystal the reciprocal lattice is composed of

points, so the Ewald sphere will intercept only one point and only one diffraction spot will be visible. In the case of a finite sample with not too small dimensions, the reciprocal lattice points will be enlarged by the effect of finite sample dimensions on the Fourier transform, therefore if the radius of the Ewald sphere is large enough several lattice points will be intercepted and several enlarged diffraction spots will be visible. A third case consists of a thin sample, where the reciprocal lattice points will be elongated along the direction of the thin dimension. In this case, the Ewald sphere intercepts the elongated points and the diffraction peaks will be elongated along the direction of the thin dimension, ultimately giving rise to streaks. In the same category falls the case of a thick sample but where the penetration depth of the beam is sufficiently small to probe only the topmost layers of the surface. The three cases are represented in Figure 1.5a, b, and c, respectively.

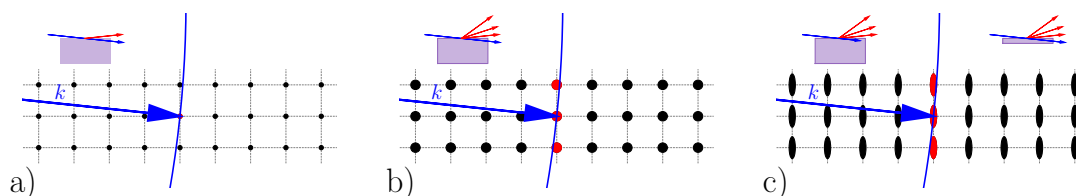


**Figure 1.5:** Intersection of the Ewald sphere with the reciprocal lattice of a) A perfect infinite crystal, b) a crystal with finite dimensions, and c) a thin crystal or a thick crystal with short penetration depth of the beam.

Furthermore, the quality of the surface (domains, roughness, islands) will affect the diffraction pattern. Some examples are shown in Figure 1.6.

### 1.3 Ultrafast Electron Diffraction

Depending on the flux of electrons and the speed of the detector, it is possible to observe changes in the structure under investigation on a timescale of the microsecond, where the limitation lies primarily on the speed of the detection electronics. This timescale is too long compared to the dynamics timescales smaller than picoseconds proper of many structural phenomena such as phase transitions and molecular dynamics. The development of pulsed laser sources with pulse duration of femtoseconds allows the exploration of out-of-equilibrium states in such phenomena [10–12] and the development of several complementary techniques including the Ultrafast Electron Diffraction (UED) [13, 14].

In UED the use of an electron probe and an optical pump, see scheme in Figure 1.7, allows to achieve a sub-picosecond time resolution and spatial resolution below  $0.01 \text{ \AA}$ . Both pump and probe originate from the same source, a fs-laser, and their delay is



### 1.3 Ultrafast Electron Diffraction

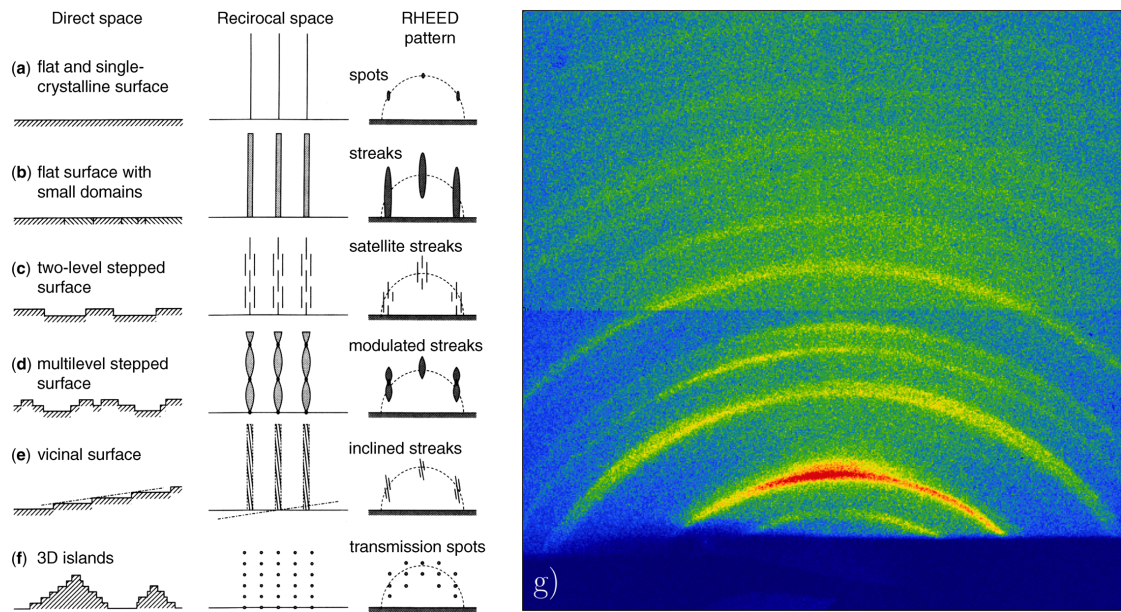


**Figure 1.6:** Examples of diffraction patterns. Panels from a) to f) are from [7], and panel g) represents Debye-Scherrer rings from adsorbed Ar on graphite (from this work).

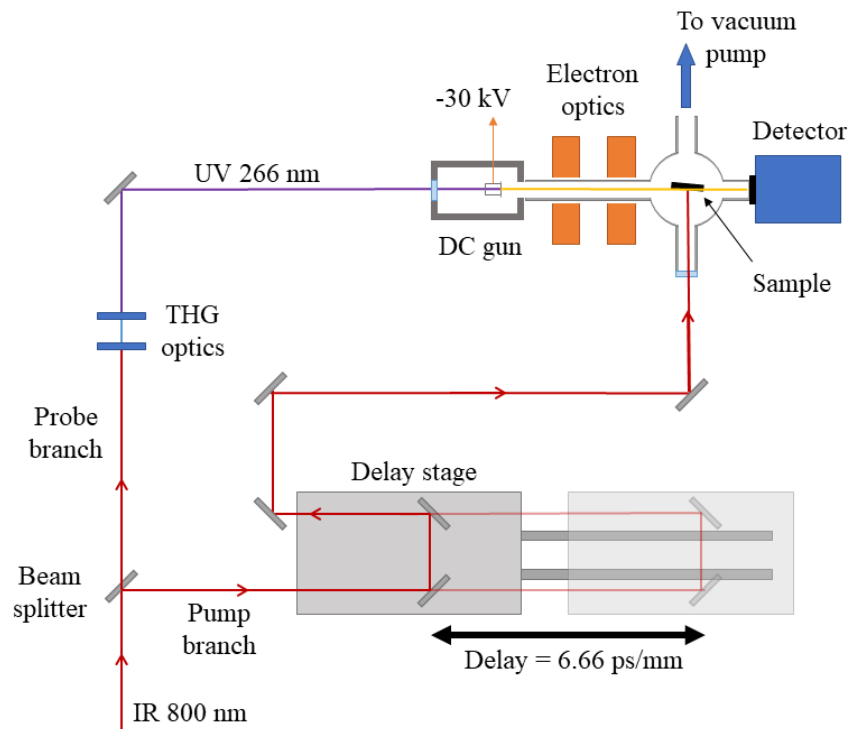


**Figure 1.7:** Scheme of a pump-probe diffraction experiment.

controlled by varying the relative length of the optical path of the two branches. In this way information such as the strain, Bragg peak position, intensity, and shape can

be acquired at different delays and the evolution of the structure can be followed on a timescale of the picosecond and below.

We present now the experimental setup, which is mostly based on the work of G. F. Mancini [15] and F. Pennacchio [16] but we describe also the important modifications and improvements necessary for the following work.

### 1.4 The UED at LUMES

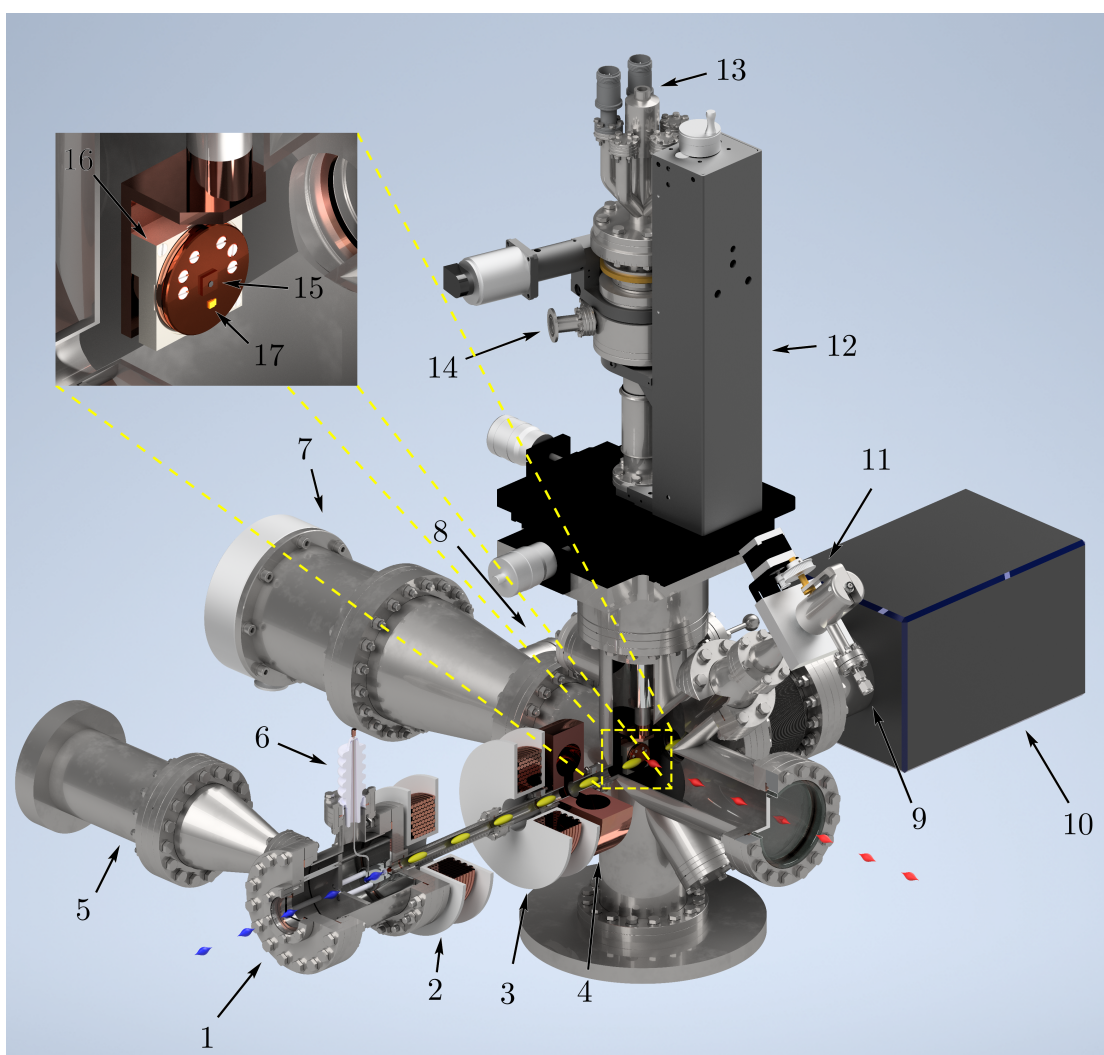


**Figure 1.8:** Schematic representation of the experimental setup. 1) DC gun; 2) collimation solenoid; 3) focusing solenoid; 4) RF cavity; 5) DC gun turbo pump; 6) HV connection; 7) main turbo pump; 8) ion gauge; 9) gas inlet; 10) detector; 11) leak valve; 12) 4-axis manipulator; 13) flow cryostat entrance; 14) cryostat vacuum port; 15) sample position; 16) 5th-axis housing; 17) sample temperature sensor.

The experimental setup is represented in Figure 1.8 and it's mostly the same built and used by Mancini and Pennacchio with some modifications. The light source is

a KMLabs Wyvern Ti:sapphire amplified laser with a 20 kHz repetition rate and 50 fs of pulse duration at 800 nm. The beam is split into two branches for the pump and probe. The pump (red pulses in the Figure 1.8) is directed through a translation stage moving a retroreflector to adjust the delay between pump and probe, then directed into the chamber to the sample. The probe beam is generated as follows: the 800 nm beam is used to generate 266 nm pulses via Third Harmonic Generation (THG) (blue pulses in Figure 1.8) utilizing nonlinear crystals. It is then focused inside the DC gun onto the back of a silver-coated sapphire window positioned on the cathode, the photocathode. The energy of the 266 nm light, 4.74 eV, is slightly higher than the work function of silver, 4.66 eV at maximum, therefore electrons are photogenerated with an energy dispersion of at maximum 80 meV. The cathode is connected to a  $-30$  kV voltage source, while the anode is a complementary plate connected to the body of the gun, therefore to ground. The emitted electrons are accelerated by the potential through a pinhole of  $150\ \mu\text{m}$  diameter and then collimated and focused via respectively two solenoids. A radio-frequency (RF) cavity allows the temporal compression of the electron bunches (yellow pulses in Figure 1.8) below 500 fs pulse duration (see [15]). The sample is mounted on a 5-axis manipulator which houses a liquid helium flow-cryostat allowing it to reach a minimum temperature of 6 K on the sample without a thermal shield. Sample and temperature sensor positions are visible in the inset in Figure 1.8. The pressure in the chamber is monitored through an ion gauge located behind the sample holder.

## 1.5 Upgrades to the setup

We describe the crucial upgrades to the setup which were functional and necessary to perform the experiments presented in this work.

### 1.5.1 Detector upgrade

The first upgrade to this setup compared to the previous version is represented by the detector: the system phosphor screen-gated MCP-CCD camera has been replaced by a DECTRIS Quadro hybrid pixel detector which allows for direct electron detection and single electron counting as well as high dynamic range, no saturation damage and high frame rate (up to several 100s of kHz) and the possibility to be triggered both via software and through an external signal. The detection principle relies on the interaction of the electrons with a thin slab of silicon, the active area, generating localized charges which are then collected by the readout electronic. As a further

consequence, the detector is not sensitive to light with energies below x-rays, which is a useful feature in a setup where light is used both to generate the electron beam (and leaves a residual beam), to photoexcite the sample, as a heat source and as well to observe the sample position and alignment and to measure the pressure via an ion gauge. All of the above light sources can be detrimental to a detection system based on a phosphor screen. The detector has an image resolution of  $514 \times 514$  pixel with up to 32-bit depth (in auto-summation mode) and a pixel size of  $75 \mu\text{m}$ , therefore total dimensions of  $38.4 \times 38.4 \text{ mm}^2$ . A comparison between two patterns of the same sample taken in similar conditions is shown in Figure 1.9. The new detector presents little to no background noise thanks to the direct detection of the electrons and a pre-existing dark noise subtraction. The ADC range of the two detectors for a single frame is the same, 16-bit, but the absence of spurious background in the Quadro system results in a higher effective dynamic range. Furthermore, the previous system showed a subpattern in the intensity of the pixels, visible in the inset in Figure 1.9a, which is not present in the Quadro system. This subpattern is due to the coupling between the optical fibers and the MCP-CCD camera and it reduced the signal-to-noise ratio and the effective resolution of the detection. The previous system had a thin layer of aluminum (200 nm) deposited over the phosphor screen to reduce the sensitivity to light but allow the electrons to pass through. This layer proved to be not sufficient to block all the light, especially in case of high pump powers, and defects on its surface limited the maximum exposure time. The Quadro detector is not affected by this problem and can be used with high pump powers and long exposure times.

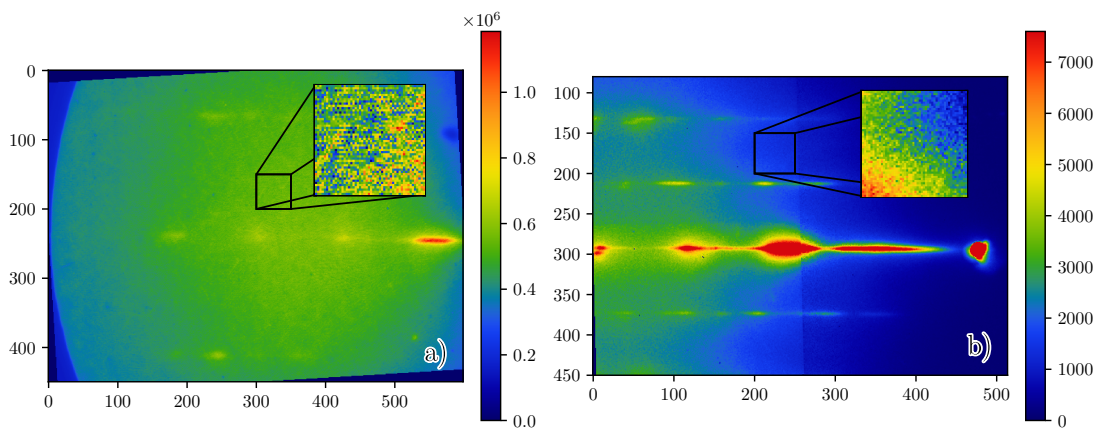


**Figure 1.9:** Graphite patterns acquired with a) previous detection system and b) Quadro detector. The insets show a magnified view of a portion of the image.

In this new configuration, the distance between the detecting surface and the sample (camera length, CL) is 425 mm; for this reason, the detector is mounted on a bellow which allows it to be moved depending on the requirements of the experiment. In this configuration, the Quadro doesn't need a beam-blocker so also the direct beam can be

monitored. Such a capability is of paramount importance in diffraction experiments for several reasons:

- it allows monitoring the beam intensity and positional stability over time;
- the distance between the diffraction features and the direct beam can be monitored to retrieve structural information;
- the relative changes between the direct beam and the diffraction pattern can be used to decouple structural effects on the sample from changes in the electron beam, including charge accumulation on the sample.

### 1.5.2 Improvements to the DC gun

When we started working with the setup we noticed two main issues with the DC electron gun: the first one was the unusual amount of time required to reach the accelerating voltage of  $-30$  kV, lasting up to several days with slow increments of the voltage, and the second was the complicated process of replacing the photocathode.

The first issue was attributed to the formation of an electric arc between the photocathode and the anode due to dirt on the two surfaces and incorrect gluing of the photocathode. We accurately cleaned the surfaces and repeated the procedure without any improvement in the situation. We then focused our attention on the connection between the cathode and the HV source and we suspected that the insulation of the connecting cable degraded over time and was not able to withstand the high voltage. We found out that this was indeed the case and we identified a point in the body of the DC gun where the arcing was taking place, visible in Figure 1.10.

We replaced the cable with a solid core copper cable and we shielded it with three concentric Teflon tubes. We also suspected that excessive wear on the potentiometer of the HV source caused sudden changes in the voltage and increased the probability of arcing. We, therefore, changed the control mode of the HV source from the internal system to an external one to rule out the effect of the damaged potentiometer.

These two actions combined allowed us to reach the accelerating voltage in a matter of less than a minute without sign of arcing or damage, reducing the startup time of the setup by a considerable amount.

The second issue that increased the downtime was related to the replacement of the photocathode. The photocathodes were sourced from a company that required a considerable amount of lead time and the order of several photocathodes at once. This led to possible degradation of the photocathodes while not in use, which com-

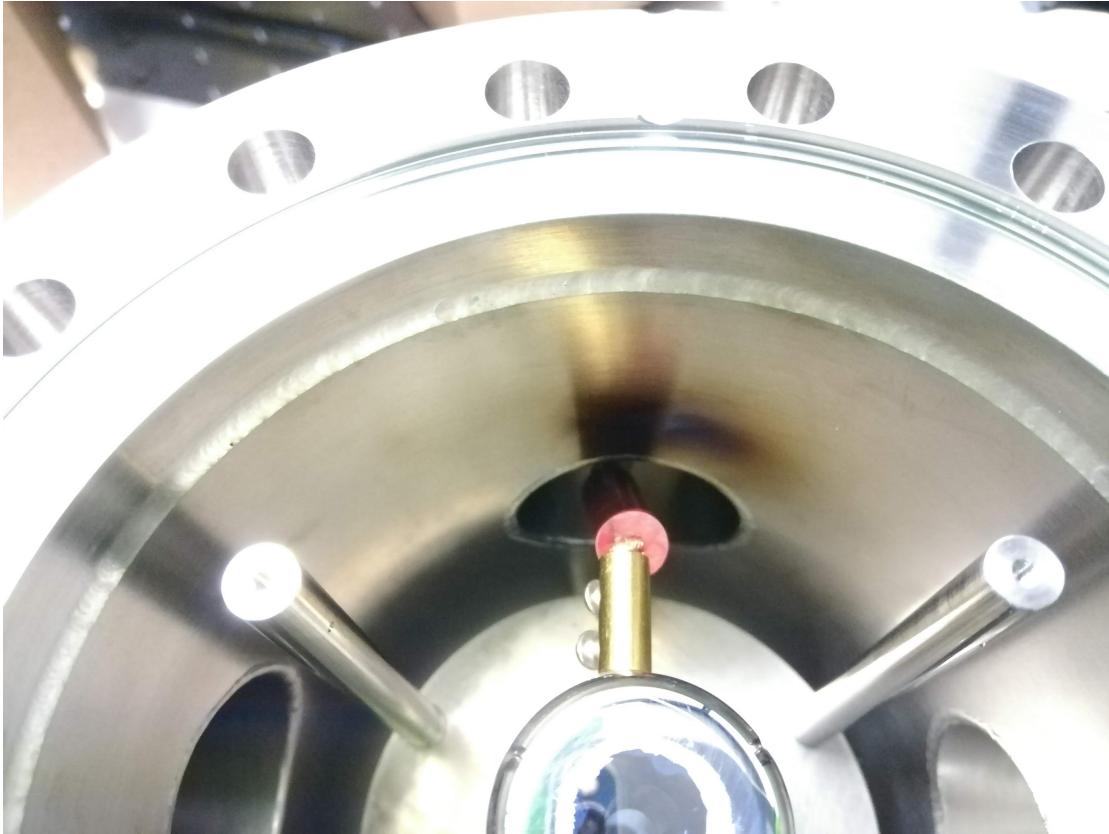


**Figure 1.10:** Inside part of the DC gun, with visible blackening on its body due to arcing.

promised the emission efficiency. Furthermore, the photocathodes were glued to the cathode using epoxy glue which required curing with heat and we noticed that the curing process damaged the silver coating. The removal of the epoxy from a previous photocathode proved to be a time-consuming process involving mechanical action on the cathode with a considerable risk of scratching the polished steel surface. We replaced the commercial photocathodes with ones made in-house using silver sputtering on a sapphire optical window and a thickness of the coating of 40 nm. We also replaced the epoxy glue with a silver paste compound which allowed us to avoid the use of heat for curing and mechanical action to remove the old photocathode. As a result, we can prepare the photocathodes when needed and we can replace them without having to dismantle the DC gun assembly and in a matter of minutes without any risk of damaging the cathode. With the commercial photocathodes the UV power used for the photoexcitation was about 6 mW while the same amount of signal was obtained with the homemade photocathodes using only 0.5 mW of UV power. We associate this increased signal with a lower work function of the in-house-made photocathodes, which, in turn, leads to a higher energy spread of the emitted electrons. Despite the higher spread, we are still able to compress the pulses up to 1 ps, which is

a sufficient resolution for the experiments described in this work, despite being worse than what was previously achieved on this setup. Concerning the durability of the cathodes, we noticed that under 6 mW UV illumination both cathodes, commercial and in-house-made, showed a degradation of the emission efficiency after about a few months of operation, while under 0.5 mW UV illumination, the in-house-made cathodes showed no appreciable degradation after more than a year of operation.

### 1.5.3 Gas injection system

Another important hardware upgrade to the setup (and vital for this work) is represented by the installation of a gas injection system, represented in Figure 1.11. The system is composed of a gas bottle, a pressure regulator that reduces the pressure to 1.5 bar, an isolation valve to separate the main chamber from the gas bottle, and a leak valve. We motorized the leak valve with a NEMA 17 stepper motor controlled by an Arduino board interfaced with the acquisition computer. This allows us to program the valve to open the gas in a repeatable way and with controlled movements with a resulting pressure control below  $1 \times 10^{-9}$  mbar. To prepare the system we close the valve on the gas bottle and open all the other valves when the main vacuum chamber is at atmospheric pressure. When we start evacuating the main chamber the gas injection system gets evacuated and once the chamber reaches the minimum pressure we close the leak valve and the isolation valve. We then open the bottle valve to fill the tube with gas regulated at 1.5 bar, in this way if there are leaks in the tube connections the positive pressure will ensure that no contamination will occur on the argon.

### 1.5.4 Cryostat and temperature sensors

The experiments presented in this work require a reliable reading of the temperature of the sample. The previous temperature sensor was not suitable for the temperature ranges we aimed to explore, therefore we replaced it with two Cernox<sup>®</sup> sensors capable of measuring temperatures as low as 1.5 K. We installed them one on the cold finger and the other on the sample holder as close as possible to the sample, and we ensured a good thermal contact between all the surfaces interfacing them with thin indium foils.

### 1.5.5 Heating control

To accurately control the temperature and achieve temperature ramps we installed a green (532 nm) 8 W ns diode laser as a heat source. We install a target made of

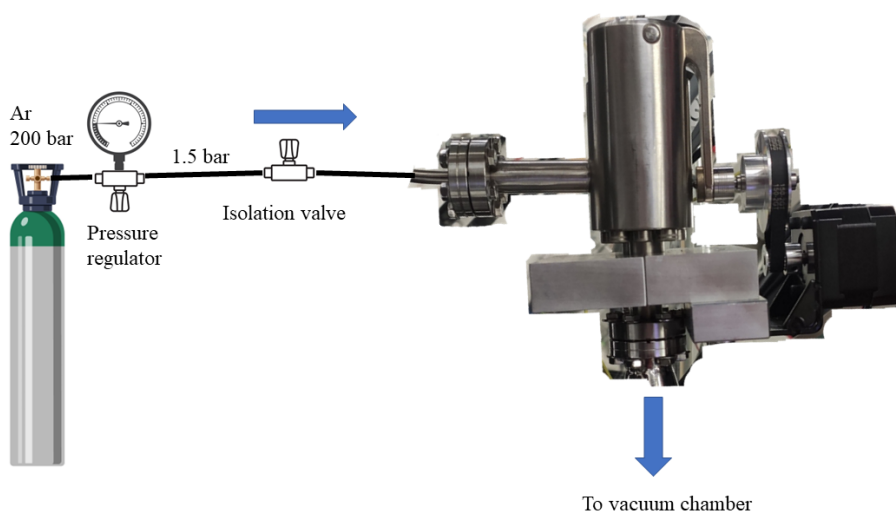


**Figure 1.11:** Gas injection system.

low-quality graphite next to the sample object of the measurement. This target will be illuminated by the green laser and transfers the heat to the sample holder. The laser is controllable with a serial communication protocol and it is interfaced with the acquisition computer.

### 1.5.6 I/O interfaces

The nature of the experiments in this work required the control and acquisition of several parameters together with the diffraction patterns. It was therefore necessary to interface the acquisition computer with the different instruments via several hardware interfaces and protocols. We used an Arduino UNO board to interface the leak valve while an Arduino DUE is connected to the analog output of the pressure gauge. This board represents the best choice since the resolution of its ADC (12-bit) matches the resolution of the DAC at the output of the pressure gauge. The temperature controller is interfaced via serial communication through a USB connection.

### 1.5.7 Software

Part of this work consisted of the development and implementation of a software interface capable of collecting all the vital information about the experiment parameters and controlling them in a reproducible and reliable way. We developed a second



## **1.5 Upgrades to the setup**

---

software capable of analyzing the data in volumes and in a repeatable way providing immediate feedback to the user. A version of the software to be publicly released is under preparation. More details about the software can be found in Appendix A.



## 2 Growth and investigation of Argon thin films adsorbed on graphite by means of Ultrafast Electron Diffraction

### 2.1 Introduction

For longer than 100 years the scientific community has been fascinated by phase transitions. In 3D systems, two types of transition are known: a discontinuous one where the order parameter changes abruptly, the so-called first-order, and a continuous one where the order parameter changes gradually and two phases coexist at a critical temperature  $T_c$ , the so-called second-order. By changing the dimensionality to 1D Peierls showed that long-range positional order can exist only at  $T = 0$  K[17].

In 2D systems, Mermin suggested the presence of an intermediate state where the long-range order is replaced by a quasi-long-range positional order[18]. The transition between these two orders is called continuous melting.

These works attest that the dimensionality of the system plays a crucial role in the mechanism of the phase transition and raise the importance of understanding such a process, particularly in 2D materials. In this regard, Kosterlitz and Thouless proposed a theory (KT theory) to describe the phase transitions in 2D systems such as superfluids, superconductivity, and XY models[19, 20]. KT theory is based on the idea of the

formation and dissociation of dislocation pairs. A dislocation can be seen as an extra row of atoms in the lattice and, if a closed path around it is taken the path will fail to close by an amount given by the Burgers vector  $b$ , see Figure 2.1a. Bound dislocation pairs can be created as the temperature rises and their unbinding leads to a continuous transition from a low-temperature quasi-long range ordered phase to the high-temperature disordered phase.

In the continuity of the work of KT, Halperin, Nelson, and Young (HNY) [21, 22] noticed the presence of an intermediate phase, called hexatic phase, represented in Figure 2.1b.

The degree of order of the structure can be estimated evaluating the decay of the density-density correlation function for the positional order and the bond-angular correlation function for the orientational order. The former is defined as:

$$g_{\vec{G}}(|\vec{r} - \vec{r}'|) = \left\langle e^{i\vec{G}[\vec{u}(\vec{r}) - \vec{u}(\vec{r}')]}\right\rangle \quad (2.1)$$

where  $\vec{G}$  is the reciprocal lattice vector,  $\vec{u}(\vec{r})$  is the thermal atomic displacement and  $\langle \dots \rangle$  is the statistical average over all atomic positions.

In case of a solid, the density-density correlation function is long ranged, therefore  $g_{\vec{G}}(r) \propto r^{-\eta}$ , an algebraic decay, while in a liquid such positional order is short ranged, therefore  $g_{\vec{G}}(r) \propto e^{-r/\eta}$ , where  $\eta$  is the correlation length.

The bond-angular correlation function is defined as:

$$g_6(|\vec{r} - \vec{r}'|) = \left\langle e^{i6[\theta(\vec{r}) - \theta(\vec{r}')]}\right\rangle \quad (2.2)$$

where  $\theta(\vec{r})$  is the angle between the bond between a particle at position  $\vec{r}$  and its nearest neighbors relative to an arbitrary axis.

In a solid, for long distances the bond-angular correlation function is constant, therefore  $g_6(r) \propto \text{const}$ , while in a liquid such orientational order is short ranged, therefore  $g_6(r) \propto e^{-r/\eta_6}$ , an exponential decay, where  $\eta_6$  is the correlation length of the orientational order.

The peculiarity of the hexatic phase is being an intermediate configuration between the solid and liquid phases, where the density-density correlation function is short ranged, therefore  $g_{\vec{G}}(r) \propto e^{-r/\eta}$ , while the bond-angular correlation function is long ranged and depends on the temperature, therefore  $g_6(r) \propto r^{-\eta_6(T)}$ .

Thanks to the sensitivity to the structural arrangement, diffraction patterns hold valuable information about the order of the system. In a solid, which is defined by

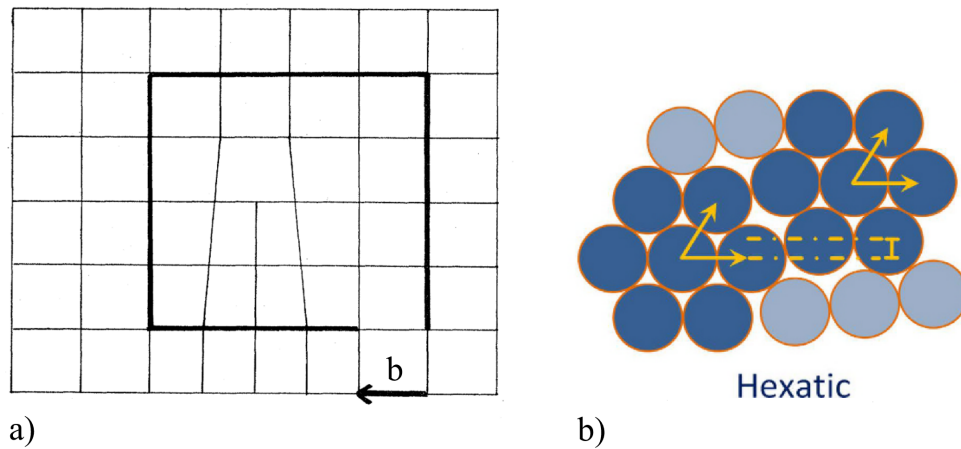


**Figure 2.1:** a) Simple dislocation, adapted from [23]. The Burgers vector is represented by the  $b$  vector. Scheme of the hexatic phase, adapted from [24].

a long-range positional order, the diffraction pattern is generally characterized by Bragg peaks, which are reflecting the periodicity of the lattice, (Figure 2.2a). In the liquid phase, the long-range positional order is absent leading to a diffraction pattern without Bragg peaks, instead the presence of a ring (Figure 2.2c). The latter is due only to the average of the random distances between the atoms.

In the hexatic phase, the presence of short-range positional and quasi-long-range bond-orientational orders causes an isotropic ring in the diffraction pattern from an infinite sample, while in a finite sample, the intensity of the ring exhibits a maximum every 60 degrees, following the six-fold symmetry of the hexatic phase, for example in Refs. [24–26] (Figure 2.2b).

In this chapter we aim to investigate the phase transitions in 2D systems, therefore, we choose rare gases adsorbed on graphite as a prototype for a pure 2D system. These systems present the advantage of having a simple unit cell, containing only one atom, on a well-known substrate, and the weak interaction between substrate and adsorbate results in a weak coupling of the two. In this work, we start our investigation with Argon (Ar) adsorbed on graphite. This choice is justified by the thermodynamic constraints accessible by our experimental setup, which are low temperature, in the range of 10-40 K, and low pressure, in the range of  $1 \times 10^{-9}$ -  $1 \times 10^{-6}$  mbar. We use Reflection High Energy Electron Diffraction (RHEED) technique to investigate the structural transformation accompanied by the thermodynamic transition of Argon films adsorbed on graphite. Thanks to the structural information we can retrieve a deposition kinetics diagram of the Argon films to reveal the presence of a mixed

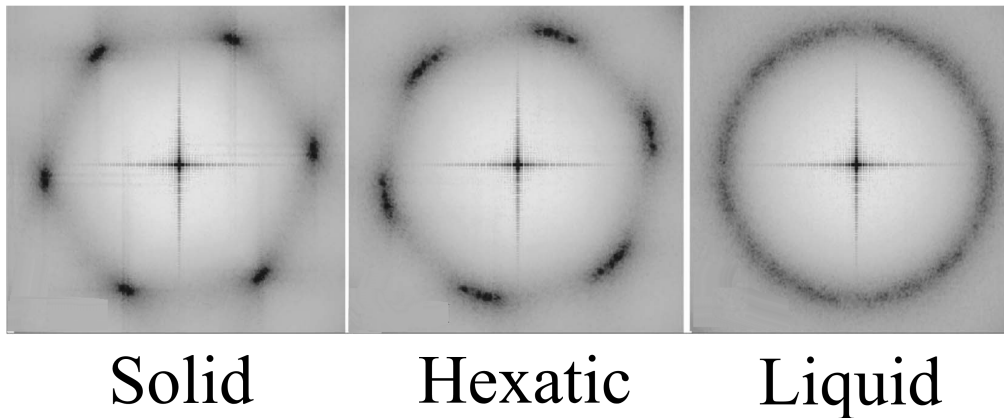


Figure 2.2: Diffraction patterns from: a) solid, b) hexatic and c) liquid phases. Adapted from [26]

crystalline configuration.

## 2.2 Previous works on Argon films adsorbed on graphite

As a noble gas, Argon does not form a strong ionic or covalent bond with the other atoms. Instead, its interaction consists of weak omnidirectional Van der Waals forces which can be described by the Lennard-Jones (LJ) potential, Figure 2.3a, where  $\sigma$

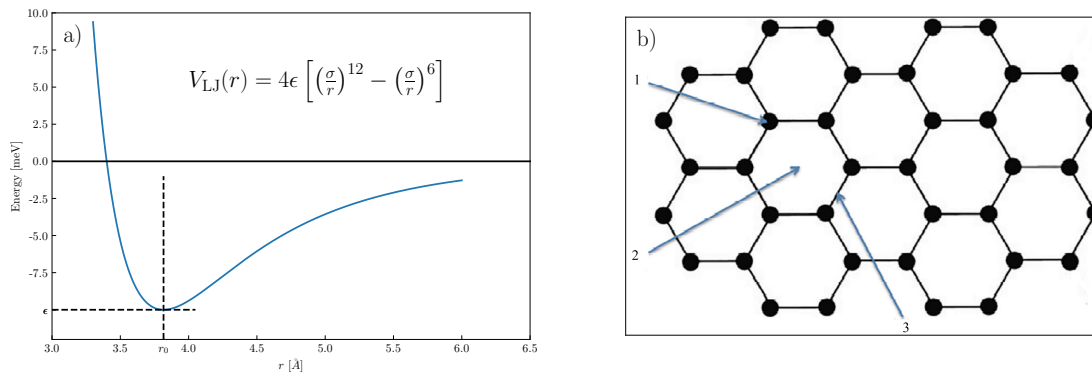


Figure 2.3: a) Lennard-Jones potential for Ar-Ar. b) Preferential adsorption sites for Ar on graphite, adapted from [27].

represents the particle-particle distance at which the potential is zero and  $\epsilon$  is the depth of the potential well. This potential is composed of two terms: the first term is a short range repulsive term originating from the Pauli repulsion of the atomic orbitals, which is a twelfth power of the distance between the particles, and the second term is an attractive term from Van der Waals forces, which is a sixth power of the distance

## 2.2 Previous works on Argon films adsorbed on graphite

between the particles and acts at long distances. The equilibrium distance between two particles is given by the position of the minimum of the potential, which is at  $r_0 = \sqrt[6]{2}\sigma$ . In case of Argon-Argon interaction, such parameters are:  $\sigma = 3.4 \text{ \AA}$  and  $\epsilon = 0.0103 \text{ eV}$ , with  $r_0 = 3.82 \text{ \AA}$  [28].

The interaction of Argon with graphite has different LJ parameters and they have been investigated teoretically by Ambrosetti *et al.* [29] and by Maiga *et al.* [27] similarly on graphene using a corrected Lennard-Jones potential. In both works, Argon shows three possible sites for adsorption on graphite, Figure 2.3b:1) the top of the carbon atom, 2) the hollow hexagon, 3) the top of the bond, with the hollow site being the most attractive. Ambrosetti found an adsorption energy of  $-0.107 \text{ eV}$ , which is 10 times higher than the energy between Ar atoms. The shape of the LJ potential is asymmetric, steep at the repulsive part and smoother in the attractive part. Therefore compressions below  $r_0$  require more energy than an equivalent expansion. The equilibrium distance  $r_0$  for Ar-Ar interaction respect to the graphite surface structure imposes that the Argon atoms are adsorbed preferentially on hollow sites forming a lattice close to the  $(\sqrt{3} \times \sqrt{3})R30$  mesh of graphite, which has a lattice constant of  $4.26 \text{ \AA}$ , see Figure 2.4. An adsorbed layer with the same lattice constant as the  $(\sqrt{3} \times \sqrt{3})R30$  mesh would result in a commensurate structure, but since the  $r_0$  distance is slightly smaller than the mesh lattice constant, the structure is expected to be incommensurate. The

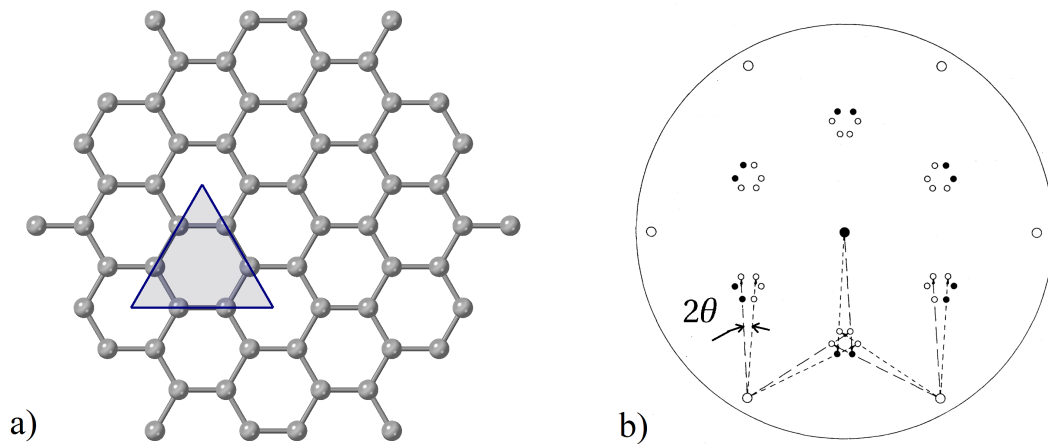


**Figure 2.4:** a) Representation of the  $(\sqrt{3} \times \sqrt{3})R30$  mesh on graphite. b) LEED pattern of adsorbed Ar on graphite, from [30]

incommensurate phase is confirmed by experiments in Low Energy Electron Diffraction by Shaw *et al.* [30, 31]; the authors found that the Argon atoms are adsorbed with the nearest-neighbor (NN) distance between  $3.82 \text{ \AA}$  and  $3.94 \text{ \AA}$ , depending on the density, at  $42 \text{ K}$ . The authors also claim the presence of a rotation of the adsorbed

## Chapter 2. Argon thin films

layer with respect to the substrate, see Figure 2.4b, previously predicted by Novaco and McTague [32]. The latter predicted that, due to the incommensurate structure, the adsorbed layer would rotate as much as 4 degrees around the normal vector to the plane. Adsorption isotherms experiments by Jura *et al.* [33] showed unusual discontinuities at around 65 K, Figure 2.5a, attributed to the heterogeneity of the substrate. Further experiments by Crowell *et al.* [34] found no evidence of a first-order phase transition above 67 K, Figure 2.5b.

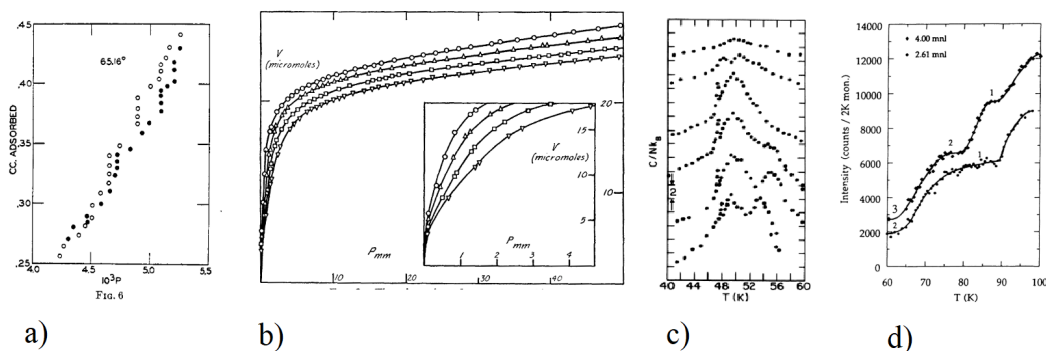


**Figure 2.5:** a) adsorption isotherms from [33]; b) adsorption isotherms from [34]; c) heat capacity from [35]; d) Bragg peak intensity from [36].

Shaw *et al.* found as well a change in the slope of the adsorption isotherms at 50 K, which they attributed to the transition from a 2D fluid to a 2D incommensurate solid phase. Neutron diffraction experiments by Taub *et al.* [37] found the same incommensurate structure but no evidence of a first-order transition. Such evidence was brought forward by Migone *et al.* with heat capacity measurements [35] finding a peak at 47.2 K associated with a weak first-order transition, and a broader peak at 49.5 K associated with a KTHNY melting, Figure 2.5c. Another neutron diffraction study of the melting has been conducted by Laese *et al.* [36] and showed instead that the melting of a multi-layer system happens layer by layer every single layer melts continuously, Figure 2.5d. Another work by McTague and Nielsen [38] with x-ray diffraction found evidence of the continuous melting and has been interpreted as a hexatic phase. The authors constructed a phase diagram for temperatures above 40 K, visible in Figure 2.6. At temperatures below 40 K, the authors report a gas (G) plus incommensurate solid (IS) phase but such a range of temperatures was not explored by their experiment. All these previous works show that the physics of the Ar films adsorbed on graphite is complex and highly disputed. The purpose of this work is to bring new insights into the mechanism of the deposition and the melting processes of Ar films adsorbed on graphite. We rely on structural transformations to identify the different orders possible in the system. The novelty of this work is the investigated area of the phase diagram pressure vs. temperature in a range never explored before



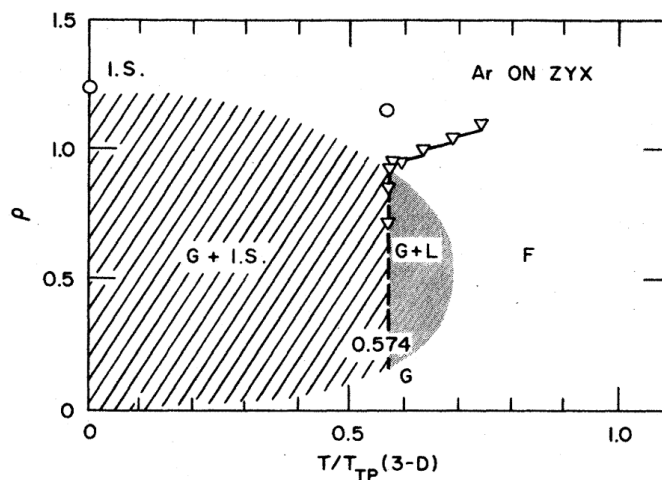


**Figure 2.6:** Phase diagram of Argon adsorbed on graphite by McTague and Nielsen [38] as density of the layer versus temperature expressed as a ratio to the triple point  $T_P = 84\text{K}$ .

(below 40 K and below  $1 \times 10^{-6}$  mbar).

## 2.3 Experimental procedure

In the following section, we will discuss the experimental procedures used to achieve the results presented in this work, including the substrate characterization, the calibration of the diffraction patterns, the deposition and melting of Argon films protocols.

### 2.3.1 Characterization of the substrate

The chosen substrate consists of natural graphite flakes acquired from Naturally Graphite and sent by Prof. John Jaszczak from Michigan Technological University. The sample provider sorted the samples into three categories after characterizing them with Laue diffraction: excellent, high, and normal quality. The flakes have a size of 1-2 mm and are provided in batches of 10-20 flakes from different countries of the world, see inset in Figure 2.7a. We chose graphite because the symmetry of its surface matches the six-fold symmetry of the close-packed structure of solid Ar. We prefer natural graphite to synthetic ones (e. g. Highly Oriented Pyrolytic Graphite, HOPG) because the latter exhibits a considerable surface roughness and it is difficult to obtain a clean flat surface. The surface flatness is important for two reasons: firstly, RHEED is a surface-sensitive technique and a high roughness can lead to a total loss of diffraction peaks at low orders. Secondly, the high roughness can hinder the uniform adsorption of the Argon and prohibit a layer-by-layer deposition (see subsection 2.4.1).

## Chapter 2. Argon thin films

---

The substrate is glued to the sample holder with an electrically conductive compound (Silver paint) and freshly cleaved at room temperature with adhesive tape just before closing the vacuum chamber. We investigate the condition of the graphite surface at room temperature; this operation is necessary firstly because the exfoliating procedure can leave a damaged surface or semi-detached graphite layers that can block the beam and compromise the surface quality, and secondly, because the graphite pattern is used to calibrate the diffraction pattern, see subsection 2.3.2. This information can be retrieved by acquiring the diffraction pattern as a function of the incidence angle  $\theta$ , a so-called rocking curve. To represent it we sum all the patterns acquired resulting in a single frame with all peaks visible. Figure 2.7a shows the rocking curve of natural graphite at 300 K. The field of view of the detector is sufficiently wide to capture up to the [008] peak in the out-of-plane (OOP) direction [001]. The in-plane (IP) direction shows the  $[0\bar{1}l]$  and  $[01l]$  peak families. The indexing of the pattern can be retrieved by measuring the ratio of the distances between the peaks, while the zone axis can be calculated by the cross product between the IP and OOP vectors [39]. For the pattern in Figure 2.7a the zone axis is [210], inset in Figure 2.7b.

The optimal alignment of the sample requires that the intensities of the  $[0\bar{1}l]$  and  $[01l]$  peak families are equivalent. Figure 2.7b shows the rocking curve of graphite at 19 K. At low temperatures, the pattern appears sharper, due to a smaller Debye-Waller factor. In addition, the pattern reveals the presence of multiple domains with similar orientations. Since the sample is of natural origin and mm-sized, the presence of domains is not surprising and their good alignment is a sign of a good quality sample. No transmission spots are present, which means that the exfoliation procedure didn't leave any partially bent and lifted layer of graphite (at least in the area probed) and the surface is flat.

We notice that the Bragg peaks are elongated along the OOP direction due to the short penetration depth of the electrons on graphite in grazing incidence. The estimation of the peak center position with respect to the direct beam is affected by an error that becomes greater the lower the diffraction orders.

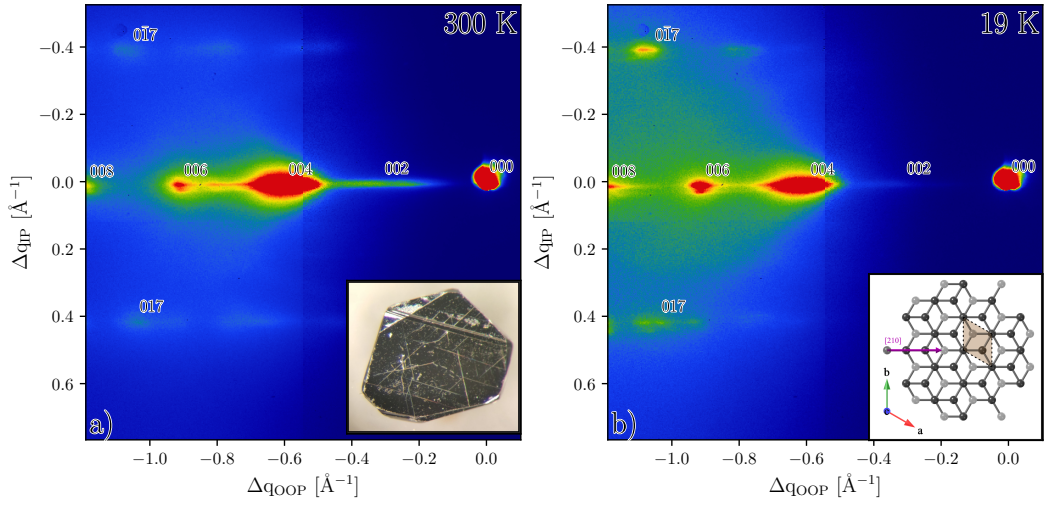


**Figure 2.7:** Diffraction pattern of graphite at a): 300 K, b) 19 K, obtained as a superposition of all the patterns acquired during the rocking curve. The peaks are indexed with respect to the zone axis [210]. The inset in a) shows the sample surface under the microscope before the exfoliation, inset in b) shows a top view of the graphite structure with the crystallographic directions and in purple the zone axis used for the diffraction patterns.

### 2.3.2 Calibration of the diffraction patterns

To retrieve the lattice parameters of an unknown sample it is necessary to calibrate the diffraction pattern from pixels to  $\text{\AA}^{-1}$ . This can be done either by geometrical considerations on the setup or by using a well-known sample as a reference, in our case it is the substrate, graphite.

#### Geometrical approach

A scheme of the geometry of the experiment is represented in Figure 2.8.

The distance between the detector and the sample (called camera length CL) must be known, together with the physical size of each pixel  $\delta$  of the detector and the wavelength  $\lambda$  of the electrons. It is important to remember that the angles measured on the detector with respect to the direct beam are  $2\theta$ , where  $\theta$  is the angle of the scattered radiation from the Bragg law. The distance  $x$  between one diffraction spot and the direct beam can be expressed as:  $x = CL \tan(2\theta)$ , while, from the Bragg law:  $\theta = \arcsin\left(\frac{\lambda}{2d}\right)$  where  $d$  is the interplanar spacing of the diffraction peak, which in this case can be kept as 1  $\text{\AA}$ . In our case:  $CL = 42.5 \text{ cm}$ ,  $\lambda = 0.0698 \text{ \AA}$ ,  $\delta = 75 \mu\text{m}$ . Therefore:

$$x = CL \tan\left(\arcsin\left(\frac{\lambda}{2d}\right)\right) = 2.972 \text{ cm} \quad (2.3)$$

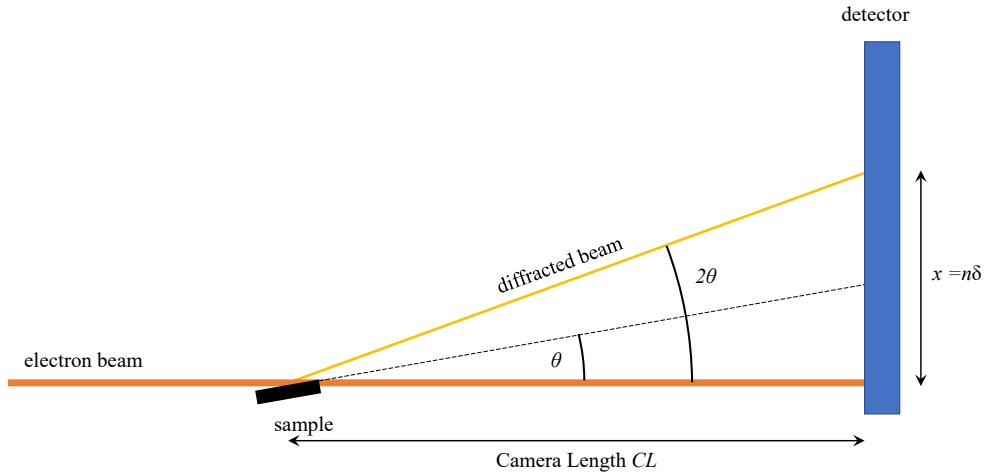


**Figure 2.8:** Schematic of the geometry used to calibrate the diffraction pattern. The distance between the sample and the detector is  $CL$ , the physical size of each pixel is  $\delta$  and the distance of the diffracted beam from the direct one on the detector is  $x = n\delta$  where  $n$  is the number of pixels.

This physical distance of  $1 \text{ \AA}$  corresponds to  $\frac{x}{\delta} = 397$  pixel. Since the diffraction pattern is an image of the reciprocal lattice, the calibration constant will be  $k = \frac{1}{397 \text{ pixels \AA}} = 0.00251 \text{ \AA}^{-1} \text{ pixel}^{-1}$ .

### Calibration with graphite

For this method the lattice parameters of graphite must be known, in this case, we use the parameters from Trucano *et al.* [40]  $a = b = 2.464 \text{ \AA}$  and  $c = 6.711 \text{ \AA}$ . The distance  $x$  in pixel between the direct beam and a known diffraction peak is measured: for the pattern in Figure 2.7a and b, the best choice is the [008] peak. The distance between the direct beam and the [008] peak is 466 pixel, while its interplanar spacing  $d$  is  $0.8389 \text{ \AA}$  and the reciprocal  $d^*$  is  $1.1921 \text{ \AA}^{-1}$ . The calibration constant is therefore  $k = \frac{d^*}{x} = 0.00256 \text{ \AA}^{-1} \text{ pixel}^{-1}$ . Another possibility is to use the distance between peaks in the IP direction, which is not affected by the OOP elongation due to the low penetration depth. In our case the distance  $D = 320$  pixel between the  $[0\bar{1}7]$  and  $[017]$  peaks can be used, which corresponds to  $0.812 \text{ \AA}^{-1}$ , therefore  $k = 0.00254 \text{ \AA}^{-1} \text{ pixel}^{-1}$ .

These values are in agreement with the geometrical approach within a few %. This method can also be used to estimate the camera length.

It is important to note that in principle the images also need to be corrected for spherical aberration since the detector is flat and we want to measure angles. The difference in the peak position for an angle  $\theta = 5^\circ$  can be estimated as:  $CL(\tan\theta - \theta) =$

94  $\mu\text{m}$ , which is comparable to the size of one pixel. Therefore, the correction is negligible if compared to the distances used to calibrate, and the calibration constant is not affected by it in a meaningful way.

### 2.3.3 Deposition of Argon

To prepare for Argon deposition the graphite is cooled with a maximum ramp of approximately 4 K/min to prevent sudden thermal contraction that can lead to damage to the substrate. In addition, while cooling down, a CW laser can be pointed on the sample to reduce the probability of condensation of impurities and residual gases ( $\text{CO}_2$ ,  $\text{H}_2\text{O}$ ,  $\text{N}_2$ ,  $\text{O}_2$ ). During the cooling ramp, the surface of the substrate is monitored paying attention to the movement of the sample holder due to the thermal contraction of the cryostat. The deposition is carried out at a constant temperature and the gas is injected with the leak valve increasing pressure with a logarithmic constant rate. We set a maximum pressure value to not exceed  $1 \times 10^{-6}$  mbar to ensure that the propagation of the electron beam is not affected by the reduction of the mean free path and to prevent damage to the turbopumps. To construct the deposition kinetics diagram we used the same protocol at different temperatures from 10 K to 40 K.

### 2.3.4 Melting of the Argon films

We carry out the melting of the Argon films by heating the sample with a constant ramp. In the meanwhile, we continuously acquire the diffraction patterns. The intensity of the diffraction pattern sets an upper limit in determining the speed of the ramp since for each acquired pattern the temperature must not vary excessively between the beginning and the end of the acquisition. A lower limit is set by the long-term stability of the system which is subjected to drifts of the laser and electron beam. We set the maximum ramp to 0.5 K/min. Unfortunately, during the melting our setup does not allow us to correlate the measured pressure with the acquired pattern and the measured temperature: the deposition procedure allows us to observe the growth of the Argon films on the graphite substrate but the condensation of the gas occurs over the entire sample holder and the cold finger, which are exposed to the gas and at temperatures between the one recorded on the sample and the lower one at the cold finger, and have a surface area orders of magnitude larger than the graphite sample.

### 2.4 Results and discussion

In this section, we will discuss the process of deposition of Argon, determine the structure and its lattice parameters, and construct its deposition kinetics diagram pressure vs. temperature. Finally, will discuss the thermodynamic melting of the Argon films within the KTHNY theory.

#### 2.4.1 Deposition process

Figure 2.9 demonstrates the deposition process of Argon on graphite at 25 K. Without gas injection, we see the graphite pattern Figure 2.9a, characterized by a streak relative to the [002] peak which indicates a high quality surface of graphite. While increasing gradually the pressure the intensity of the graphite peak decreases. When it reaches the minimum value at  $1.4 \times 10^{-8}$  mbar we start seeing a streak which we attribute to the formation of a monolayer of Argon, Figure 2.9b. Increasing the pressure to  $2.9 \times 10^{-8}$  mbar mixed diffraction features of streaks combined with Bragg peaks appear, Figure 2.9c. At around  $8.9 \times 10^{-8}$  mbar the Bragg peaks disappear and only the streaks remain. At high pressure, above  $6 \times 10^{-7}$  mbar, the pattern shows mainly sharp Bragg peaks. To determine the growth mode of the adsorbate we followed the evolution of the intensity of the peaks with increasing pressure, Figure 2.9k. The curve indicates that the growth is not layer-by-layer but rather is very similar to an epitaxial growth following the Stranski-Krastanov model [41]. In our case the growth shows intermediate steps and the whole process is sketched in panels (f) to (j): starting from the graphite surface with some defects (f) a monolayer is formed (g) and diffraction streaks are visible; the defects favor the nucleation of crystalline Ar (h) generating the weak transmission spots visible in (c), then the gaps between defects are filled creating a flat multi-layer film (i) where the diffraction pattern loses the peaks and shows mainly streaks, and finally, the growth of islands continues (j) producing again transmission spots. We take note of the pressure at which this first layer is half-filled, which we call  $p_0$ . Such pressure can be used as a qualitative reference to estimate the transition point from the gas phase to adsorbed phases (solid, liquid, hexatic).

#### 2.4.2 Determination of the structure of the adsorbate

Thanks to the diffraction pattern we retrieve the crystal structure of the adsorbed Ar and its relative orientation with respect to the graphite substrate.

Figure 2.10a shows the rocking curve of adsorbed Ar deposited at 19 K with a maximum pressure of  $5 \times 10^{-7}$  mbar. without changing the azimuthal angle  $\phi$  while Figure 2.10b

shows the rocking curve of the same deposition with  $\phi = 30^\circ$ . Both patterns are consistent with a Face Centered Cubic (FCC) structure with the [111] direction parallel to the out-of-plane axis of graphite and the  $[\bar{4}22]$  axis parallel to the  $b$  axis of graphite, as shown in panel (c). The patterns are indexed consequently.

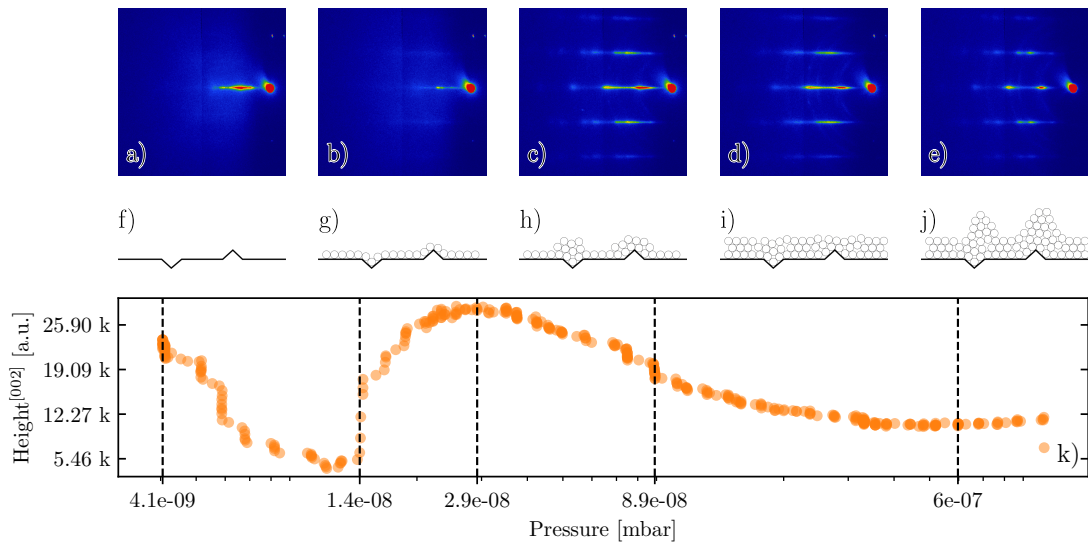


**Figure 2.9:** Patterns and peak intensity during Ar deposition at 25K. Panels a-e show the pattern evolution from graphite to Ar peaks; panels f-j show a schematic representation of the growth stages. Panel k shows the evolution of the intensity of the peaks with increasing pressure. The dashed lines mark the values of pressures corresponding to the patterns shown in (a-e) and growth stage sketches (f-j).

The Argon atoms form layers on the graphite sitting preferentially on the center of the honeycomb hexagons in a  $(\sqrt{3} \times \sqrt{3})R30$  mesh, which means a triangular lattice with nearest-neighbor separation of  $\sqrt{3} \times a$ , where  $a = 2.46 \text{ \AA}$  is the lattice constant of graphite, and rotated 30 degrees respect to the graphite unit cell.

On graphite, there are 3 possible kinds of hexagon sites, A, B, C, and each layer sits on the same kind of site, leading to stacking of the form ABC, see Figure 2.10c left side. The growth of the first layer can start from any of the three sites from different areas of the substrate but maintains the three stacked layers thus originating a two-fold twinning configuration. Such twinning is revealed on the pattern by the double peaks, i.e. 311 and 022 in Figure 2.10a, which are labeled with different colors.

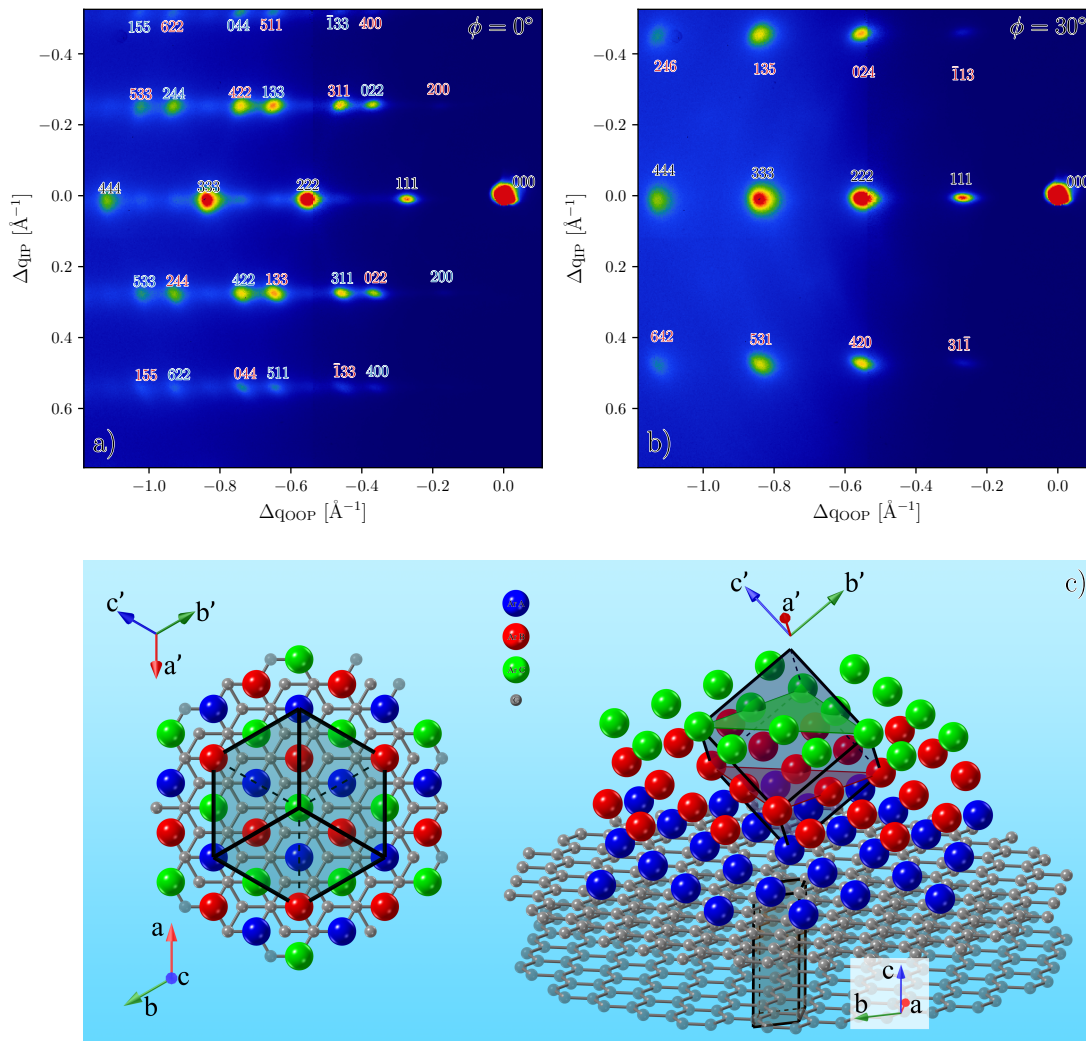


**Figure 2.10:** a) Rocking curve of adsorbed Ar with azimuthal angle  $\phi = 0$  and b) rocking curve of the same adsorbed structure with  $\phi = 30^\circ$ , both obtained at 19 K. The two twins are labeled with red and blue labels, while the black labeled peaks are common between the two. c) Top and perspective views of 3 layers of adsorbed Ar on the graphite substrate with FCC unit cell and axes orientation.

If the stacking would have involved only two layers the double peaks would have been replaced by a single peak from a Hexagonal Close Packed (HCP) structure which has a stacking of the form ABAB.

The interlayer distance and the NN distance can be estimated from the OOP and IP directions respectively. For the former, considering the  $d^*$  for the [444] peak as the distance from the direct beam on the calibrated pattern, the interplanar spacing will be  $4/d^* = 3.58\text{\AA}$ . For the IP direction, instead of using the single peaks it is more useful to take advantage of the entire horizontal rows and estimate the distance between



parallel rows. Considering that the distance between the row from [200] to [533] and the row from [400] to [155] is equal to the  $[\bar{4}22]$  vector, the NN distance  $d_{\text{NN}}$  can be calculated using the formula:

$$d_{\text{NN}} = \sqrt{\frac{-4^2 + 2^2 + 2^2}{d^{*2}}} \frac{1}{\sqrt{2}} \quad (2.4)$$

The factor  $\frac{1}{\sqrt{2}}$  after geometrical considerations: on the FCC cell the [111] plane cuts the faces of the cube along the diagonal, therefore the distance between nearest neighbors will be  $a' \frac{\sqrt{2}}{2} = \frac{a'}{\sqrt{2}}$ , where  $a'$  is the lattice constant of the FCC cell. During this work, we used several natural graphite samples with different quality, and depositions performed with the same procedure led to NN values between 3.92 Å and 3.97 Å. Since the  $(\sqrt{3} \times \sqrt{3})\text{R}30$  mesh has a NN distance of 4.26 Å, the value of  $d_{\text{NN}}$  is compatible with an incommensurate phase, which has been observed in previous experiments [30, 37, 38]. However, one sample batch showed a NN distance of 4.26 Å, which is the expected value for a commensurate phase. Depositions on these samples were performed at different temperatures and consistently resulted in a commensurate phase never observed before and represented in Figure 2.11 with a comparison between the two in-plane distances. It is clearly visible that  $D_c > D_i$ . We suspect that the change from incommensurate to commensurate is related to the quality of the samples. The commensurate phase was observed only on samples with excellent-quality while high and normal-quality samples always resulted in incommensurate phases.

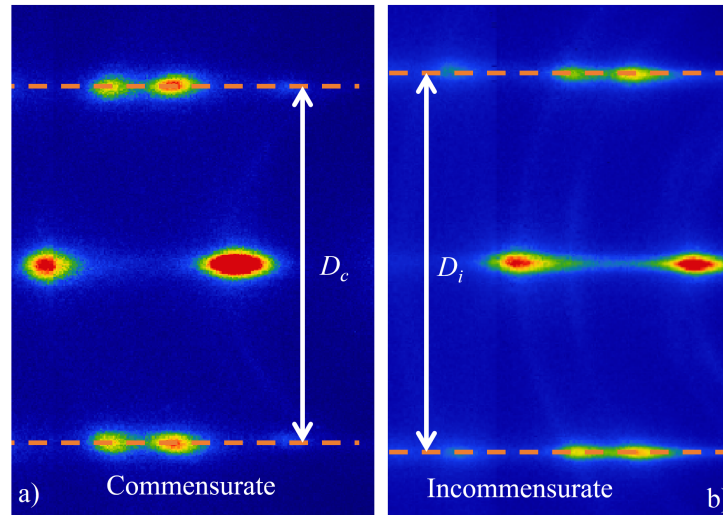


**Figure 2.11:** a) Diffraction pattern of solid Argon at 19K on a sample with a commensurate phase. b) Diffraction pattern of solid Argon at 19K with an incommensurate phase.  $D_c$  and  $D_i$  represent the distance in-plane between the peak rows of the commensurate and incommensurate phases respectively.  $D_c > D_i$ .

### 2.5 The possibility of the hexatic phase

The depositions at temperatures below 18 K and above approximately 30 K show a pattern slightly different from the one observed between 20-25 K, proper of a pure crystalline phase with long-range positional order. Patterns for two temperatures, 12 K and 35 K, are shown in Figure 2.12. Both patterns present the coexistence of rings and peaks elongated along the circumference of the rings. Such patterns are not proper for either a fully crystalline solid phase or a liquid phase. It is therefore possible that these particular patterns describe the presence of a transient configuration which could have a character close to a hexatic phase. Since the geometry of the experiment is not ideal for the study of such kind of complex crystalline configuration, as a first approximation we performed diffraction simulations with two different atomic dispositions: one which resembles a pure hexatic phase and another where the in-plane orientation of the hexatic is combined with an out-of-plane partial orientation typical of liquid crystal characters. The simulation is performed in a brute-force approach, evaluating the interference from each atom for each pixel of the simulated detector. The simulation algorithm used does not allow for an accurate estimation of the intensities of the diffraction features but allows for a qualitative comparison of their shape and position. The simulated system in the hexatic phase is composed of crystallites of Argon with a thickness of 11 Å and a diameter of 80 Å. In the first case, the crystallites are disposed on a triangular lattice with a lattice constant slightly bigger than the crystallite diameter and a total size of  $3200 \times 3200 \text{ Å}^2$ . A random distance from the lattice point is introduced to simulate the effect of the short-range positional order. The orientation of the crystallites is the same for all crystallites. In the hexatic combined with liquid crystal disposition, a rotation along the zone axis of graphite is introduced, with a normal distribution of angles centered around 0 and a standard deviation of 0.08 rad. Comparing the simulations with the experimental data, we clearly observe that between the two simulated configurations, the one with hexatic combined with liquid crystals is the one that better resembles the experimental patterns. Therefore we think that our intermediate configurations observed below 18 K and above 30 K exhibit characters similar to an hexatic phase combined with the partial out-of-plane orientation of liquid crystals.

The presence of atom vacancies and dislocations can induce the formation of crystallites with short-range positional order and quasi-long-range orientational order in-plane [42]. An out-of-plane component is present and it's responsible for the elongation of the peaks along the circumference of the rings which we related to the presence of a few Argon layers and islands.

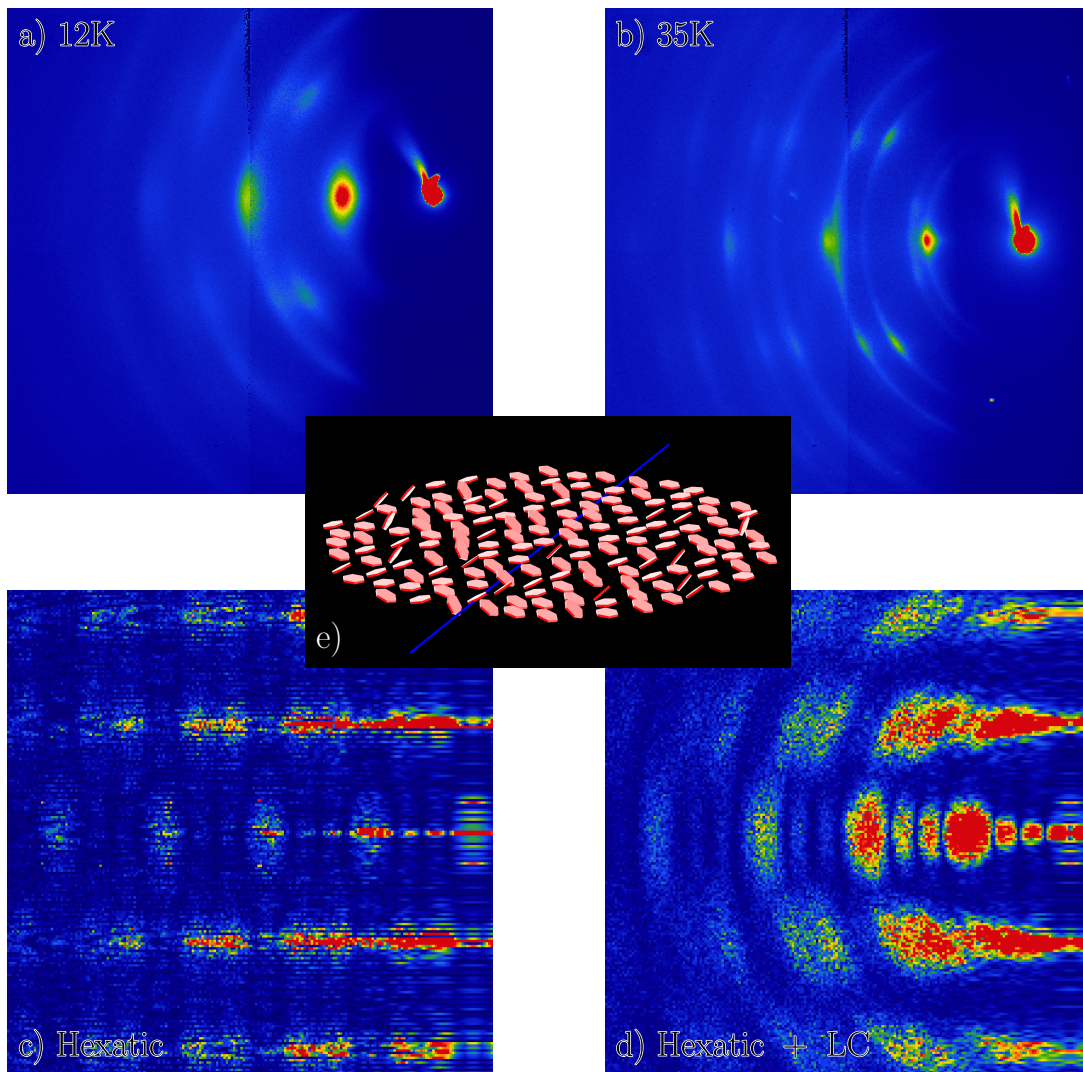


**Figure 2.12:** Experimental (a-b) patterns for two deposition temperatures, 12K and 35K. Panel (c), simulated reflection pattern of the hexatic configuration, (d) simulated pattern of the hexatic configuration with a tilt of the crystallites along the electron beam axis. e) Exaggerated view of a portion of the liquid crystal configuration used in the simulation with the axis of rotation/direction of electron beam marked in blue.

## 2.6 Deposition kinetics diagram of Argon films

To construct a deposition kinetics diagram for the deposition process, the experiment is repeated in a range of temperatures from 10 K to 40 K. For each deposition, the  $p_0$  is reported in a graph versus the deposition temperature, and the depositions are performed on the substrates exhibiting the incommensurate phase. The resulting graph is shown in Figure 2.13. The general behavior is an increase of the deposition

## Chapter 2. Argon thin films

pressure with the temperature, with a minimum deposition pressure of  $2 \times 10^{-8}$  mbar at low temperatures. At pressures below  $p_0$  the adsorption is very little so no substantial change in the diffraction pattern of graphite is noticed, therefore in these regimes, Ar can be considered as a gas (G). At pressures above  $p_0$  the diagram can be divided into three regions: at temperatures between 19 K and 30 K the pattern shows diffraction spots proper of a long-ranged 3D solid phase (S) which is shown to be mostly incommensurate with the chance of commensurate one, while in areas outside this interval, the pattern incorporates as well partial rings and elongation of the diffraction peaks. Such a pattern could be associated with the presence of a hexatic characters (H) in combination with a liquid crystal (LC) configuration, as seen from the simulations. The inset shows our data together with the phase diagram from the work of Maiga *et al.*[27] on graphene. As they point out the graphene curve presents a shift to higher pressures compared to the graphite one in their simulations, but the general trend is the same.

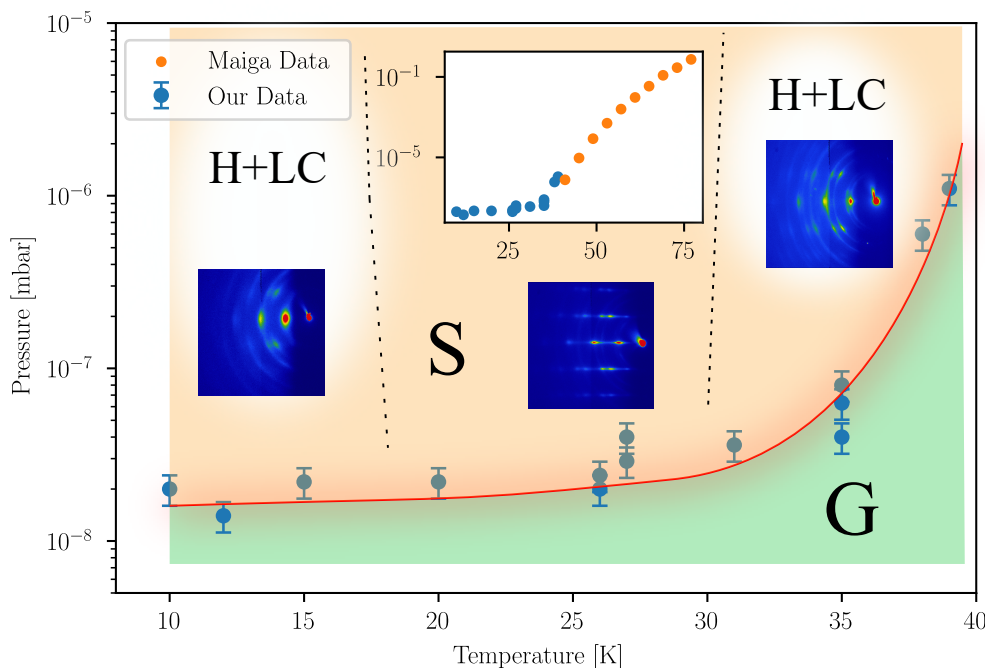


**Figure 2.13:** Deposition kinetics diagram. The red line is an eye guide to identify boundary between the gas phase (G) and the adsorbed configurations. The dashed lines represent hypothetical boundaries between mixed configurations (H+LC) and solid (S). The inset shows our data together with the data simulated by Maiga *et al.*[27].

## 2.7 Thermodynamic melting process

Now we focus our attention on the thermodynamic melting process by increasing the temperature of the system quasi-adiabatically above the melting temperature.

The sample is heated at a speed of 0.5 K/min. Figure 2.14 reports the melting process after a deposition at 24 K and maximum pressure of  $5 \times 10^{-7}$  mbar. In the same way as before, panels (a-e) show the diffraction pattern of the sample captured at the temperatures marked by the black dashed lines in panels (f) and (g).

The bottom panels show the height of the [222] Ar peak with its FWHM in the OOP direction in panel (f) and the calculated NN distance and interlayer distance in panel (g). The pattern initially shows a 3D solid with elongated peaks due to the layered structure at the starting temperature slightly above 24 K. The increasing temperature does not create any considerable effect until reaching 30 K, except for a slight decrease in the height of the peak. Above this temperature, at around 33 K, the interlayer distance decreases slowly, accelerating with higher temperatures, sign of relaxation of the structure in the OOP direction while the IP NN distance remains constant. Such relaxation reaches a minimum above 35K at which point the pattern suffers a considerable change with the disappearing of the peaks elongation, visible also from the decreasing of the FWHM. The system transitions to a fully ordered 3D islands structure with transmission spots. The height of the diffraction peaks then drops quickly and the pattern disappears completely close to 36K, the melting point, leaving only a faint ring which persists until 45 K. Such a ring was almost invisible at 25 K but its intensity increases with temperature and its position is strictly related to the [111] peak position. The presence of this ring can be associated to the existence of a liquid phase. Since a liquid does not possess positional and orientational long-range order, the diffraction pattern associated with this phase would be a ring with its radius related to the average distance between the atoms/particles. In this case, such a distance would be the same as the interlayer distance, around 3.53 Å which is too small for the Ar-Ar Lennard-Jones  $r_0 = 3.72$  Å. A second explanation for the ring could be that defects on the graphite surface can trap small crystallites of Argon in random orientations that cannot desorb as easily as the ones in the flat areas and require higher temperatures. Since such quantities are small and the experiment is performed at grazing incidence higher order rings, if present, are too faint to be visible so from this data it is not possible to distinguish between the two explanations.

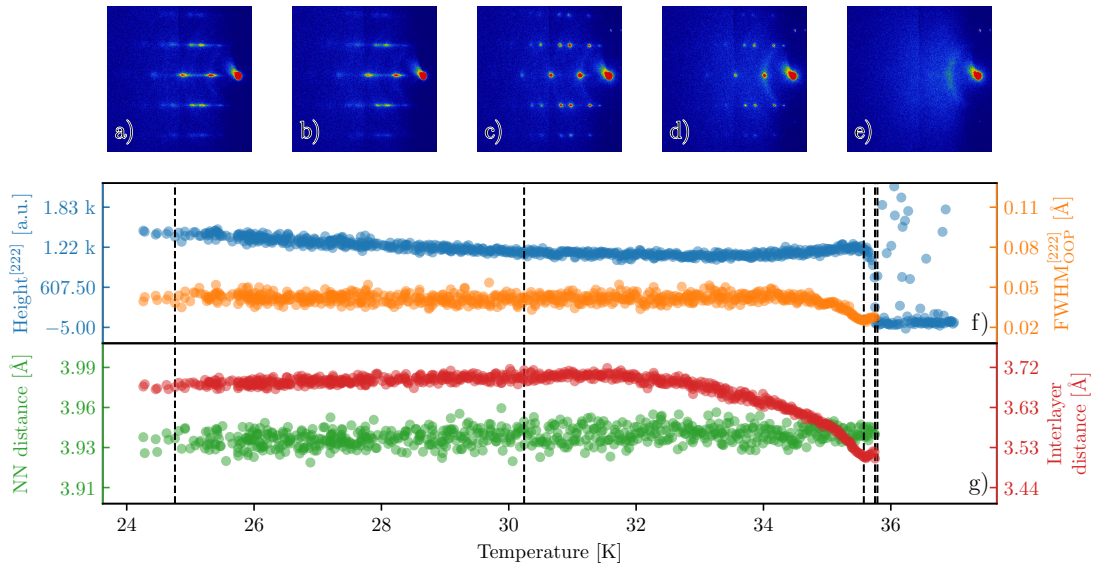


**Figure 2.14:** Diffraction pattern evolution during slow melting (a-e) and the height of the [222] Ar peak with its FWHM in the OOP direction (f) and the calculated NN distance and interlayer distance (g) during the same process.

Our data suggest that the Argon films are the first to melt in contrast to the 3D islands nucleated around the defects which remain resilient until the melting point leading to the transmission spots. The melting of the films exhibits a continuous transition between 30 and 35 K, while the 3D islands show a first-order transition denoted by the abrupt change in the peak parameters around 36 K. This observation is in agreement with the two peaks observed by Migone in specific heat measurements [35] where the broader one is associated with the continuous melting and the sharp one with a weak first-order transition. In our case, the continuous melting happens before the first-order transition, which we speculate is due to the different ranges in temperature and pressure. The melted Argon could be either in a liquid phase or a gas phase. We suspect that it is in the isotropic liquid phase.

## 2.8 Conclusions

This work demonstrates the capability of RHEED to investigate the deposition and the melting processes of Argon on graphite based on structural transformation in a regime of temperatures and pressures so far never explored.

We revealed that the growth process is similar to a Stranski-Krastanov one where the adsorption of one monolayer is followed by a growth of 3D islands pinned to surface defects.

The solid phase is an FCC structure following ABC stacking with a NN distance of 3.95 Å, which is consistent with an incommensurate phase, predicted and observed in previous works.

For the first time, a commensurate phase with a NN distance of 4.26 Å is reported by us. We attribute this phase to the quality of the substrate since it manifests only in a specific batch of samples with higher quality.

The deposition performed in a temperature range between 10 and 40 K revealed the presence of a crystalline configuration exhibiting mixed traits between an hexatic phase and a liquid crystal one at temperatures below 18 K and above 30 K. We report a deposition kinetics diagram in a range of temperatures and pressures that has been never reported before.

The melting process of the Argon films shows a two-fold mechanism: a continuous melting of the films followed by a first-order transition of the 3D islands.

## 2.9 Perspectives and outlook

To achieve a layer-by-layer deposition we suggest the use of samples with a high degree of flatness and coherence of the surface. We propose to anneal the samples in vacuum at 1000 K to relax the structure, thus reducing the defects on the surface.

To favor the deposition in a commensurate phase we suggest the use of substrates with very good quality without domains, ideally monocrystalline.

A highly interesting prototypical 2D system with exotic thermodynamic properties can be explored by replacing Argon with helium. At very low temperatures, helium admits a small zero-point energy which gives rise to quantum effects that can generate a quantum phase transition in two dimensions.

The melting of the films showed an interesting behavior with the continuous melting of the films followed by the abrupt melting of the 3D islands. We propose to perform a time-resolved experiment to investigate the melting process in more detail. We carry out such investigation in the following chapter and we illustrate the results we found.





# 3 Ultrafast dynamics of Ar films on graphite

## 3.1 Introduction

In this chapter, we focus our interest on out-of-equilibrium phenomena in argon films adsorbed on graphite. We aim to investigate the structural changes of the films under ultrafast pulsed excitations by means of Ultrafast Reflection High Energy Electron Diffraction (URHEED) and reveal their dynamics involved in the relaxation processes. So far this kind of investigation on argon films adsorbed on graphite has never been conducted, thus any ultrafast dynamics observed will have major importance in the physics of melting in 2D systems.

In this project, we use the photon energy of 1.55 eV (800 nm) to pump the system and the electrons at 30 keV to probe the dynamical structural changes.

Argon interacts via Van der Waals forces, there are no shared electrons between Ar-Ar and Ar-C atoms. As a consequence, there will not be any available electronic or phononic excitation in the range of energies between UV and near-infrared. Thus argon cannot absorb photons in this energy range. For this reason, we exclude any possible dynamics faster than some tens of ps.

However, graphite (the substrate) is the only component of the system that absorbs this light, generating electronic and phononic excitations which can propagate and be transferred to the argon films, leading to possible ultrafast dynamics.

## 3.2 Experimental procedure

In this section, we will discuss the experimental protocol adopted to conduct pump-probe measurements on argon films adsorbed on graphite. We start with the procedure of the spatial and temporal overlap determination; secondly, we investigate the

dynamics of graphite and, finally, we explore the dynamics of argon films.

### 3.2.1 Spatial and temporal overlap determination

Before any pump-probe experiment, the determination of the spatial and temporal overlap is a crucial step. The pump and the probe beams must converge to a single point in space and time. The point at which this condition is met is called time zero  $t_0$ .

An efficient method to determine spatial and temporal overlap is to use the plasma-lensing effect [43] on the electron beam. We generate the plasma by focusing ultrashort laser pulses on a copper target. The electric field of the plasma is strong enough to deflect our electron beam and when the laser pulses and the electron pulses are in spatial and temporal overlap the deflection is visible on the detector as a displacement of part of the beam, see Figure 3.2d.

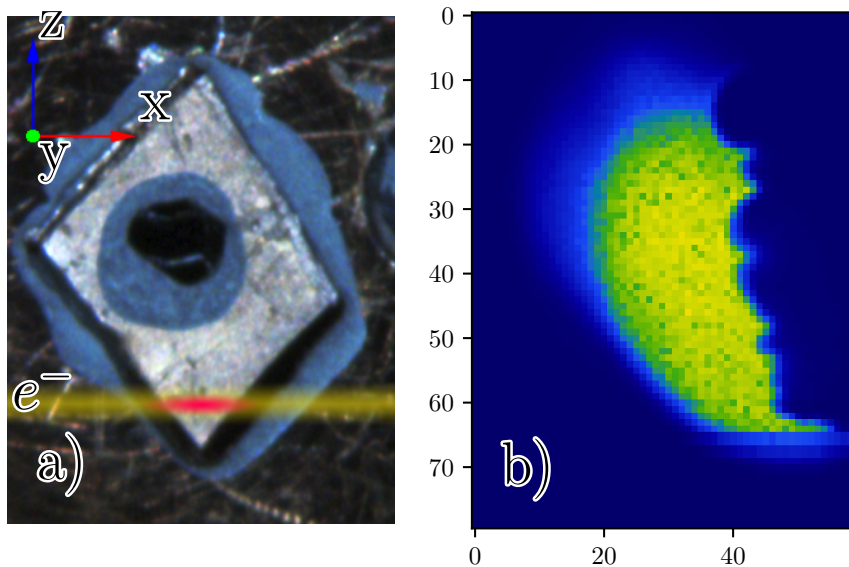


**Figure 3.1:** a) Picture of a sample on the sample holder with the schematic representation of the electron beam and the pump laser on the corner of the copper plaque. b) Picture of the collimated electron beam being clipped by the copper plaque (shadow on the right).

The generation of the plasma leaves a superficial charge  $\sigma$  on the surface of the target. Since  $\sigma \propto 1/R$ , where  $R$  is the radius of curvature of the target, a sharp object will generate a stronger and more localized electric field than a flat surface. We exploit the fact that our sample is mounted on a square copper plaque to use the sharpness of its corners to intensify the plasma. A schematic representation is depicted in Figure 3.1a, where the sample holder is moved along  $y$  and  $z$  to clip the beam and position it on the corner of the plaque. Figure 3.1b shows the shadow of the

copper plaquette and it can be seen that the edge is not particularly flat but presents some scratches and irregularities. Ultimately this does not constitute a problem since asperities will increase the localized electric field. The fact that the plaquette is oriented as in the picture presents another advantage: the position in  $z$  can be adjusted so the portion of the area illuminated by the laser is as long as the sample in order to achieve the same spatial overlap. To see the plasma generation we perform

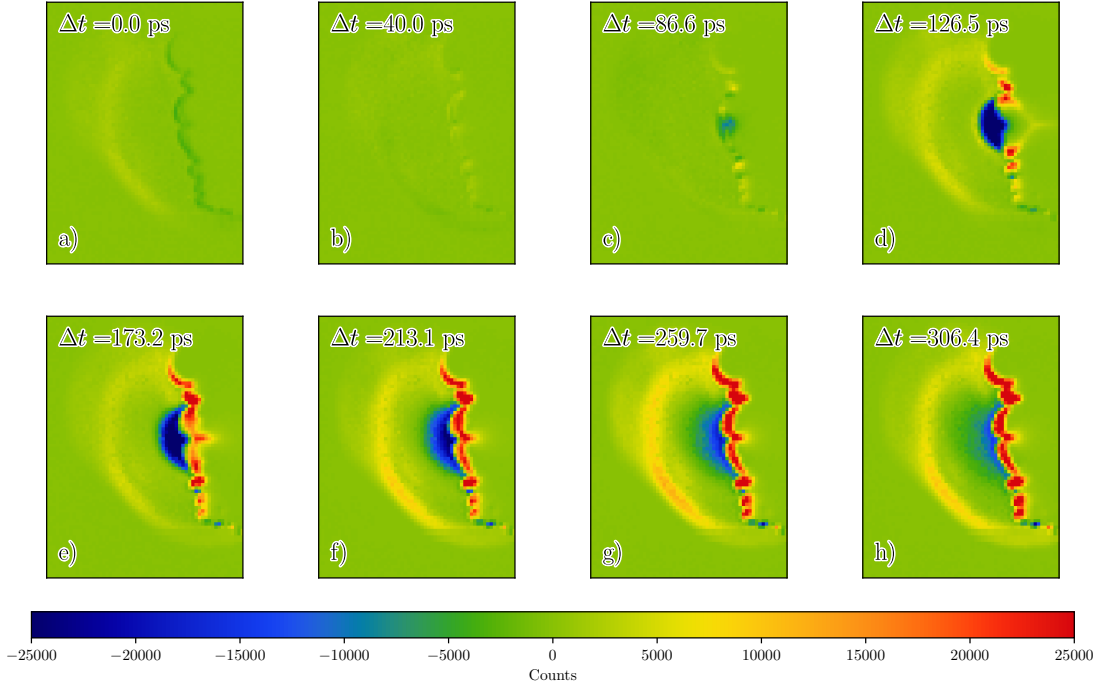


**Figure 3.2:** Effect of the plasma on the electron beam at different times from an arbitrary time before the plasma generation.

a scan changing the delay between the pump and the probe pulses and we observe the effect on the electron beam as in Figure 3.2. The resulting lensing effect consists of a displacement of the electrons leaving a hole (blue area) in the beam and with increased counts in other areas (red areas) since the charge must be conserved.

A simple model to represent the two effects is the following: the electron pulse is a Gaussian  $G(t; \mu, \sigma)$  with a center  $\mu$  in time and a width  $\sigma$ ; given its fast generation the plasma can be considered as instantaneous with an exponential decay  $\Gamma(t; \lambda)$  with lifetime  $\tau$  and rate  $\lambda = \frac{1}{\tau}$ . The two functions are represented in Figure 3.3a. The result of the interaction between the electron pulse and the plasma can be retrieved by convolving the two functions; for this simple model this can be done analytically:

$$f(\tau; \mu, \sigma, \lambda) = (G * \Gamma)(t) = A \frac{\lambda}{2} \exp\left\{\left(\frac{\lambda}{2}(2\mu + \lambda\sigma^2 - 2t)\right)\right\} \operatorname{erfc}\left(\frac{\mu + \lambda\sigma^2 - t}{\sqrt{2}\sigma}\right) \quad (3.1)$$

### Chapter 3. Ultrafast dynamics of Ar films on graphite

where  $A$  is a normalization factor and  $\text{erfc}(x)$  is the complementary error function. Equation 3.1 is referred to as an exponentially modified Gaussian distribution. The result of the convolution is shown in Figure 3.3a with the green trace. We take a small ROI inside the hole, typically 3x3 pixels, and average the counts as a function of the delay. The result is shown in Figure 3.3b with the blue dots while the fit is represented by the red line. Despite being a simple model the fit approximates the experimental data in a satisfactory way and the temporal overlap can be retrieved by the fit parameters in the following way: the parameter  $\mu$  defines the moment in time when the center of the Gaussian is at the maximum of the exponential decay but this is not the moment at which the electrons begin to interact with the plasma,  $t_0$ ; taking into account the width of the Gaussian  $\sigma$  we can define the temporal overlap as the time at which a little portion, e. g. 2.5%, of the electron bunch starts to interact with the plasma. This also means that 97.5% of the electrons are still unaffected by the plasma and such percentage corresponds to shifting the entire electron pulse by  $2\sigma$  towards earlier times, Figure 3.3b.

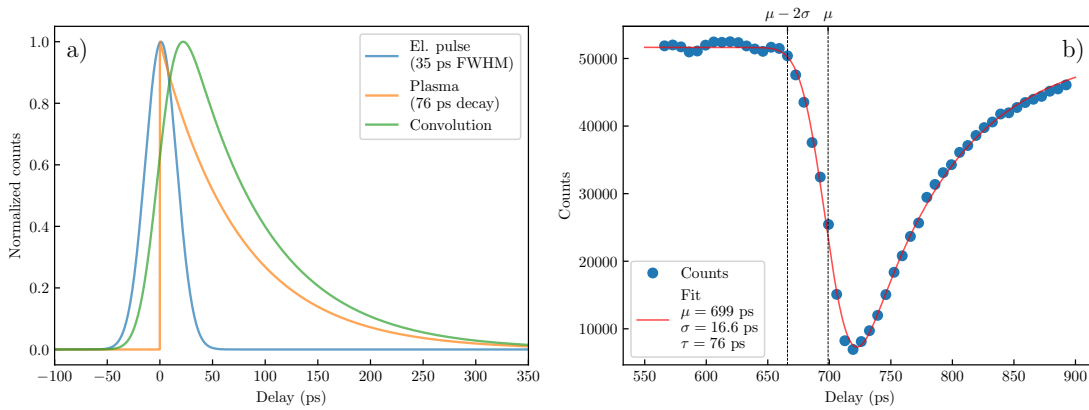


**Figure 3.3:** a) Models of the electron pulse and the plasma with their convolution. b) Data from the time scan and its fit, with  $\mu$  and  $\mu - 2\sigma$  at the dashed lines. The delay is not yet adjusted for  $t_0$  but it's relative to an arbitrary point.

The time resolution can be estimated as the FWHM of the electron pulse as  $2\sqrt{2\ln(2)}\sigma = 39$  ps.

In this case, the electron beam is collimated so the plasma-lensing effect can be easily visible, and this allows for the improvement of the spatial overlap: the pump beam can be moved independently from the electron beam, therefore, at times around  $t_0$ , the hole can be moved to be centered on the beam. Provided a correct alignment of the solenoids, the pump and probe beams will maintain the spatial and temporal overlap also after the beam is focussed on the detector.

To ensure the best possible measurement conditions, we refine the overlap by per-

forming the same scan on graphite, which has a known fast dynamic, and we adjust the parameters to maximize the observed effects. For our pump-probe measurement, the typical diameter of our probe beam at the position of the sample is approximately 500  $\mu\text{m}$  and its footprint on the sample spans along the length of the sample, 2 mm. We always make sure that the pump beam is bigger than the probed area to ensure a homogeneous effect of the photoexcitation.

### 3.3 Ultrafast dynamics of graphite

The ultrafast dynamics of graphite is shown in Figure 3.4. Panel a shows the intensity of the (0014) Bragg peak as a function of the delay between the pump (800 nm) and probe pulses. The intensity exhibits a drop of around 70% in a timescale of 10-20 ps for a fluence of 44.5 mJ/cm<sup>2</sup>. This drop indicates a significant disorder induced by the photoexcitation [44], and lasts at least up to 700 ps without showing a recovery toward the initial state. As described in the work Carbone *et al.* the drop in intensity depends strongly on the fluence used for the photoexcitation [45, 46].

Following the position of the same Bragg peak, information about compression/expansion of the lattice can be extracted. In case of graphite, the lattice expands by around 8 pm in the first 100 ps after the photoexcitation Figure 3.4b. Differently from the intensity, the expansion starts a slow relaxation at approximately 200 ps but at 700 ps it is still not yet fully recovered. The timescale of the relaxation is indicative of phononic origin. In the same paper, the authors demonstrated the presence of a coherent oscillation in the lattice expansion along  $c$ -axis, with a period of  $\approx 1$  ps, see Figure 3.5a, which is assigned to the shear mode  $E_{2g}$  at 43 cm<sup>-1</sup>. The interlayer expansion follows a compression that is expected to occur with a characteristic time of around 500 fs, depending on the photoexcitation fluence. Refined measurements on HOPG with better time resolution revealed this fast dynamic confirming that it occurs as fast as 500 fs [16], see Figure 3.5. The 1.5 eV photons excite electrons around the  $M$  point in the graphite bands, from a bonding  $\pi$  band to the antibonding  $\pi^*$  band, resulting in an effective weakening of the bond along  $c$ -axis generating the compression. A visual representation of the dynamic is shown in Figure 3.6.

Before investigating the ultrafast dynamics of argon films we explore first the dynamics of our substrate, natural graphite, at room temperature and low temperature (the temperature of the deposition of the films). Below, in Figure 3.7 we show the results for the temperatures of 300 K, red line, and 20 K, blue line. We can observe the same dynamics as the higher fluence case but less pronounced. The drop in peak intensity and

### Chapter 3. Ultrafast dynamics of Ar films on graphite

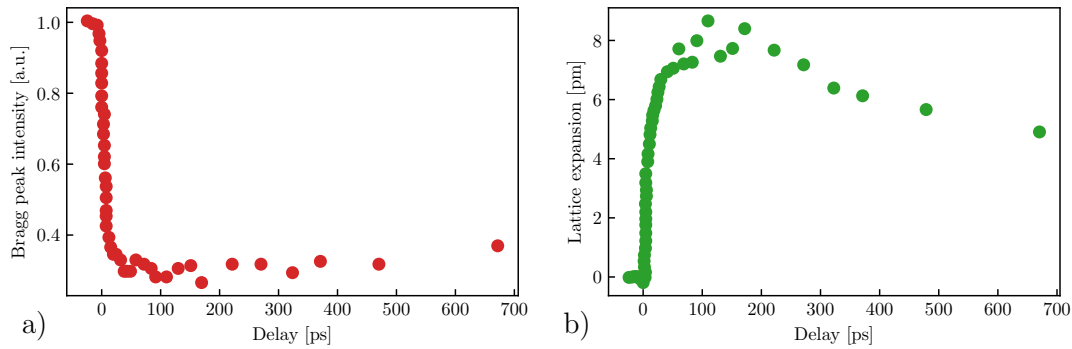


**Figure 3.4:** Ultrafast dynamics on HOPG graphite at fluence of  $44.5 \text{ mJ/cm}^2$  at 300 K retrieved from the (0 0 14) Bragg peak. a) Bragg peak intensity, b) lattice expansion. Data digitized from [45]

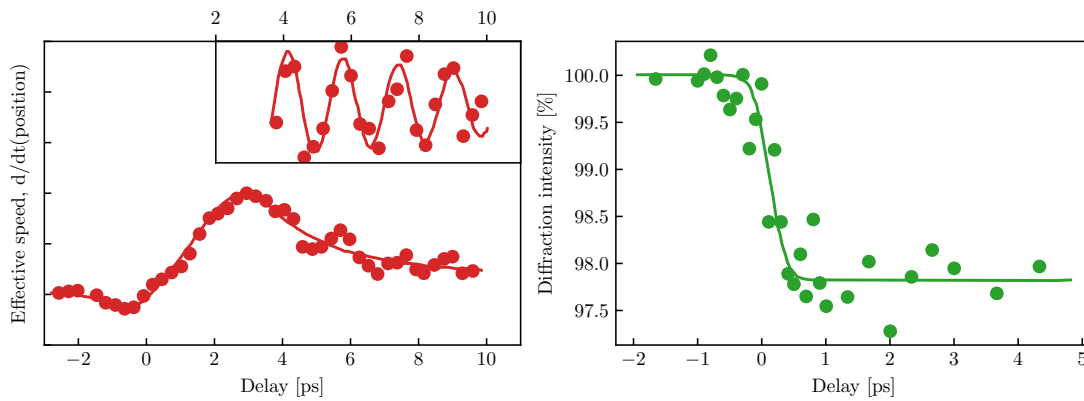


**Figure 3.5:** Ultrafast dynamics on HOPG graphite. a) Effective speed of the peak as  $d/dt(\text{position})$ , inset with coherent oscillations, from [45]. b) Electronic dynamics of HOPG graphite, from [16]

the displacement along the  $c$ -axis are consistent with what we described previously. The expected dynamics of argon films is of the order of 100 ps, therefore we decided to work with a lower time resolution (without utilizing the RF pulse compression system) to try to minimize the sources of noise and beam drifts.

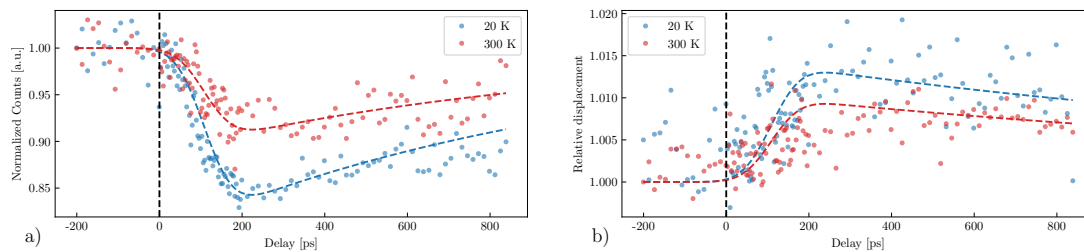


**Figure 3.7:** Graphite dynamics at 300 K /blue) and 22K (red) at a fluence of  $1.6 \text{ mJ/cm}^2$ : a) intensity of the [006] peak, b) displacement. The lines are eye guides.

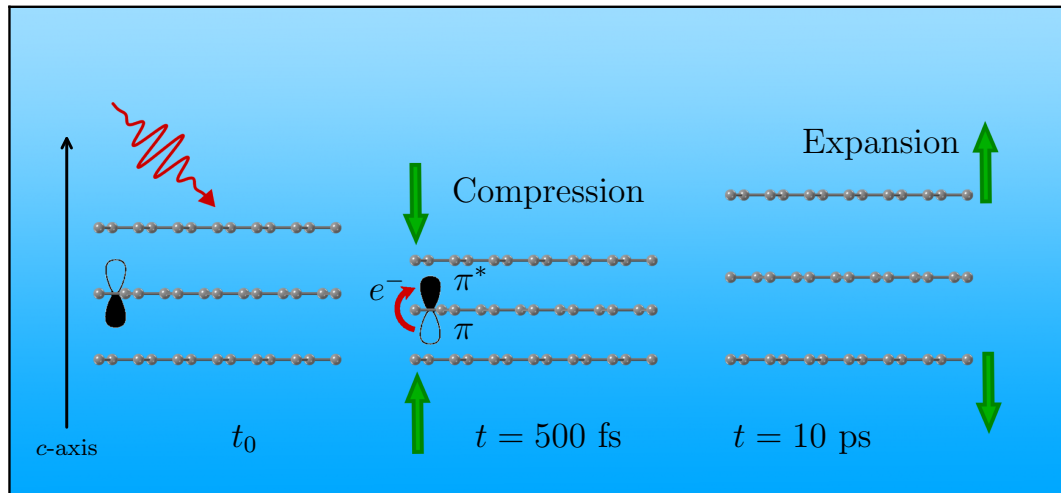


**Figure 3.6:** Sketch of the lattice dynamics on graphite at different times after the photoexcitation, with the change of the  $\pi$  orbital from bonding to antibonding, adapted from [45]

### 3.4 Ultrafast dynamics of argon thin films

We perform the time-resolved experiment on argon films adsorbed on graphite in the solid phase, indicated in the deposition kinetics diagram by the red dashed line at  $T = 20$  K, see Figure 3.8. We used 1.55 eV (800 nm) laser pulses with 45 fs pulse duration. The deposition conditions of these films are: temperature of the substrate  $T = 20$  K, maximum pressure of argon  $p = 1 \times 10^{-6}$  mbar. The determination of the right fluences for our pump was highly challenging because of two main constraints: we wanted to use the highest possible fluence to maximize the effect on graphite, and thus on the argon films, but we also wanted to avoid desorption of the films due to heating from the pump. We observed that at fluences higher than  $3.5 \text{ mJ}/\text{cm}^2$  the argon films start desorbing quickly and the graphite peaks appear again, see Figure 3.9a and b. For lower fluences the desorption process is still present but slower. Therefore we limit our total acquisition time accordingly, which affects the signal-to-noise ratio of the experiment.

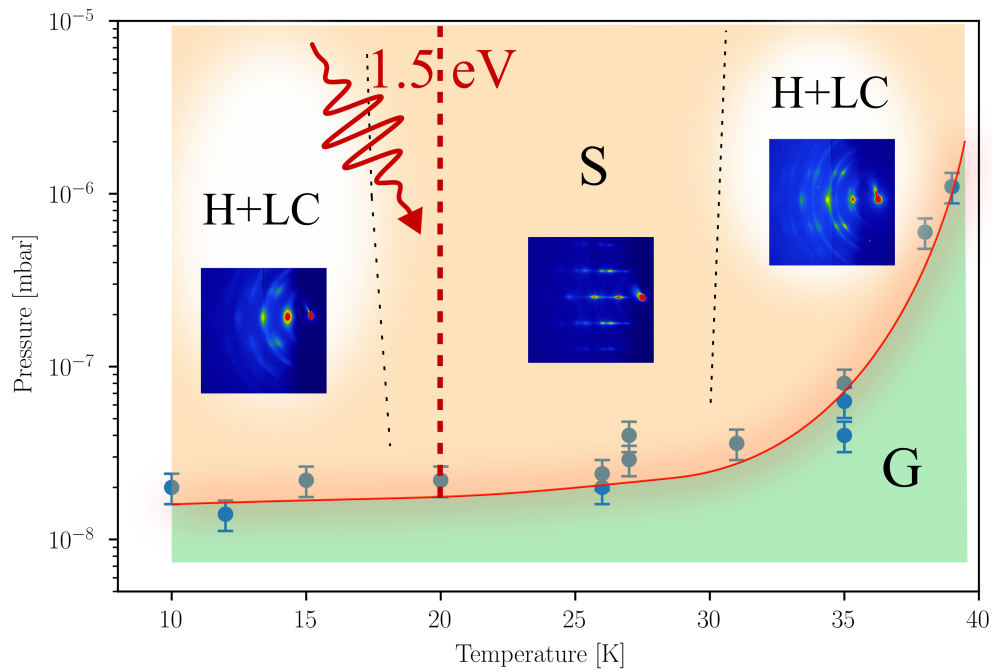


**Figure 3.8:** Deposition kinetics diagram of argon adsorbed on graphite. The red dashed line indicates the temperature at which we perform the photoexcitation.

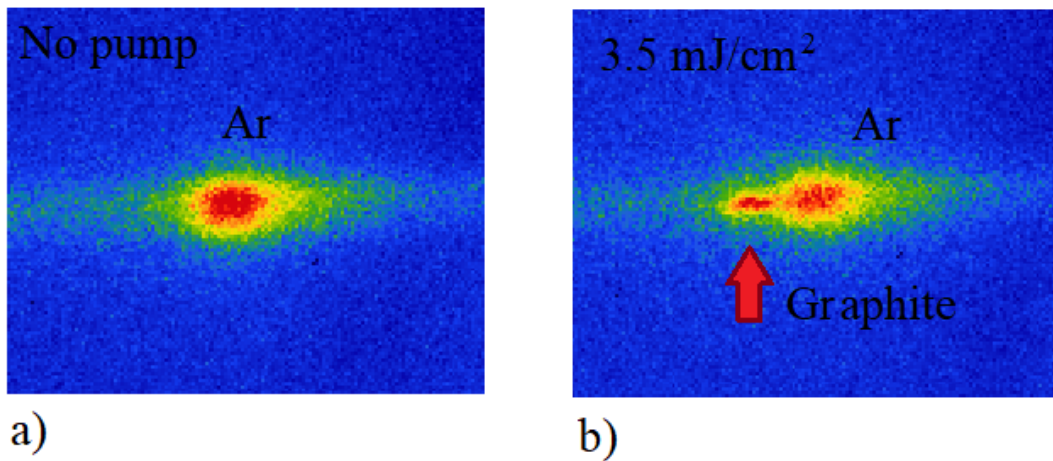


**Figure 3.9:** Diffraction peak of Ar films a) after the deposition without pump beam, b) with pump beam at  $3.5 \text{ mJ/cm}^2$  of fluence. The peak of graphite is visible on the left side of the argon peak.

In Figure 3.10 we present time-resolved data of argon films at 20 K and fluence of  $1.6 \text{ mJ/cm}^2$ . The main result of argon dynamics it's observable in the position shift of the



### 3.4 Ultrafast dynamics of argon thin films

[333] Bragg peak of argon, see panel b. We notice a positive shift that starts after 150 ps and lasts approximately until 500-600 ps. The high level of noise present in the data does not allow us to be accurate in the determination of the lifetime. We note that nothing is visible at  $t_0$ . In the intensity graph, Figure 3.10a, it is less apparent the presence of dynamics, but we suspect that a decrease may be present around 100 ps. We don't see any noticeable dynamics after the photoexcitation in the FWHM, see Figure 3.10c. The possible intensity drop at 100 ps could be justified by the disorder created in the graphite layer within 10 ps after the photoexcitation Figure 3.4, which, by consequence, transfer this disorder to the argon sites since the argon atoms are constrained by the honeycomb lattice of graphite.

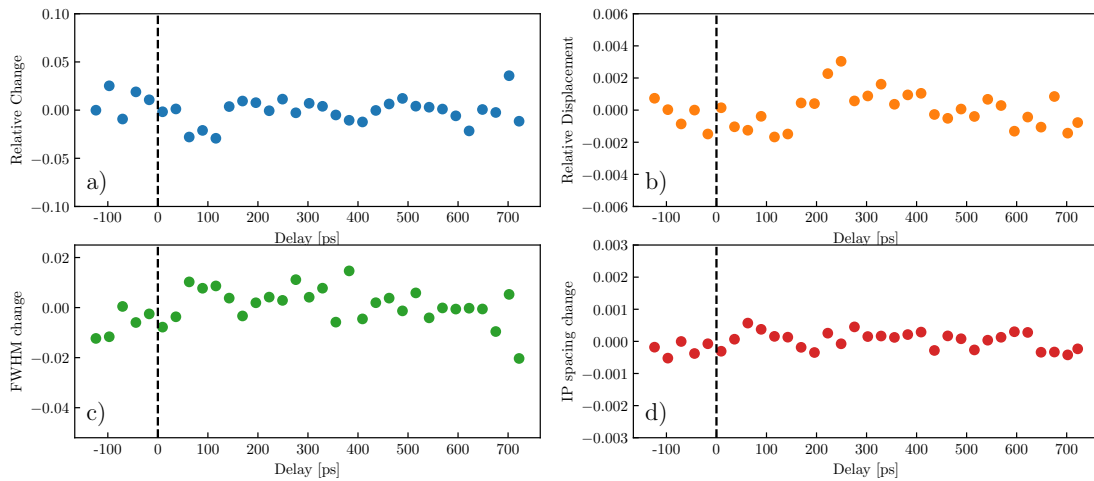


**Figure 3.10:** Pump-probe experiment on adsorbed argon at 20 K and fluence of  $1.6 \text{ mJ/cm}^2$ : a) intensity of the [333] peak, b) relative displacement, c) FWHM change, d) in-plane lattice spacing change. The black lines mark the  $t_0$  position.

The observable shift of the argon peak at 150 ps, calculated with Equation 1.8, indicates an expansion along the [333] direction of the argon films. This expansion occurs only between the layers since we don't observe any change in the in-plane lattice spacing, see Figure 3.10d. One possible explanation for this expansion is that, as we presented previously, it is a reaction to the dynamics of the graphite. After the photoexcitation of 1.55 eV, an electronic excitation from the band  $\pi$  to  $\pi^*$  is created in a time of 500 fs. After the compression, the graphite starts expanding in a timescale from 10 to 100 ps along the  $c$ -axis. The expansion is accompanied by the propagation of an acoustic wave along the  $c$ -axis which will be transferred from the graphite to the argon films. The observed expansion of the argon films is the reaction to the expansion of the graphite, and the delay between the two is justified by the time needed for the propagation of the acoustic wave from the graphite to the films. We represent this

### Chapter 3. Ultrafast dynamics of Ar films on graphite

process in Figure 3.11.

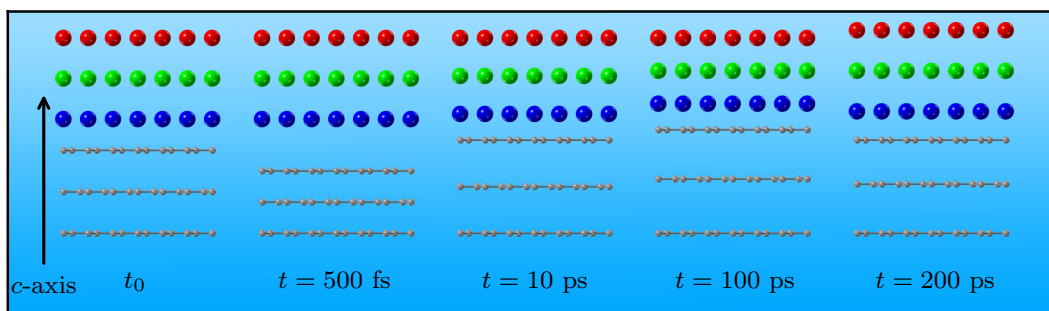


**Figure 3.11:** Schematics of the proposed plane dynamics, greatly exaggerated for clarity.

To confirm our results of the expansion dynamics of the argon films we repeated the experiment using different lower fluences, see Figure 3.12. Unfortunately, the used fluences are too small to induce any dynamics on graphite, therefore we cannot observe any dynamics on the argon films.

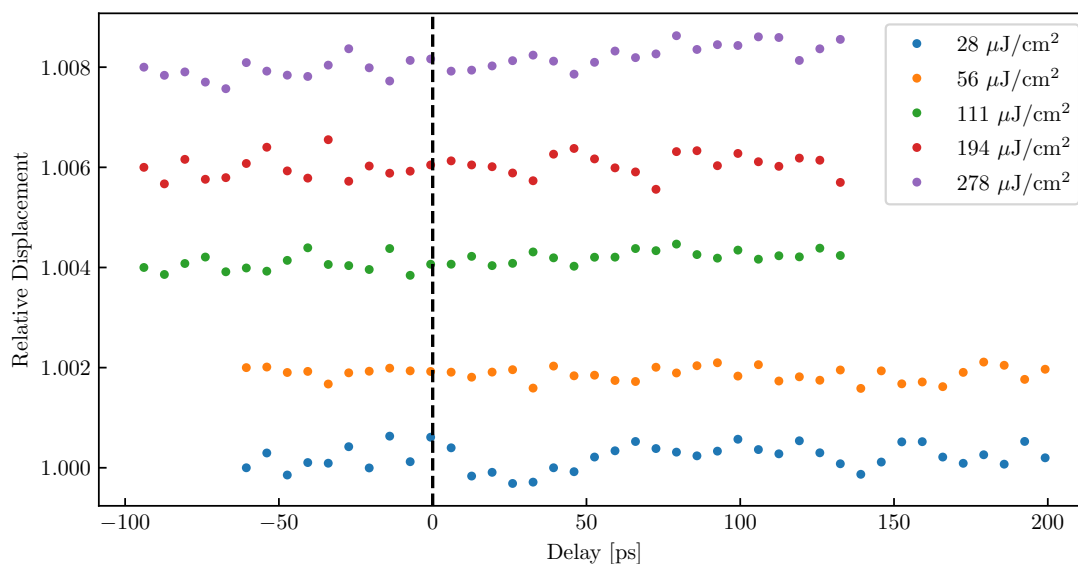


**Figure 3.12:** Pump-probe experiment on adsorbed argon at 20 K at fluences between 28  $\mu\text{J}/\text{cm}^2$  and 278  $\mu\text{J}/\text{cm}^2$ . a) Peak intensity, b) Relative peak displacement, c) Change in the FWHM. The black lines mark the  $t_0$  position.

### 3.5 Conclusions

In conclusion, the pump-probe investigation on argon films adsorbed on graphite revealed that the argon films are influenced by the ultrafast dynamics of graphite. The photoexcitation of 1.55 eV induces an electronic excitation which is followed by an interlayer compression of the graphite planes thanks to strong electron-phonon coupling. This compression evolves in a timescale of 500 fs and it is followed by an expansion that reaches its maximum after approximately 100 ps, generating an acoustic wave propagating along the  $c$ -axis. The adsorbed argon films are affected by this acoustic wave after a timescale of 150 ps, which is translated in a shift of the Bragg peak position in the diffraction pattern.

### 3.6 Outlook

The experiment presents several challenges mainly due to the nature of the probed system. One possible way to maximize the observed effect on the argon films is to repeat the experiment on a system with a mono- or bi-layer of argon. The proximity of these thin layers to the graphite potential would result in a clearer response of the adsorbed gas.

In the link with the previous chapter, it will be interesting to perform time-resolved experiments in the proximity of the mixed crystalline configuration, at low temperature or at high temperature in the proximity of the melting point with the aim to drive this configuration toward another by photoexcitation.

As another intriguing experiment, we propose to investigate the dynamics of graphite and adsorbed argon at a high angle of incidence where a higher penetration depth of the electrons would allow monitoring diffraction peaks from both graphite and argon. It would be interesting to see how the dynamics of graphite are influenced by the adsorbed gas.

Furthermore, we propose to replace the argon with lighter gases, such as neon and helium, expecting more pronounced ultrafast effects, while heavier gases, such as krypton and xenon, would lead to smaller effects and slower dynamics.



# 4 Ultrafast generation of hidden phases via energy-tuned electronic photoexcitation in magnetite

## 4.1 Introduction

Magnetite, with its chemical formula  $\text{Fe}_3\text{O}_4$ , is a compound member of the transition metal oxides class. It has been discovered more than 2500 years ago as the first magnetic material and its uncommon properties propelled our civilization towards considerable discoveries and technological advancements. In 1939, the Dutch chemist Verwey found a up to 2 orders of magnitude discontinuity in the temperature dependence of the electrical resistivity [47]. This discontinuity was also dependent on the stoichiometry of the compound (Figure 4.1) and the transition temperature, called Verwey temperature  $T_V$  associated with this discontinuity, was found to be in a range between 100 K and 120 K [48].

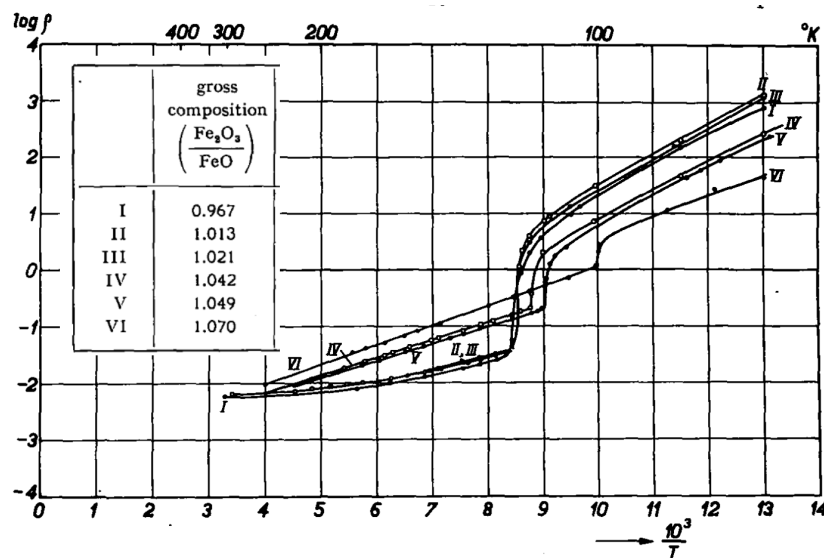


Figure 4.1: Resistivities of different magnetite compounds as a function of temperature [48].

## Chapter 4. Ultrafast generation of hidden phases via energy-tuned electronic photoexcitation in magnetite

---

Due to the discontinuity in resistivity, the low-temperature (LT) and high-temperature (HT) phases are referred to as insulator and conductive phases, respectively, therefore, the Verwey transition (VT) can be referred to as a metal-insulator transition (MIT).

Bragg determined that the structure of magnetite is a spinel with the form  $AB_2O_4$  where A and B are two non-equivalent metal cations *et al.* [49]. In 1947 Verwey proposed instead an inverse spinel structure, in order to account for the discontinuity in the resistivity. In such a structure A is the  $Fe^{2+}$  cation occupying the tetrahedral sites and the B octahedral sites are occupied by both  $Fe^{2+}$  and  $Fe^{3+}$  cations. This particular arrangement results in the formation of a charge-order observed later by Weng *et al.* [50], which explains the change in resistivity. Despite the agreement with the conductivity and diffraction data, this model failed to explain the transition from a cubic  $Fd\bar{3}m$  structure at HT to a monoclinic  $Cc$  at LT with a small tilt angle of  $90.20^\circ$  observed in neutron diffraction [51]. More steps towards the explanation of the VT were taken by Senn *et al.* with the attribution of a structural distortion to a new bond-dimerized state in combination with Jahn-Teller effect [52] called trimeron, see Figure 4.2. This quasiparticle involves the formation of a bound state between two  $Fe^{3+}$  ions separated by a  $Fe^{2+}$  ion in a linear arrangement through the delocalization of the minority spin electron in the middle ion. At LT the trimerons form an almost perfect Wigner crystal and their fluctuations with increasing temperature are deemed responsible for the VT in the quasi-adiabatic regime, persisting from below  $T_V$  until the Curie temperature and defining the VT as an order-disorder transition [53–56].

The advent of out-of-equilibrium techniques allowed investigation of the speed of the VT and revealed the presence of a hidden phase separation [57]. In this work, we aim to shine new light on the nature of the MIT through the generation of hidden phases thermodynamically inaccessible and investigating the structural response of the system following different electronic excitations. The method we used is the Ultrafast Reflection High Energy Electron Diffraction (URHEED), which allows for direct observation of the structure through the diffraction pattern and the selection of the electronic excitations tuning the energy of the incident light.

The content of this Chapter is adapted from the preprint "Ultrafast generation of hidden phases via energy-tuned electronic photoexcitation in magnetite" by B. Truc, P. Usai, F. Pennacchio, G. Berruto, R. Claude, I. Madan, V. Sala, T. LaGrange, G. M. Vanacore, S. Benhabib, and F. Carbone, arXiv:2210.00070 [58].

It is divided into two main parts: the first one deals with the investigation of the sample in equilibrium conditions and with the subsequent considerations, and the second one is dedicated to the investigation of the sample in out-of-equilibrium conditions.

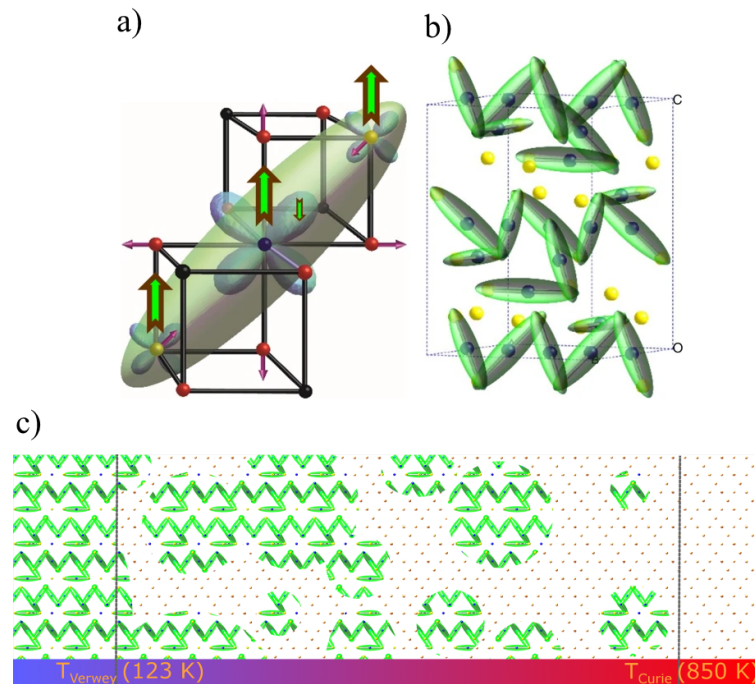


**Figure 4.2:** a) Single trimeron. Fe<sup>2+</sup> and Fe<sup>3+</sup> sites are represented with blue and yellow respectively, the green arrows represent the spin while the purple ones are related to the structural distortions induced by the bonding. b) Long-range order of the trimerons. c) Persistence of the trimerons from below  $T_V$  until the Curie temperature of 850 K, from [55]

This work was started in 2015 by former members of the group and I provided my contribution through the preparation and calibration of the experimental setup, collection of equilibrium data and part of the 800 nm photoexcitation data together with B. Truc and R. Claude, preliminary analysis of ours and previous datasets with B. Truc and simulations of the diffraction patterns. The remaining data presented (400 nm photoexcitation and second 800 nm dataset) were taken by E. Pennacchio and G. Berruto. The project was supervised by I. Madan, V. Sala, G. M. Vanacore, S. Benhabib, and F. Carbone.

## 4.2 Verwey transition in equilibrium conditions

The sample studied in this work is a single-crystal synthetic magnetite polished to achieve optical flatness. The  $T_V$  has been retrieved from resistivity measurements, shown in Figure 4.3a, and it is found to be approximately 117 K. The hysteresis visible between the curves is attributed to irreversible twinning effects. To find the crystal orientation and its lattice parameter x-ray diffraction at room temperature has been used, shown in Figure 4.3b, and the resulting orientation for the out-of-plane direction is [110]. The lattice constant is found to be  $a = 8.385 \text{ \AA}$ .

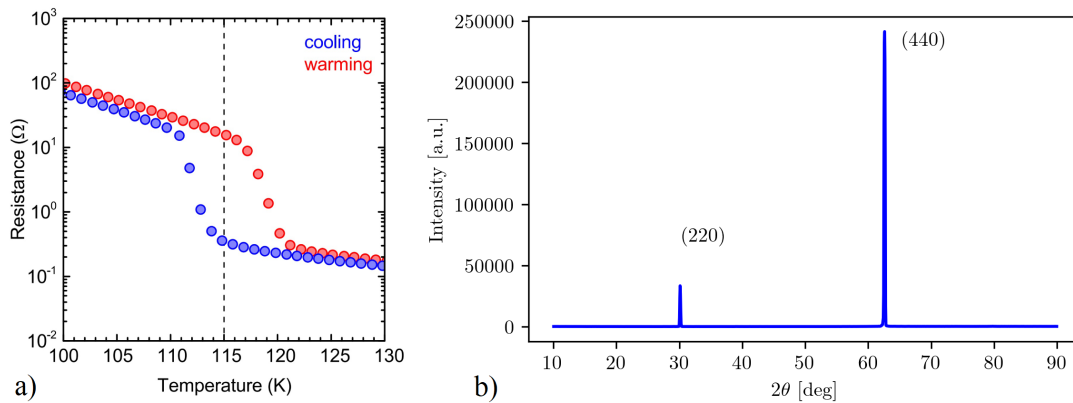


**Figure 4.3:** a) Resistivity of the sample as a function of temperature for heating and cooling ramps. b) X-ray diffraction peaks of the sample at 300 K.

We performed a rocking curve of the sample at room temperature from  $0.5^\circ$  to  $5^\circ$  in the UED setup and its result is shown in Figure 4.4a as a stack of all the frames. The zone axis is identified to be the  $[1\bar{1}0]$  and the peaks are indexed consequently. From now on, the peaks are named with the subscript  $c$  if belonging to the HT cubic phase and with subscript  $m$  if belonging to the LT monoclinic phase. The evolution of the  $(660)_c$  peak is shown in Figure 4.4b as intensity (color) and position (black trace) as a function of the temperature between 300 K and 38 K. It can be seen that the peak, which is sharp and intense at high temperature, suddenly drops in intensity after the transition temperature. Additionally, it shifts in position and gets considerably broader, see also Figure 4.7b, and Figure 4.7c. The changes in intensity and the broadening, especially the increased gaussian contribution to the FWHM, are attributed to the multiple domains and the strain in the LT phase which reduce the coherence length of the crystal. In Figure 4.6a the rocking curve as a function of the scattering angle  $2\theta$  is shown for the LT phase, together with its profile in panel b.



## 4.2 Verwey transition in equilibrium conditions

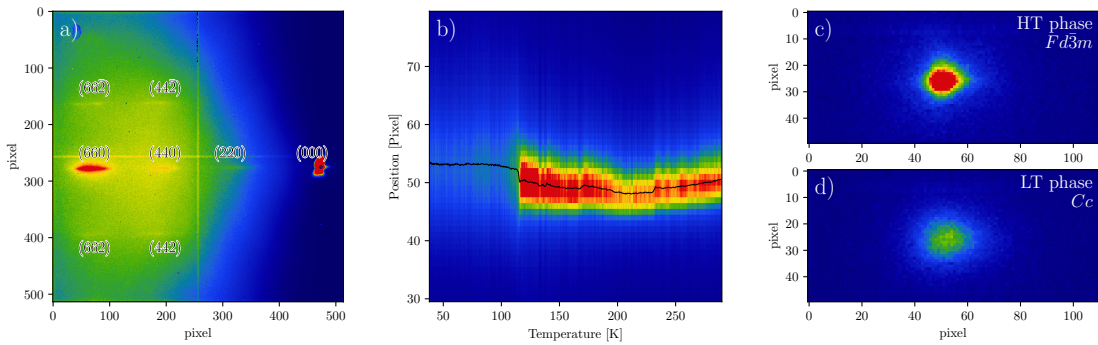


**Figure 4.4:** a) Rocking curve of the sample at room temperature. b) Evolution of  $(660)_c$  peak intensity with temperature. The black line indicates the position of the peak's center. c) and d) Change of the  $(660)_c$  peak before and after the transition.

At low temperatures the only peak that remains resolvable is the highest order, therefore this peak will be the one monitored from now on. Considering the monoclinic structure, the closest peak to the HT  $(660)_c$  with a shorter scattering vector  $q$  would be the  $(\bar{1}200)_m$  corresponding to the zone axis  $[010]_m$ , see Figure 4.5b, while the  $(0120)_m$  overlaps with the  $(660)_c$ . The measured intensity ratio between the two is found to be  $0.62 \pm 0.2$ , with a theoretical value of 0.68. Despite this agreement, only one peak is clearly visible after the transition and more are needed to obtain a correct peak assignment.

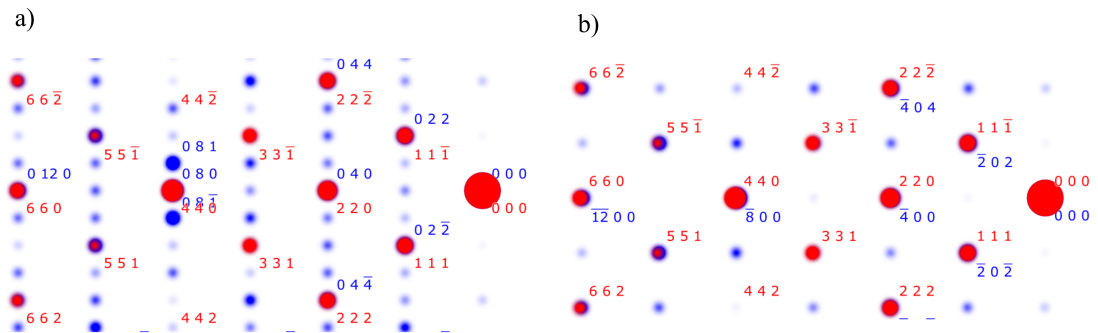


**Figure 4.5:** Simulated patterns of the  $Fd\bar{3}m$  HT (red) and LT  $Cc$  (blue) phases for the  $[\bar{1}10]_c$  zone axis and  $[100]_m$  (a) and  $[010]_m$  (b) zone axes.

The peaks are fitted with a Voigt profile which best approximates the peak shape and allows distinguishing between inhomogeneous (Gaussian) and homogeneous (Lorentzian) broadening contributions. From the evolution of the peak position, it is possible to obtain the change in lattice plane distance  $d$  and with that the strain generated by the transition, Figure 4.7a. As a reference, the value at 150 K is taken and

## Chapter 4. Ultrafast generation of hidden phases via energy-tuned electronic photoexcitation in magnetite

a strain of 1% is found at the lowest temperature, corresponding to an elongation of  $\sim 1$  pm on the [110] direction. Such deformation is consistent with the shear strain component  $\varepsilon_{xy}$  expected in the cubic to monoclinic transition. All the extracted quantities show the character of a first-order transition, while the spikes visible at 170 K and 230 K in the strain are experimental artifacts.

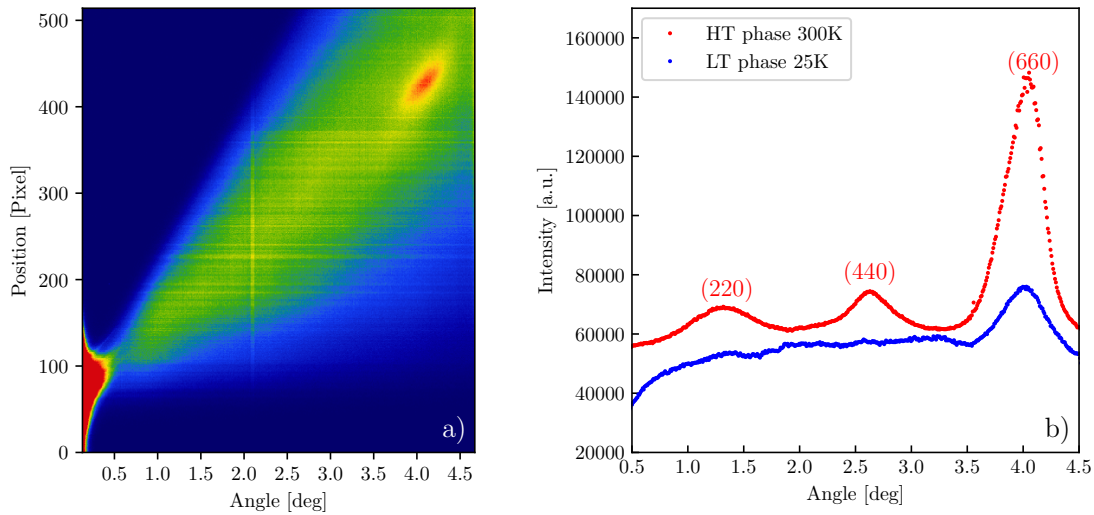


**Figure 4.6:** a) Rocking curve of the sample at room temperature. b) Evolution of (660)<sub>c</sub> peak intensity with temperature. The red line indicates the position of the peak's center. c) and d) Evolution of the (660)<sub>c</sub> peak before and after the transition.

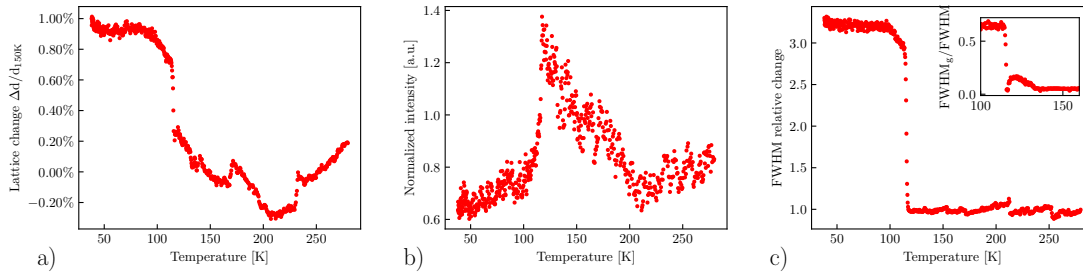


**Figure 4.7:** a) Evolution of the strain in the [110] direction as a function of temperature. b) Evolution of the intensity (integrated area) of the (660)<sub>c</sub> peak as a function of temperature. c) Evolution of the FWHM of the (660)<sub>c</sub> peak as a function of temperature. The inset shows the contribution of the Gaussian to the Voigt with a fluctuation of about 20 K above the transition.

Ultrasound measurements showed a softening of the  $c_{44}$  elastic constant at the Verwey transition, which corresponds to a shear strain [59]. The observation of the strain in the [110] direction is coherent with what was observed in ultrasound measurements and proves that despite our technique is generally not a bulk sensitive one in this case

## 4.2 Verwey transition in equilibrium conditions

it is possible to approximate the system as a bulk one.

The shear strain can be correlated to the order parameter using the Ginzburg-Landau (GL) theory obtaining a constraint on the possible candidates. Denoting the order parameter with  $\Delta$ , the free energy can be expressed as:

$$F = F_0 + \underbrace{g\varepsilon\Delta}_{\text{coupling term}} + \alpha\Delta^2 + \frac{\beta}{2}\Delta^4 + \underbrace{\dots}_{\text{higher order terms}} \quad (4.1)$$

with  $\alpha$  and  $\beta$  as coefficients and  $g$  is the coupling constant. Since the coupling term is an energy as well, it must be invariant under any symmetry operation. For magnetite, whose point group in the HT phase is  $O_h$ , the only possible invariant representation is the  $A_{1g}$ , cfr. Table 4.1.

	E	8C <sub>3</sub>	6C <sub>2</sub>	6C <sub>4</sub>	3C <sub>2</sub> =(C <sub>4</sub> ) <sup>2</sup>	i	6S <sub>4</sub>	8S <sub>6</sub>	3σ <sub>h</sub>	6σ <sub>d</sub>	linear, rotations	quadratic
A <sub>1g</sub>	1	1	1	1	1	1	1	1	1	1		x <sup>2</sup> +y <sup>2</sup> +z <sup>2</sup>
A <sub>2g</sub>	1	1	-1	-1	1	1	-1	1	1	-1		
E <sub>g</sub>	2	-1	0	0	2	2	0	-1	2	0		(2z <sup>2</sup> -x <sup>2</sup> -y <sup>2</sup> , x <sup>2</sup> -y <sup>2</sup> )
T <sub>1g</sub>	3	0	-1	1	-1	3	1	0	-1	-1	(R <sub>x</sub> , R <sub>y</sub> , R <sub>z</sub> )	
T <sub>2g</sub>	3	0	1	-1	-1	3	-1	0	-1	1		(xz, yz, xy)
A <sub>1u</sub>	1	1	1	1	1	-1	-1	-1	-1	-1		
A <sub>2u</sub>	1	1	-1	-1	1	-1	1	-1	-1	1		
E <sub>u</sub>	2	-1	0	0	2	-2	0	1	-2	0		
T <sub>1u</sub>	3	0	-1	1	-1	-3	-1	0	1	1	(x, y, z)	
T <sub>2u</sub>	3	0	1	-1	-1	-3	1	0	1	-1		

**Table 4.1:** Character table of the  $O_h$  point group [60].

	A <sub>1g</sub>	A <sub>2g</sub>	E <sub>g</sub>	T <sub>1g</sub>	T <sub>2g</sub>	A <sub>1u</sub>	A <sub>2u</sub>	E <sub>u</sub>	T <sub>1u</sub>	T <sub>2u</sub>
A <sub>1g</sub>	A <sub>1g</sub>	A <sub>2g</sub>	E <sub>g</sub>	T <sub>1g</sub>	T <sub>2g</sub>	A <sub>1u</sub>	A <sub>2u</sub>	E <sub>u</sub>	T <sub>1u</sub>	T <sub>2u</sub>
A <sub>2g</sub>	A <sub>2g</sub>	A <sub>1g</sub>	E <sub>g</sub>	T <sub>2g</sub>	T <sub>1g</sub>	A <sub>2u</sub>	A <sub>1u</sub>	E <sub>u</sub>	T <sub>2u</sub>	T <sub>1u</sub>
E <sub>g</sub>	E <sub>g</sub>	E <sub>g</sub>	A <sub>1g</sub> +A <sub>2g</sub> +E <sub>g</sub>	T <sub>1g</sub> +T <sub>2g</sub>	T <sub>1g</sub> +T <sub>2g</sub>	E <sub>u</sub>	E <sub>u</sub>	A <sub>1u</sub> +A <sub>2u</sub> +E <sub>u</sub>	T <sub>1u</sub> +T <sub>2u</sub>	T <sub>1u</sub> +T <sub>2u</sub>
T <sub>1g</sub>	T <sub>1g</sub>	T <sub>2g</sub>	T <sub>1g</sub> +T <sub>2g</sub>	A <sub>1g</sub> +E <sub>g</sub> +T <sub>1g</sub> +T <sub>2g</sub>	A <sub>2g</sub> +E <sub>g</sub> +T <sub>1g</sub> +T <sub>2g</sub>	T <sub>1u</sub>	T <sub>2u</sub>	T <sub>1u</sub> +T <sub>2u</sub>	A <sub>1u</sub> +E <sub>u</sub> +T <sub>1u</sub> +T <sub>2u</sub>	A <sub>2u</sub> +E <sub>u</sub> +T <sub>1u</sub> +T <sub>2u</sub>
T <sub>2g</sub>	T <sub>2g</sub>	T <sub>1g</sub>	T <sub>1g</sub> +T <sub>2g</sub>	A <sub>2g</sub> +E <sub>g</sub> +T <sub>1g</sub> +T <sub>2g</sub>	A <sub>1g</sub> +E <sub>g</sub> +T <sub>1g</sub> +T <sub>2g</sub>	T <sub>2u</sub>	T <sub>1u</sub>	T <sub>1u</sub> +T <sub>2u</sub>	A <sub>2u</sub> +E <sub>u</sub> +T <sub>1u</sub> +T <sub>2u</sub>	A <sub>1u</sub> +E <sub>u</sub> +T <sub>1u</sub> +T <sub>2u</sub>
A <sub>1u</sub>	A <sub>1u</sub>	A <sub>2u</sub>	E <sub>u</sub>	T <sub>1u</sub>	T <sub>2u</sub>	A <sub>1g</sub>	A <sub>2g</sub>	E <sub>g</sub>	T <sub>1g</sub>	T <sub>2g</sub>
A <sub>2u</sub>	A <sub>2u</sub>	A <sub>1u</sub>	E <sub>u</sub>	T <sub>2u</sub>	T <sub>1u</sub>	A <sub>2g</sub>	A <sub>1g</sub>	E <sub>g</sub>	T <sub>2g</sub>	T <sub>1g</sub>
E <sub>u</sub>	E <sub>u</sub>	E <sub>u</sub>	A <sub>1u</sub> +A <sub>2u</sub> +E <sub>u</sub>	T <sub>1u</sub> +T <sub>2u</sub>	T <sub>1u</sub> +T <sub>2u</sub>	E <sub>g</sub>	E <sub>g</sub>	A <sub>1g</sub> +A <sub>2g</sub> +E <sub>g</sub>	T <sub>1g</sub> +T <sub>2g</sub>	T <sub>1g</sub> +T <sub>2g</sub>
T <sub>1u</sub>	T <sub>1u</sub>	T <sub>2u</sub>	T <sub>1u</sub> +T <sub>2u</sub>	A <sub>1u</sub> +E <sub>u</sub> +T <sub>1u</sub> +T <sub>2u</sub>	A <sub>2u</sub> +E <sub>u</sub> +T <sub>1u</sub> +T <sub>2u</sub>	T <sub>1g</sub>	T <sub>2g</sub>	T <sub>1g</sub> +T <sub>2g</sub>	A <sub>1g</sub> +E <sub>g</sub> +T <sub>1g</sub> +T <sub>2g</sub>	A <sub>2g</sub> +E <sub>g</sub> +T <sub>1g</sub> +T <sub>2g</sub>
T <sub>2u</sub>	T <sub>2u</sub>	T <sub>1u</sub>	T <sub>1u</sub> +T <sub>2u</sub>	A <sub>2u</sub> +E <sub>u</sub> +T <sub>1u</sub> +T <sub>2u</sub>	A <sub>1u</sub> +E <sub>u</sub> +T <sub>1u</sub> +T <sub>2u</sub>	T <sub>2g</sub>	T <sub>1g</sub>	T <sub>1g</sub> +T <sub>2g</sub>	A <sub>2g</sub> +E <sub>g</sub> +T <sub>1g</sub> +T <sub>2g</sub>	A <sub>1g</sub> +E <sub>g</sub> +T <sub>1g</sub> +T <sub>2g</sub>

**Table 4.2:** Product table of the  $O_h$  point group [60].

## Chapter 4. Ultrafast generation of hidden phases via energy-tuned electronic photoexcitation in magnetite

This means that the product between the symmetry representation of  $\varepsilon_{xy}$ , which is  $T_{2g}$ , and  $\Delta$  must as well belong to the  $A_{1g}$  representation. As seen in Table 4.2, the only possible representation multiplied by  $T_{2g}$  that gives  $A_{1g}$  is  $T_{2g}$  itself. Therefore the order parameter  $\Delta$  must belong to the  $T_{2g}$  representation and can be expressed with its three components,  $\Delta = (\Delta_{xy}, \Delta_{yz}, \Delta_{xz})$ . The free energy will be rewritten as:

$$F_{\text{coupling}} = \underbrace{g_1 \varepsilon_{xy} \Delta_{xy}}_{\alpha_1} + \underbrace{g_2 \varepsilon_{yz} \Delta_{yz}}_{\alpha_2} + \underbrace{g_3 \varepsilon_{xz} \Delta_{xz}}_{\alpha_3} \quad (4.2)$$

which leads to three possible scenarios, represented in Figure 4.8:

- $\alpha_1, \alpha_2, \alpha_3 \neq 0$ , all the angles are different from  $90^\circ$  and the system is trigonal, Figure 4.8a;
- $\alpha_1, \alpha_2 \neq 0$  and  $\alpha_3 = 0$ , the system is triclinic with  $a \neq b \neq c$ , Figure 4.8b;
- $\alpha_1 \neq 0$  and  $\alpha_2, \alpha_3 = 0$ , the system is monoclinic, Figure 4.8c, so  $a$  and  $b$  are unchanged and only  $c$  suffers a modification and only one angle is different from  $90^\circ$ .

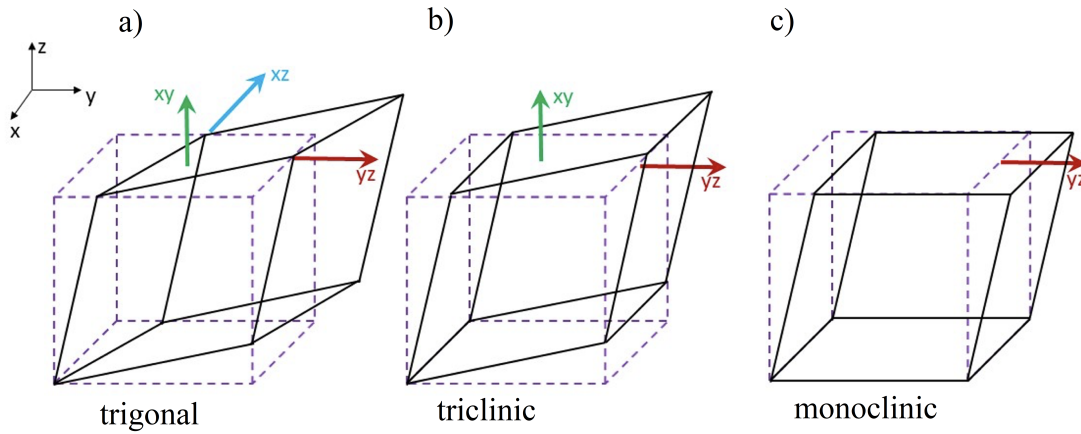


**Figure 4.8:** Possible strain configurations from the initial cubic lattice: a) trigonal, b) triclinic, and c) monoclinic.

Since the strain in the  $[110]$  direction originates from the formation of the trimeron network, the latter can be considered a valid order parameter as it fulfills the symmetry criterion.

### 4.3 Verwey transition under out-of-equilibrium conditions

The possibility to prompt the metal-to-insulator transition by ultrashort light pulses has opened new opportunities to understand the dynamics of such mechanisms and the possibility to explore hidden phases otherwise unachievable. A phase consisting of cubic domains surrounded by the rest of the monoclinic structure has been discovered in an ultrafast resonant x-ray diffraction experiment utilizing ultrashort 800 nm laser pulses as excitation [61]. Such a process happens in two steps, destruction of the trimerons and recovery to the cubic phase, with characteristic times of 300 fs and 1.5 ps. Another study about optical reflectivity showed the existence of three excitation regimes and suggests that the 800 nm pulses used as excitation act as heating similarly to the equilibrium thermodynamic of magnetite [57]. To date, all the previous studies, including simulations, considered only the 800 nm excitation wavelength, which corresponds to 1.55 eV and will excite the  $d-d$   $\text{Fe}_B^{2+} t_{2g} \rightarrow \text{Fe}_B^{3+} t_{2g}$  optical transition [62]. In this work, we study the evolution of the (660) Bragg peak under 800 nm and 400 nm photoexcitation with pulse duration of 45 fs and fluences of  $2.9 \text{ mJ}/\text{cm}^2$  (intermediate regime [57]) and  $1.2 \text{ mJ}/\text{cm}^2$  respectively. The sample is maintained at a temperature of 80 K. The results are shown in Figure 4.9.

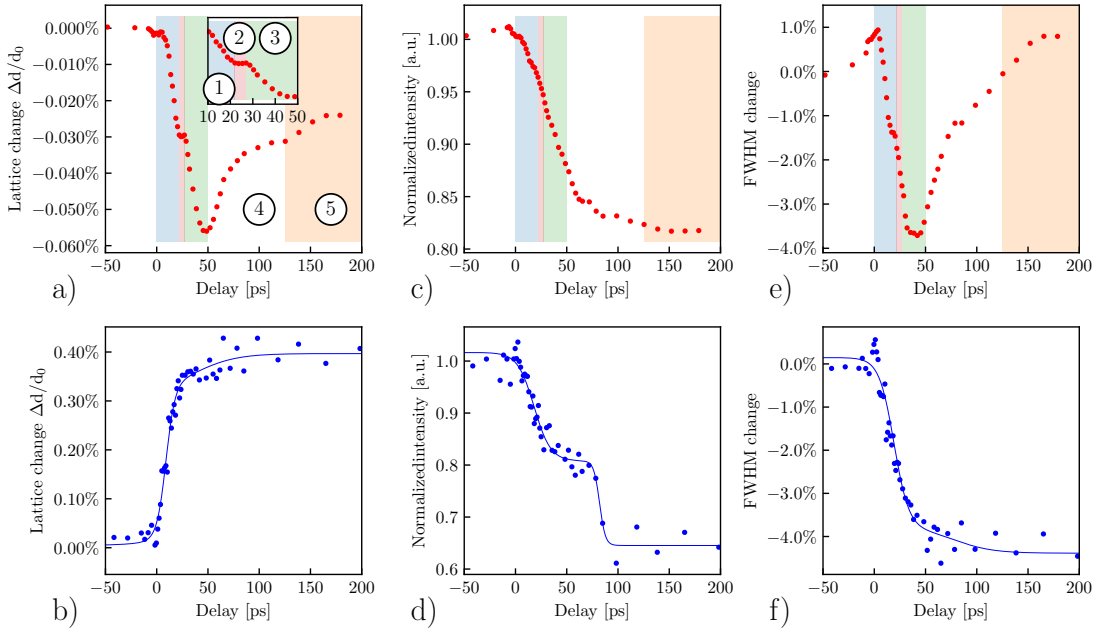


**Figure 4.9:** Evolution of the lattice compression/expansion (a-b), normalized intensity (c-d), and FWHM (e-f) along the [110] direction under 800 nm (red traces) and 400 nm (blue traces) photoexcitation. In (a), the shaded areas show multiple compression stages. Solid lines are guides to the eye.

## Chapter 4. Ultrafast generation of hidden phases via energy-tuned electronic photoexcitation in magnetite

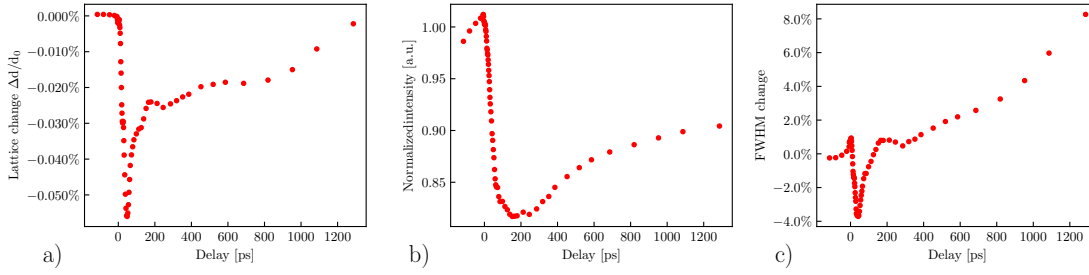


**Figure 4.10:** Evolution of the lattice compression/expansion (a), normalized intensity (b), and FWHM (c) along the [110] direction under 800 nm photoexcitation until 1.3 ns.

We discuss first the case of 800 nm photoexcitation.

The observation of the lattice dynamics shows a compression of approximately  $-0.06\%$ , which reveals a change toward the cubic phase. Our data expands the range of previous works [54, 57, 61] and demonstrates that the hidden phase lasts for about 50 ps and is divided into three compression stages, marked by the shaded areas in Figure 4.9a: the first one shows a sudden compression of about  $-0.03\%$  and lasts 22 ps; in the second one a minor compression is visible and lasts approximately 5 ps; the third one adds a further compression of  $0.03\%$  in the last 23 ps. The presence of several steps is a distinctive trait of separate processes such as electron-phonon coupling and phonon-phonon interaction [54, 63] but with our time resolution of several ps is not able to distinguish electron-electron interaction contributions since it is supposed to have a timescale of  $<300$  fs [61]. A multi-stage behavior is observed as well in the relaxation process, with an expansion between 50 ps and 126 ps of about  $0.03\%$ , which is the same amount as the compression in the third compression stage. Finally, the last and fifth step in the evolution of the lattice is a further expansion towards the equilibrium phase which is still not recovered after 1.3 ns, as shown in Figure 4.10a.

Concerning the intensity of the Bragg peak, Figure 4.9c, a drop is visible after the photoexcitation. The recovery towards the HT cubic phase is expected to increase the intensity of the peak, but such behavior is not observed, even after 1.3 ns. This could be explained by the fact that the photoexcitation increases the temperature of the lattice with a consequent structural disorder due to the motion of the atoms, a phenomenon called induced Debye-Waller effect [44]. A similar long-lived state is visible also in the FWHM which drops, recovers after 200 ps, and keeps broadening after 1.3 ps. Such long dynamics are a sign that the phase induced by the 800 nm photoexcitation is metastable and the relaxation process involves a complex pathway with the interplay of electron-electron, electron-phonon, and phonon-phonon interactions. The lifetime marks as well the existence of a hidden phase in the out-of-equilibrium

### 4.3 Verwey transition under out-of-equilibrium conditions

---

regime, therefore the observed phase separation between cubic islands and monoclinic background is rather a local minimum in energy than an equilibrium state. The formation of the cubic islands is consequent to the destruction of the long-range order in the trimeron network due to the optically triggered  $d-d$  excitations. In fact, the excited minority  $t_{2g}$  electrons see their mobility restored and change the valency of the  $\text{Fe}^{2+}$  and  $\text{Fe}^{3+}$  obtaining the destruction of the trimeron in a timescale  $<300$  fs. Therefore, the  $\text{Fe}_B\text{-Fe}_B$  bond is restored to its original length removing the strain, the long-range order of the trimers is destroyed and the structure is allowed to return to the cubic high-temperature phase. The data shows that the relaxation process back towards the monoclinic state is a two-step process via the interaction of the electrons with high-energy optical phonons first which in turn decay anharmonically into acoustic modes through a three-phonon scattering process [64–67]. A possible scenario explaining the multiple compression stages is as follows: during the first compression stage the conduction electrons in the trimeron couple with the  $X_3$  phonon mode (TO) [56] while during the second one, the  $X_3$  (TO) phonons couple with the  $\Delta_5$  mode and the residual local stress on the structure is distributed through percolation. Such a scenario is supported by another UED experiment showing that, under the same excitation, the  $X_3$  (TO) mode is prompted through the electron-phonon coupling [54] while the  $\Delta_5$  modes are deemed the most susceptible to the lattice transformation [53].

We repeated the same experiment under 400 nm excitation, which corresponds to 3.10 eV, and it is shown in the second row of Figure 4.9. In this case, the lattice expands about 0.4 % which is an opposite behavior compared to what was observed in the 800 nm case and implies that the monoclinic distortion is reinforced by this photoexcitation. Since only one Bragg peak is visible in this LT phase, it is not possible to measure accurately the value of the monoclinic angle  $\beta_M$ , whose nominal value before the photoexcitation is  $90.236^\circ$  [52], but, upon the excitation, it is expected to increase. Such modification of the lattice occurs in a phase that is not showing any thermal-induced modification, therefore it is only optically accessible and it is another hidden phase with an increased monoclinic angle. While the one induced by the 800 nm excitation is a mixed phase with the coexistence of cubic and monoclinic domains, this one is fully monoclinic and its manifestation is evident after approximately 50 ps in a single stage and it is attributed mainly to electron-phonon coupling. The phase remains stable and there is no sign of recovery for a duration up to 200 ps, which marks again a metastable state. Concerning the intensity and the FWHM, a drop in the former is observed consistently with what is expected for the structure factor, while the latter shows a shrinking instead of the broadening expected by a thermal effect. This reinforces the conclusion that it is indeed an only-optical accessible state with an increased long-range structural order. X-rays measurements show that a maximum of

## Chapter 4. Ultrafast generation of hidden phases via energy-tuned electronic photoexcitation in magnetite

three trimers are allowed for a  $\text{Fe}_B^{3+}$  site but only four of the eight sites participate in the trimeron formation while the others remain inactive [52], and our data shows that below 90 K the monoclinic distortion remains stable until 40 K, so no further trimerons are created. From the optical reflectivity data, it is visible that the 400 nm excitation is responsible for a ligand-to-metal charge transfer from the 2p oxygen bands to the 3d bands of  $\text{Fe}_B$ . This results in a change of the valence of the inactive  $\text{Fe}_B$  from  $\text{Fe}^{3+}$  to  $\text{Fe}^{2+}$ , increasing the  $t_{2g}$  orbital ordering and creating new trimerons. As a consequence, the monoclinic distortion is reinforced in a region where it is not thermally accessible and the trimeron lattice is further populated. One effect at play is represented by the Jahn-Teller distortion induced by the orbital ordering and another is caused by the localization of the charge in the newly formed trimerons, which creates additional stress on the structure reducing the  $\text{Fe}_B\text{-Fe}_B$  bond length. Another x-ray experiment showed that doping the magnetite would introduce selective  $\text{Fe}^{2+}$  sites vacancies replacing them with  $\text{Fe}^{3+}$  which in their case weakens the trimeron network [68]. In our case the opposite effect is observed, the  $\text{Fe}^{3+}$  become  $\text{Fe}^{2+}$  due to the ligand-metal charge transfer, and the trimeron network is reinforced leading to an increased expansion of the lattice in the [110] direction.

The Figure 4.11 summarizes the evolution of the trimeron lattice based on the different photoexcitations.

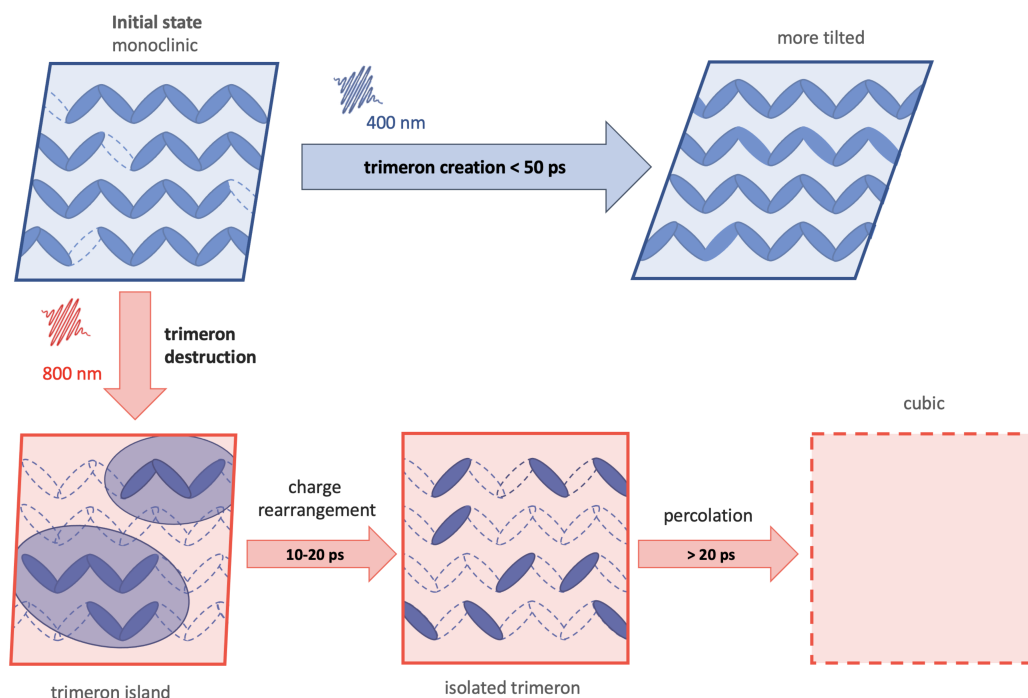


**Figure 4.11:** Sketch summarizing the evolution of the trimeron lattice based on the different photoexcitations.



### Limitations and open questions

According to the simulations more reflections are expected, even with a much lower intensity, but they are not observed in LT phase. This could be explained by the presence of micro-sized domains (twins) and the increasing strain on the structure combined with the physical size of the probe (electron beam). Since the latter is around  $500\ \mu\text{m}$  at the sample position, and it is a convergent beam, the intensity of the expected peaks is not seen both because the domains and the strain reduce the overall coherence of the surface along the beam footprint and also because the area probed could include several domains, therefore the total intensity of those reflections would be a superposition of peaks of different domains and hidden in the signal noise. Also, since during the phase separation the coherence length of the trimeron lattice shrinks to hundreds of nanometers [69], the size and footprint of our beam probe an average of several phases, reducing the ability to distinguish the specific mechanism at the origin of the observed multi-stage compression. In this regard, techniques that make use of nano-sized electron beams such as CB-UEM [70] could help to better understand the origin of the observed phenomena.

Furthermore, our work is based on the observation of the distortion of the lattice in the [110] direction with only one visible peak, which limits our ability to detect distortions in the other two directions. The investigation of different Bragg peaks and different zone axes would provide additional information on the direction of the strain.

## 4.4 Conclusions

In this work, we observed the evolution of the diffraction pattern of magnetite along the [110] direction in the temperature range 40 K-300 K, detecting changes to the diffraction peak at the Verwey transition. Exploiting the framework of the Ginzburg-Landau theory we were able to identify the symmetry of the proposed order parameter, which is the trimeron arrangement along the probed crystallographic direction. We exploit two different excitation energies, 1.55 eV and 3.10 eV to drive the magnetite from its equilibrium state at 80 K to two distinct metastable states inaccessible by thermal excitation. The first one, triggered by the 800 nm photoexcitation, is a hidden mixed phase with the coexistence of cubic and monoclinic domains, while the second one, triggered by the 400nm photoexcitation, leads to a ligand-to-metal charge transfer and the formation of new trimerons, which reinforce the monoclinic distortion. We expose the key role of the trimeron network in inducing the structural transition and demonstrate the ability to establish different hidden phases through selective electronic excitations.



# A Software

## A.1 Acquisition software

The software is written in Python and it is based on the PyQt5 library for the graphical interface and the pyqtgraph library for the display of the data. The use of Python language allows the software to be easily customized and adapted depending on the kind of experiment to be performed and the preferences of the users.

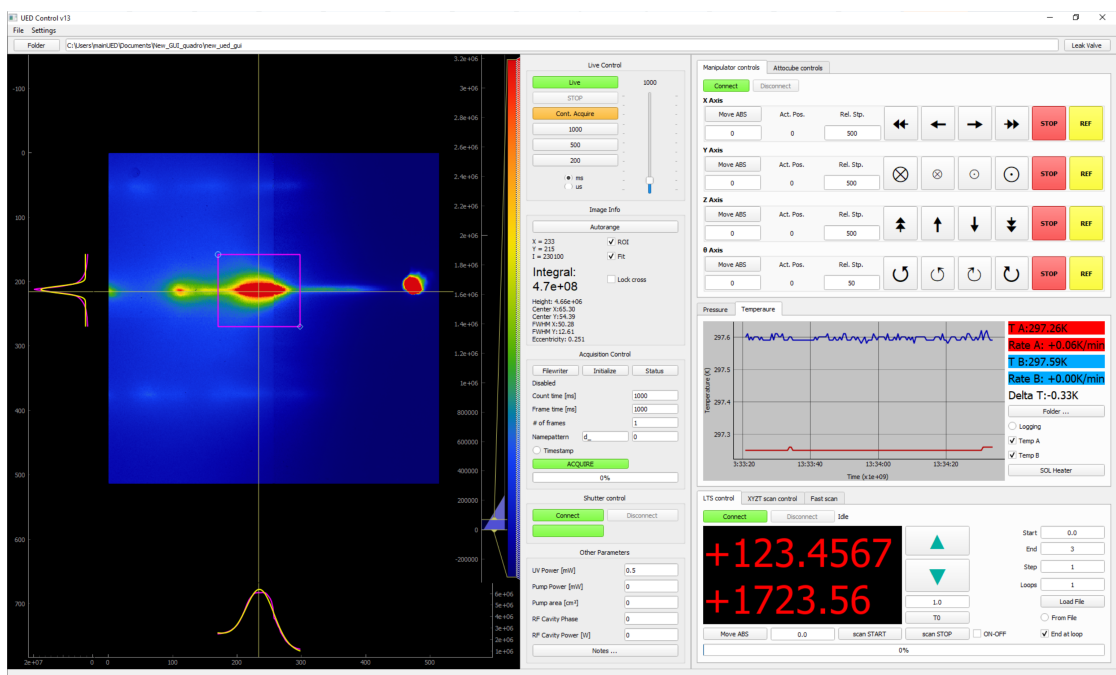


**Figure A.1:** Screenshot of the UED software. The main window is divided in three parts: the left part displays the acquired image and eventual cross sections, the middle part mostly controls the acquisition settings for the detector and some basic image information, the right part controls the movement of the sample, monitors temperature and pressure and controls delay scans and rocking curves.

## Appendix A. Software

---

Figure A.1 shows the main window of the acquisition software which can acquire in two modes: live and full. In live mode the detector only acquires one frame with the specified exposure time and it requires less time to be initialized; in full mode the detector allows for more parameters to be tuned, more details below, but requires more time and it is less suitable for continuous acquisition. The interface is divided into three main areas:

- the left panel displays the last acquired image in a colormap together with its cross sections at the cursor position (or horizontal/vertical binning in case of a ROI). A colorbar allows adjustment of the displayed range of data.
- the middle panel houses different subpanels:
  - the first subpanel allows to control the live acquisition settings (display or save, exposure time) and to start and stop the acquisition. In live mode the image can be acquired at a maximum frame rate of 15fps (if only displayed) or 4fps if it is also saved to disk. Details on the file format will be discussed later;
  - the second subpanel displays information about the counts in the selected pixel and the total counts in the selected ROI as well as the possibility to disable the ROI, enable a fit of the two binnings (which will be displayed together with the cross sections) and the fit parameters;
  - the third subpanel controls the acquisition parameters for the full acquisition mode. These include the exposure time and the number of frames per single exposure, allowing to take frames up to the maximum frequency, which is one of the main advantages of this detector. This mode does not allow to view the frames during the acquisition but only after the acquisition is finished;
  - the fourth subpanel controls a shutter which will enable/disable the pump beam;
  - the last panel allows to store information about other acquisition parameters such as UV and pump power, area, cavity parameters and general notes;
- the third panel hosts the movement controls for all 5 axes, pressure and temperature monitoring and logging, delay scan and rocking curve controls.

In addition to the main window, two more windows (in Figure A.2) allow to control the temperature of the sample and the leak valve:

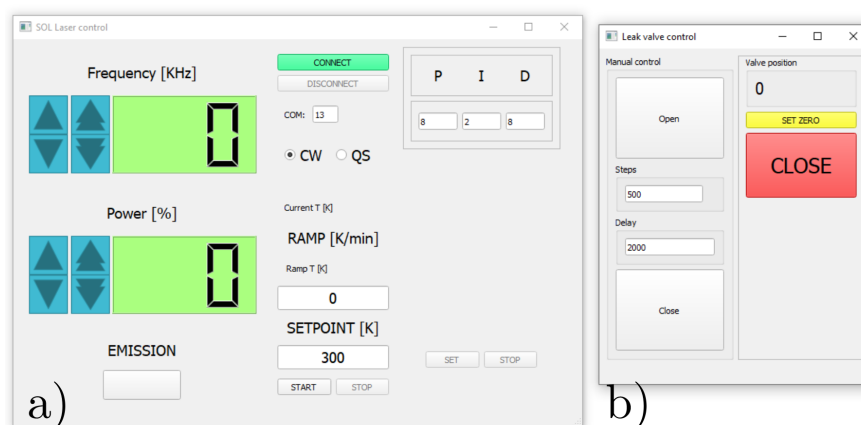


**Figure A.2:** Heating laser control with PID, setpoint and ramp controls and leak valve control.

- Figure A.2a shows the controls for the green laser used as a heater. The settings include power and repetition rate (which are not fully decoupled, the repetition rate will affect the maximum power available) as well as a PID panel to set the parameters. A setpoint can be chosen as well as a temperature ramp. The PID allows to maintain the setpoint to a fluctuation below 5mK. The emission can be turned on and off with the button on the bottom left;
- Figure A.2b shows the controls for the leak valve. Since it is operated by a stepper motor the interface allows to set the amount of steps the motor has to move and the delay between each step in  $\mu\text{s}$ . Once the valve is closed the counter on the top right shows 0 and the red CLOSE button allows to close the valve fully regardless of its current status. This function is used to quickly close the valve after an experiment or in case of emergency. A PID to control the valve based on the current pressure is under development.

**File format** The file format of choice is the HDF5 (.h5). Among its advantages, the important one to us is the possibility to store different kind of data, like numbers, strings, 1-2-3dimensional arrays, which fits well with the needs of this experiment. The data collected is composed by:

- the image itself as a 2D array of integers (or 3D array in case of multiple frames);
- the time of the acquisition in two format: a Windows timestamp which represents the number of 100-nanosecond intervals since January 1st, 1601 UTC and its conversion in a human readable format;
- the temperature of the sample and the cold finger of the cryostat, and the raw

## Appendix A. Software

---

value of the sensors in Ohm (these values can be single numbers or arrays in case of multiple frames);

- the pressure inside the chaeber in mbar (single number or array);
- positions of the manipulator (useful for rocking curves);
- position of the delay stage in mm;
- detector parameters (exposure time, number of frames, threshold energy);
- other parameters and notes;

### A.2 Data analysis software

The data analysis software is as well written in Python and based on the PyQt5 library for the graphical interface and the pyqtgraph library for the display of the data. The software supports several formats as input: .tiff, .h5, .SPE, and .pickle, both in single folders and in .zip archives. The entire datasets can be exported as .pickle files or just the images as .npy files.

The capabilities of the software are briefly discussed below, but a full manual is still under development and will be released with the final version of the software.

The main window is shown in Figure A.3. It is divided in three main areas: on the left side there are the controls for the displayed image, for the ROIs, for the fit and the output of the measurement ruler; the middle part is dedicated to display the acquired images and the profiles of the ROI, with a scrollbar to navigate the dataset; on the right part a tab selector allows to view multiple information such as the metadata of the acquisitions, Figure A.3, the temperature and pressure plots and the live fit parameters Figure A.4.

The image controls allow to:

- change the image to grayscale or colormap;
- copy the image to the clipboard;
- sum all frames or a selected range;
- rotate by an arbitrary angle:

The ROI controls allow to:

- enable the ROI;
- autoscale the image based on the ROI content;
- add or remove multiple ROIs;

All ROIs are movable, resizable and rotatable.

The fit controls allow to:

- enable the fit;
- select the fit function between Gaussian and Voigt;
- fit all data and all ROIs;

The ruler panel shows the output of the measuring tools which can be pixels, mm or  $\text{\AA}^{-1}$ , together with the orientation of the ruler in degrees.

In the image panel the ROIs are visible as magenta boxes with handles for their manipulation. If the fit is enabled a crosshair will show the center of the fit and an ellipse will show the contour of the fit at the FWHM. The imaged can be moved and enlarged at will. The two profile plots show the horizontal and vertical binnings of the ROI and the fit, if enabled.

The top menus grant access to additional analysis tools: a radial average tool Figure A.5 which allows to define a circular sector around a peak and average the counts as a function of the distance from the peak, a calibration tool Figure A.6 which allows to retrieve the calibration constant from a known pattern or apply a previously calculated one, a plotter tool Figure A.7 which allows to plot the result of a fit and holds also previous datasets for comparison, and a simulator tool Figure A.9 which allows to simulate a diffraction pattern from any crystal structure or atom distribution. The pump-probe menu allows to perform basic analysis of pump-probe experiments such as the grouping of the frames by delay, the selection of the loops, and the calculation of  $t_0$  and the time resolution.

## Appendix A. Software

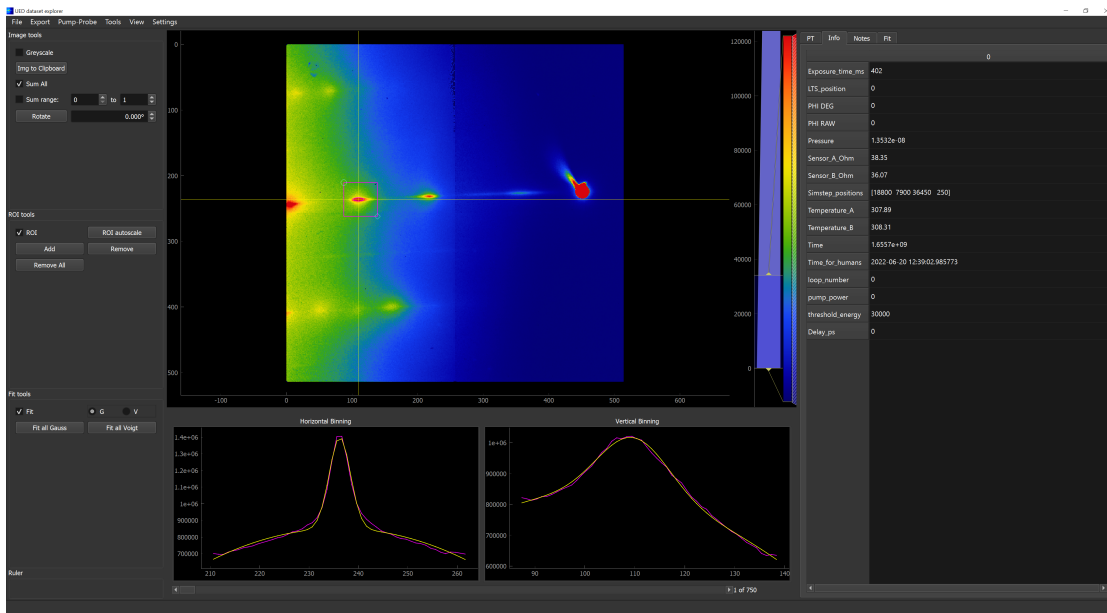


Figure A.3: Screenshot of the UED data analysis software in the main window.



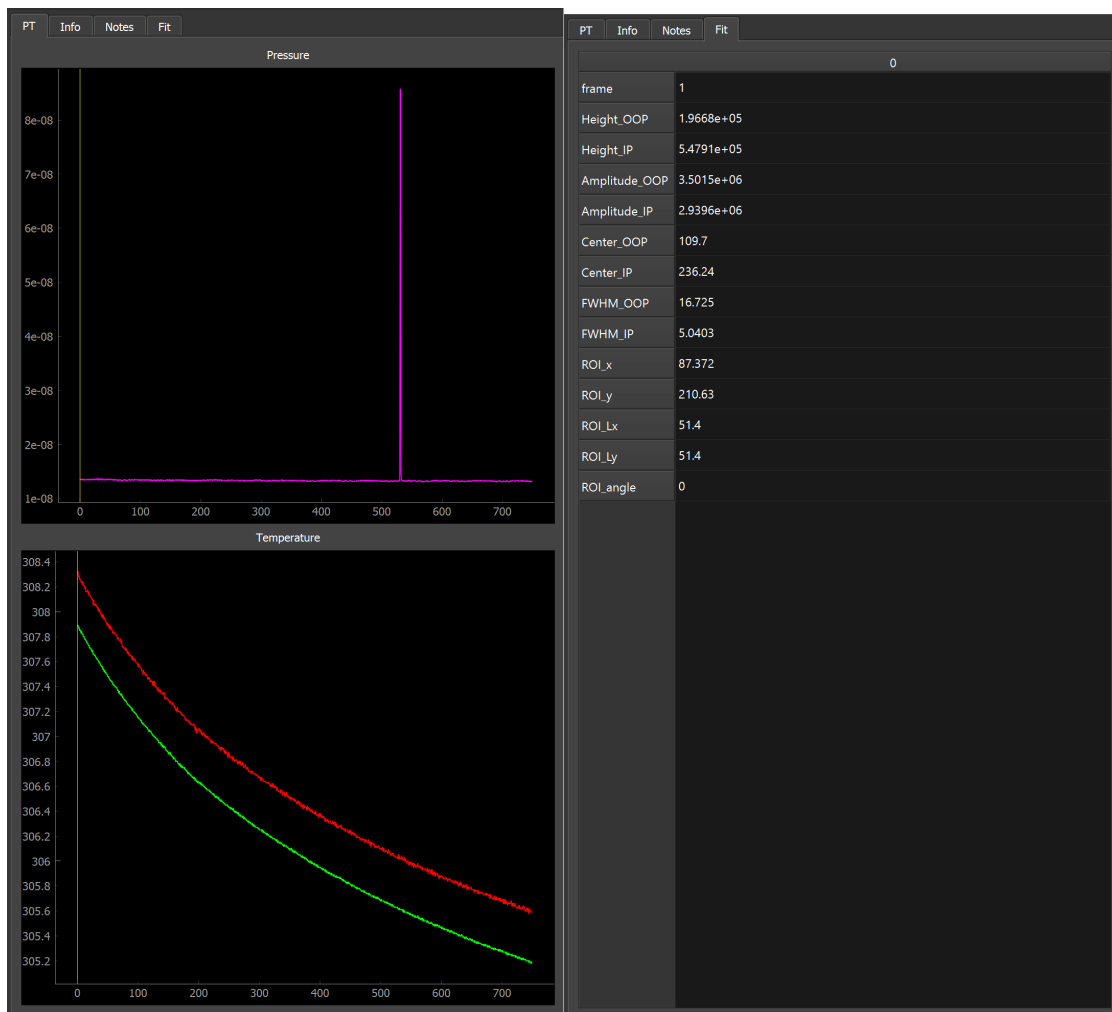


Figure A.4: Screenshot of the UED data analysis software showing the hidden tabs.

## Appendix A. Software

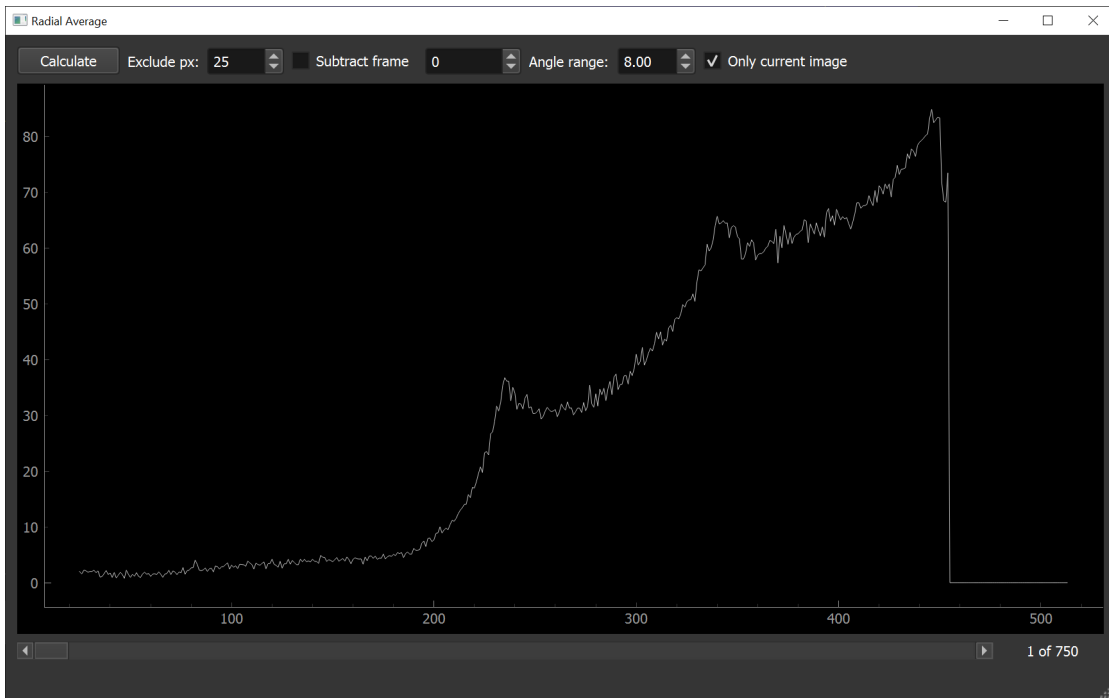


Figure A.5: Screenshot of the radial average tool.

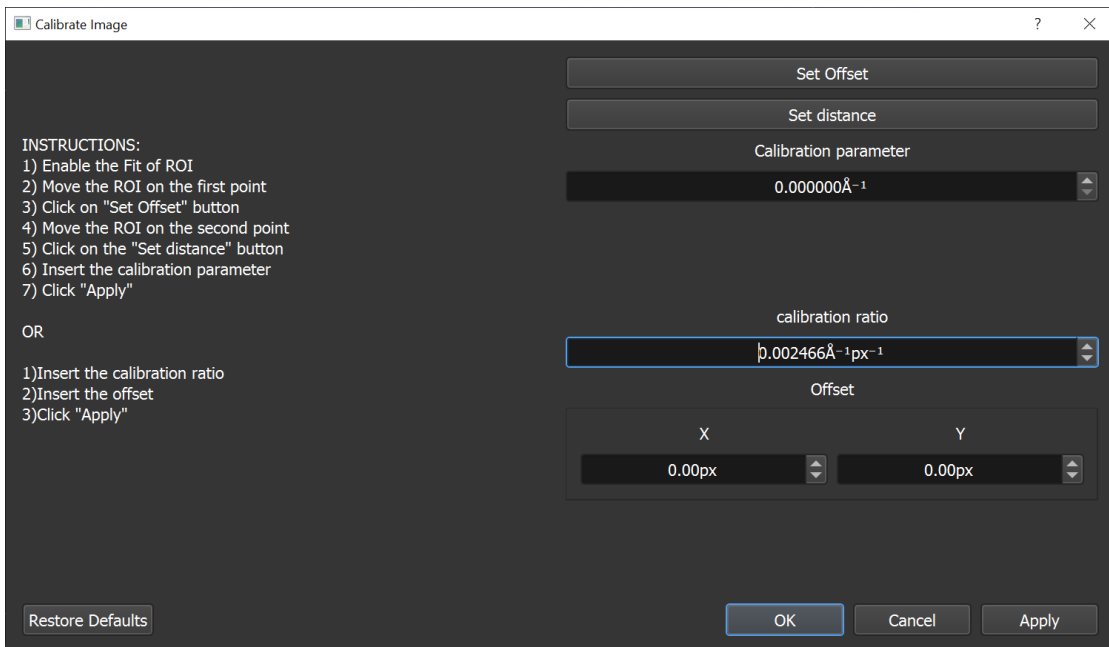


Figure A.6: Screenshot of the calibration tool.

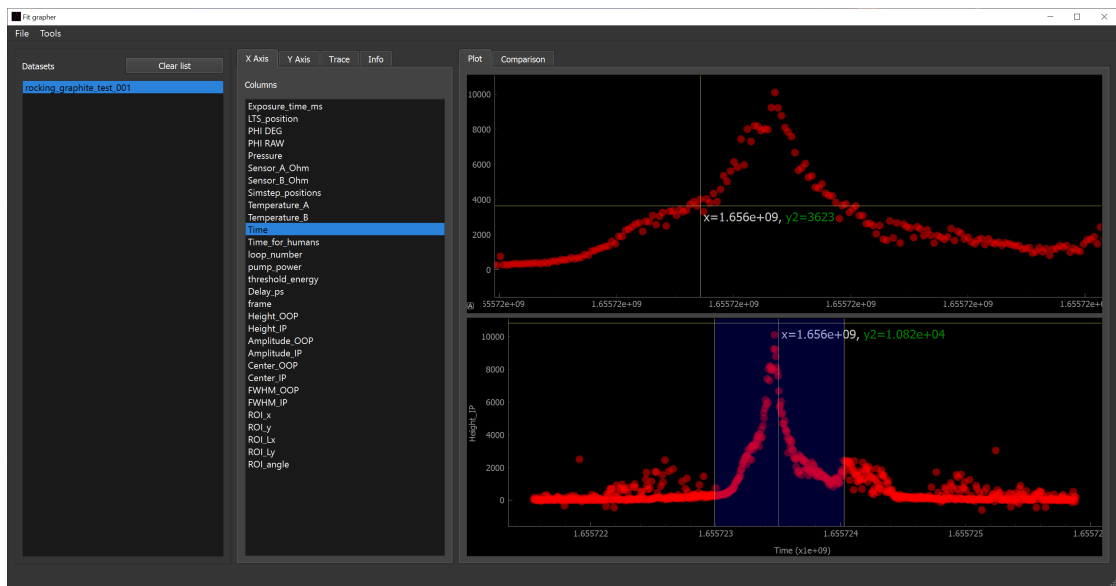


Figure A.7: Screenshot of the plotting tool.

## Appendix A. Software

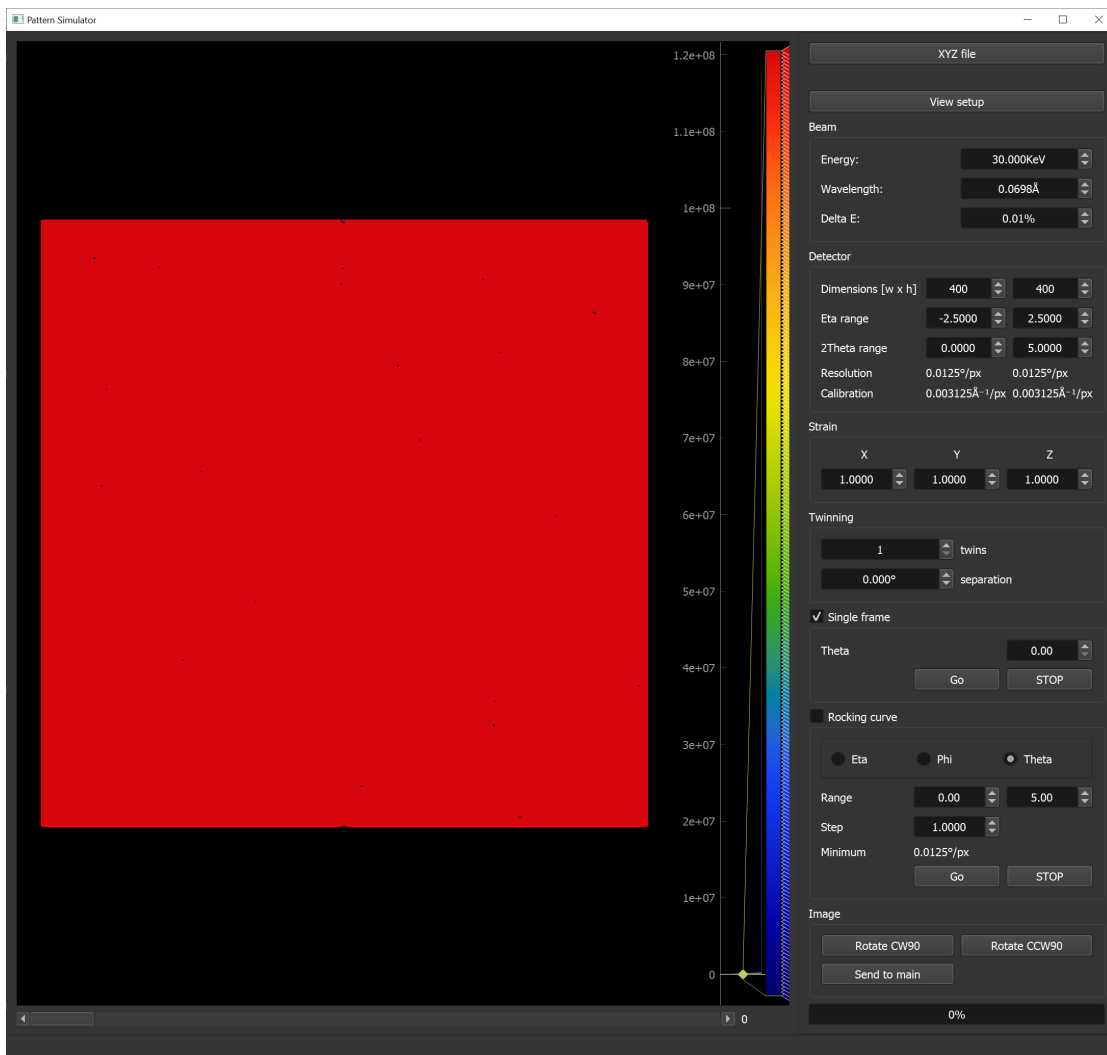


Figure A.8: Screenshot of the plotting tool.

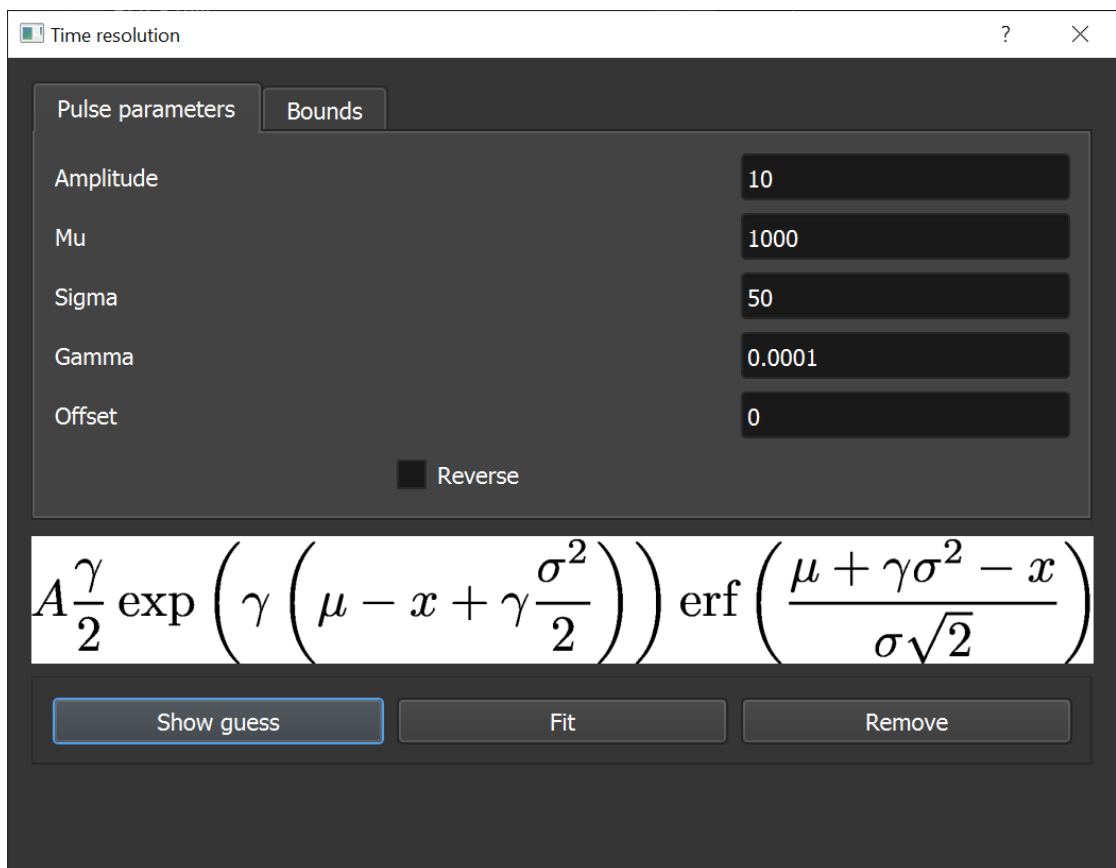


Figure A.9: Screenshot of the time resolution tool.



## Bibliography

- [1] William Henry Bragg and William Lawrence Bragg. The reflection of x-rays by crystals. *Proceedings of the Royal Society of London. Series A, Containing Papers of a Mathematical and Physical Character*, 88(605):428–438, 1913.
- [2] Neil W Ashcroft, N David Mermin, et al. *Solid state physics*, 1976.
- [3] M Pl Seah and WA Dench. Quantitative electron spectroscopy of surfaces: A standard data base for electron inelastic mean free paths in solids. *Surface and interface analysis*, 1(1):2–11, 1979.
- [4] JH Neave, BA Joyce, PJ Dobson, and N Norton. Dynamics of film growth of gaas by mbe from rheed observations. *Applied Physics A*, 31(1):1–8, 1983.
- [5] Gertjan Koster, Mark Huijben, A Janssen, and G Rijnders. Growth studies of heteroepitaxial oxide thin films using reflection high-energy electron diffraction (rheed). In *Epitaxial Growth of Complex Metal Oxides*, pages 3–29. Elsevier, 2015.
- [6] Masatomo Sumiya, Noritaka Ogusu, Kouhei Osada, and Shunro Fuke. In-situ rheed observation of mocvd-gan film growth. *MRS Online Proceedings Library (OPL)*, 693, 2001.
- [7] Shuji Hasegawa. Reflection high-energy electron diffraction. *Characterization of Materials*, 97:1925–1938, 2012.
- [8] Nevill Francis Mott. The scattering of electrons by atoms. *Proceedings of the Royal Society of London. Series A, Containing Papers of a Mathematical and Physical Character*, 127(806):658–665, 1930.
- [9] Hans Bethe. Zur theorie des durchgangs schneller korpuskularstrahlen durch materie. *Annalen der Physik*, 397(3):325–400, 1930.
- [10] Ahmed H Zewail. Femtochemistry: Atomic-scale dynamics of the chemical bond. *The Journal of Physical Chemistry A*, 104(24):5660–5694, 2000.

## Bibliography

---

- [11] Majed Chergui and Ahmed H Zewail. Electron and x-ray methods of ultrafast structural dynamics: Advances and applications. *ChemPhysChem*, 10(1):28–43, 2009.
- [12] Majed Chergui and Eric Collet. Photoinduced structural dynamics of molecular systems mapped by time-resolved x-ray methods. *Chemical reviews*, 117(16): 11025–11065, 2017.
- [13] Ahmed H Zewail. 4d ultrafast electron diffraction, crystallography, and microscopy. *Annual review of physical chemistry*, 57:65–103, 2006.
- [14] Ding-Shyue Yang, Nuh Gedik, and Ahmed H Zewail. Ultrafast electron crystallography. 1. nonequilibrium dynamics of nanometer-scale structures. *The Journal of Physical Chemistry C*, 111(13):4889–4919, 2007.
- [15] Giulia Fulvia Mancini, Barbara Mansart, Saverio Pagano, Bas Van Der Geer, Marieke De Loos, and Fabrizio Carbone. Design and implementation of a flexible beamline for fs electron diffraction experiments. *Nuclear Instruments and Methods in Physics Research Section A: Accelerators, Spectrometers, Detectors and Associated Equipment*, 691:113–122, 2012.
- [16] Francesco Pennacchio, Giovanni M Vanacore, Giulia F Mancini, Malte Oppermann, Rajeswari Jayaraman, Pietro Musumeci, Peter Baum, and Fabrizio Carbone. Design and implementation of an optimal laser pulse front tilting scheme for ultrafast electron diffraction in reflection geometry with high temporal resolution. *Structural Dynamics*, 4(4):044032, 2017.
- [17] R. Peierls. Quelques propriétés typiques des corps solides. *Annales de l'I.H.P.*, 5(3):177–222, 1935. ISSN 0365-320X.
- [18] N. D. Mermin and H. Wagner. Absence of ferromagnetism or antiferromagnetism in one- or two-dimensional isotropic Heisenberg models. *Physical Review Letters*, 17(22):1133–1136, 1966. ISSN 00319007. doi: 10.1103/PhysRevLett.17.1133.
- [19] J. M. Kosterlitz and D. J. Thouless. Ordering, metastability and phase transitions in two-dimensional systems. *Journal of Physics C: Solid State Physics*, 6(7):1181–1203, 1973. ISSN 00223719. doi: 10.1088/0022-3719/6/7/010.
- [20] J. M. Kosterlitz and D. J. Thouless. Two-Dimensional Physics. *Progress in Low Temperature Physics*, 7:371–433, 1978. ISSN 00796417. URL <https://linkinghub.elsevier.com/retrieve/pii/S0079641708601754>.



- [21] B. I. Halperin and David R. Nelson. Theory of Two-Dimensional melting. *Physical Review Letters*, 41(2):121–124, 1978. ISSN 00319007. doi: 10.1103/PhysRevLett.41.121.
- [22] A. P. Young. Melting and the vector Coulomb gas in two dimensions. *Physical Review B*, 19(4):1855–1866, 1979. ISSN 01631829. doi: 10.1103/PhysRevB.19.1855.
- [23] Katherine J Strandburg. Two-dimensional melting.
- [24] Antara Pal, Md Arif Kamal, and VA Raghunathan. Observation of the chiral and achiral hexatic phases of self-assembled micellar polymers. *Scientific reports*, 6(1):32313, 2016.
- [25] IA Zaluzhnyy, RP Kurta, EA Sulyanova, OY Gorobtsov, AG Shabalin, AV Zozulya, AP Menushenkov, M Sprung, BI Ostrovskii, and IA Vartanyants. Spatially resolved x-ray studies of liquid crystals with strongly developed bond-orientational order. *Physical Review E*, 91(4):042506, 2015.
- [26] Peter Keim, Georg Maret, and Hans-Hennig von GRÜNBERG. Franks constant in the hexatic phase. *Physical Review E*, 75(3):031402, 2007.
- [27] Sidi M. Maiga and Silvina M. Gatica. Monolayer adsorption of noble gases on graphene. *Chemical Physics*, 501:46–52, 2018. ISSN 0301-0104. doi: <https://doi.org/10.1016/j.chemphys.2017.11.020>. URL <https://www.sciencedirect.com/science/article/pii/S0301010417306614>.
- [28] L.A Rowley, D Nicholson, and N.G Parsonage. Monte carlo grand canonical ensemble calculation in a gas-liquid transition region for 12-6 argon. *Journal of Computational Physics*, 17(4):401–414, 1975. ISSN 0021-9991. doi: [https://doi.org/10.1016/0021-9991\(75\)90042-X](https://doi.org/10.1016/0021-9991(75)90042-X). URL <https://www.sciencedirect.com/science/article/pii/002199917590042X>.
- [29] A. Ambrosetti and P. L. Silvestrelli. Adsorption of rare-gas atoms and water on graphite and graphene by van der waals-corrected density functional theory. *Journal of Physical Chemistry C*, 115(9):3695–3702, mar 2011. ISSN 19327447. doi: 10.1021/JP110669P/ASSET/IMAGES/JP110669P.SOCIAL.JPEG\_V03. URL <https://pubs.acs.org/doi/abs/10.1021/jp110669p>.
- [30] Christopher G. Shaw, S. C. Fain, and M. D. Chinn. Observation of orientational ordering of incommensurate argon monolayers on graphite. *Physical Review Letters*, 41(14):955–957, 1978. ISSN 00319007. doi: 10.1103/PhysRevLett.41.955.
- [31] Christopher G. Shaw and Samuel C. Fain. Condensation and compression of argon monolayers on graphite. Technical Report 1, 1979.

## Bibliography

---

- [32] Anthony D Novaco and John P McTague. Orientational epitaxy—the orientational ordering of incommensurate structures. *Physical Review Letters*, 38(22):1286, 1977.
- [33] George Jura and Dean Criddle. Phase transitions of argon adsorbed on graphite. *Journal of Physical and Colloid Chemistry*, 55(2):163–172, 1951. ISSN 00223654. doi: 10.1021/j150485a001. URL <https://pubs.acs.org/sharingguidelines>.
- [34] A. D. Crowell and D. M. Young. The adsorption of argon on graphite. *Transactions of the Faraday Society*, 49:1080–1085, 1953. ISSN 00147672. doi: 10.1039/tf9534901080.
- [35] A D Migone, Z R Li, and M. H.W. Chan. Melting transition of submonolayer Ar adsorbed on graphite. *Physical Review Letters*, 53(8):810–813, 1984. ISSN 00319007. doi: 10.1103/PhysRevLett.53.810.
- [36] JZ Larese and QM Zhang. Layer-by-layer melting of argon films on graphite: A neutron-diffraction study. *Physical review letters*, 64(8):922, 1990.
- [37] H Taub, K Carneiro, JK Kjems, L Passell, and JP McTague. Neutron scattering study of ar 36 monolayer films adsorbed on graphite. *Physical Review B*, 16(10):4551, 1977.
- [38] J. P. McTague, J. Als-Nielsen, J. Bohr, and M. Nielsen. Synchrotron x-ray study of melting in submonolayer Ar and other rare-gas films on graphite. *Physical Review B*, 25(12):7765–7772, 1982. ISSN 01631829. doi: 10.1103/PhysRevB.25.7765.
- [39] Jeffrey William Edington and JW Edington. *Electron diffraction in the electron microscope*. Springer, 1975.
- [40] Peter Trucano and Ruey Chen. Structure of graphite by neutron diffraction. *Nature*, 258(5531):136–137, 1975.
- [41] ZH Zhang, S Hasegawa, and S Ino. Rheed intensity oscillation during epitaxial growth of ag on si (111) surfaces at low temperature. *Physical Review B*, 55(15):9983, 1997.
- [42] B Joos and MS Duesbery. Dislocation energies in rare-gas monolayers on graphite. *Physical review letters*, 55(19):1997, 1985.
- [43] Cheyne M Scoby, RK Li, and P Musumeci. Effect of an ultrafast laser induced plasma on a relativistic electron beam to determine temporal overlap in pump–probe experiments. *Ultramicroscopy*, 127:14–18, 2013.

- 
- [44] Ahmed H Zewail and John Meurig Thomas. *4D electron microscopy: imaging in space and time*. World Scientific, 2009.
- [45] Fabrizio Carbone, Peter Baum, Petra Rudolf, and Ahmed H Zewail. Structural preablation dynamics of graphite observed by ultrafast electron crystallography. *Physical review letters*, 100(3):035501, 2008.
- [46] Robert P Chatelain, Vance R Morrison, Bart LM Klarenaar, and Bradley J Siwick. Coherent and incoherent electron-phonon coupling in graphite observed with radio-frequency compressed ultrafast electron diffraction. *Physical review letters*, 113(23):235502, 2014.
- [47] EJW Verwey. Electronic conduction of magnetite ( $\text{Fe}_3\text{O}_4$ ) and its transition point at low temperatures. *Nature*, 144(3642):327–328, 1939.
- [48] EJW Verwey and PW Haayman. Electronic conductivity and transition point of magnetite (“ $\text{Fe}_3\text{O}_4$ ”). *Physica*, 8(9):979–987, 1941.
- [49] WH Bragg. The structure of magnetite and the spinels. *Nature*, 95(2386):561–561, 1915.
- [50] Shih-Chang Weng, Yen-Ru Lee, Cheng-Gang Chen, Chia-Hung Chu, Yun-Liang Soo, and Shih-Lin Chang. Direct observation of charge ordering in magnetite using resonant multiwave x-ray diffraction. *Physical Review Letters*, 108(14):146404, 2012.
- [51] M Iizumi, TF Koetzle, G Shirane, S Chikazumi, M Matsui, and S Todo. Structure of magnetite ( $\text{Fe}_3\text{O}_4$ ) below the verwey transition temperature. *Acta Crystallographica Section B: Structural Crystallography and Crystal Chemistry*, 38(8):2121–2133, 1982.
- [52] Mark S Senn, Jon P Wright, and J Paul Attfield. Charge order and three-site distortions in the verwey structure of magnetite. *Nature*, 481(7380):173–176, 2012.
- [53] S Borroni, GS Tucker, F Pennacchio, J Rajeswari, U Stuhr, A Pisoni, J Lorenzana, HM Rønnow, and F Carbone. Mapping the lattice dynamical anomaly of the order parameters across the verwey transition in magnetite. *New Journal of Physics*, 19(10):103013, 2017.
- [54] Wei Wang, Jun Li, Zhixiu Liang, Lijun Wu, Pedro M Lozano, Alexander C Komarek, Xiaozhe Shen, Alex H Reid, Xijie Wang, Qiang Li, et al. Verwey transition as evolution from electronic nematicity to trimerons via electron-phonon coupling. *arXiv preprint arXiv:2202.08744*, 2022.

## Bibliography

---

- [55] Giuditta Perversi, Elise Pachoud, James Cumby, Jessica M Hudspeth, Jon P Wright, Simon AJ Kimber, and J Paul Attfield. Co-emergence of magnetic order and structural fluctuations in magnetite. *Nature communications*, 10(1):1–6, 2019.
- [56] Przemysław Piekarczyk, Dominik Legut, Edoardo Baldini, Carina A Belvin, Tomasz Kołodziej, Wojciech Tabiś, Andrzej Kozłowski, Zbigniew Kakol, Zbigniew Tarnawski, José Lorenzana, et al. Trimeron-phonon coupling in magnetite. *Physical Review B*, 103(10):104303, 2021.
- [57] Francesco Randi, Ignacio Vergara, Fabio Novelli, Martina Esposito, Martina Dell’Angela, VAM Brabers, P Metcalf, Roopali Kukreja, Hermann A Dürr, Daniele Fausti, et al. Phase separation in the nonequilibrium verwey transition in magnetite. *Physical Review B*, 93(5):054305, 2016.
- [58] B Truc, P Usai, F Pennacchio, G Berruto, R Claude, I Madan, V Sala, T LaGrange, GM Vanacore, S Benhabib, et al. Ultrafast generation of hidden phases via energy-tuned electronic photoexcitation in magnetite. *arXiv preprint arXiv:2210.00070*, 2022.
- [59] H Schwenk, S Bareiter, C Hinkel, B Lüthi, Z Kakol, A Kosłowski, and JM Honig. Charge ordering and elastic constants in  $\text{Fe}_{3-x}\text{Zn}_{xx}\text{O}_4$ . *The European Physical Journal B-Condensed Matter and Complex Systems*, 13(3):491–494, 2000.
- [60] Oh - point group character tables. Webpage. URL <https://www.webqc.org/symmetrypointgroup-oh.html>.
- [61] S De Jong, R Kukreja, Christoph Trabant, N Pontius, CF Chang, T Kachel, Martin Beye, Florian Sorgenfrei, CH Back, B Bräuer, et al. Speed limit of the insulator-metal transition in magnetite. *Nature materials*, 12(10):882–886, 2013.
- [62] Simone Borroni, Edoardo Baldini, Vamshi M Katukuri, Andreas Mann, Krzysztof Parlinski, Dominik Legut, Christopher Arrell, Frank van Mourik, Jérémie Teyssier, Andrzej Kozłowski, et al. Coherent generation of symmetry-forbidden phonons by light-induced electron-phonon interactions in magnetite. *Physical Review B*, 96(10):104308, 2017.
- [63] Pablo Maldonado, Karel Carva, Martina Flammer, and Peter M Oppeneer. Theory of out-of-equilibrium ultrafast relaxation dynamics in metals. *Physical Review B*, 96(17):174439, 2017.
- [64] L Perfetti, PA Loukakos, M Lisowski, U Bovensiepen, H Eisaki, and M Wolf. Ultrafast electron relaxation in superconducting  $\text{Bi}_2\text{Sr}_2\text{CaCu}_2\text{O}_{8+\delta}$  by time-resolved photoelectron spectroscopy. *Physical review letters*, 99(19):197001, 2007.

- [65] Fabrizio Carbone, Ding-Shyue Yang, Enrico Giannini, and Ahmed H Zewail. Direct role of structural dynamics in electron-lattice coupling of superconducting cuprates. *Proceedings of the National Academy of Sciences*, 105(51):20161–20166, 2008.
- [66] Barbara Mansart, José Lorenzana, Andreas Mann, Ahmad Odeh, Mariateresa Scarongella, Majed Chergui, and Fabrizio Carbone. Coupling of a high-energy excitation to superconducting quasiparticles in a cuprate from coherent charge fluctuation spectroscopy. *Proceedings of the National Academy of Sciences*, 110(12):4539–4544, 2013.
- [67] Barbara Mansart, Mathieu JG Cottet, Thomas J Penfold, Stephen B Dugdale, Riccardo Tediosi, Majed Chergui, and Fabrizio Carbone. Evidence for a peierls phase-transition in a three-dimensional multiple charge-density waves solid. *Proceedings of the National Academy of Sciences*, 109(15):5603–5608, 2012.
- [68] E Pachoud, J Cumby, G Perversi, JP Wright, and JP Attfield. Site-selective doping of ordered charge states in magnetite. *Nature Communications*, 11(1):1671, 2020.
- [69] S Borroni, GS Tucker, U Stuhr, J Lorenzana, HM Rønnow, and F Carbone. Energy domain versus time domain precursor fluctuations above the verwey transition in magnetite. *Physical Review B*, 101(5):054303, 2020.
- [70] Ayca Yurtsever and Ahmed H Zewail. 4d nanoscale diffraction observed by convergent-beam ultrafast electron microscopy. *Science*, 326(5953):708–712, 2009.





# PAOLO USAI

Rue Pré-du-Marché 23, 1004 Lausanne Switzerland · +41 78 834 60 53  
[paolo.usai@epfl.ch](mailto:paolo.usai@epfl.ch)

## EDUCATION

**SEPT. 2018-march 2023**

**PhD in Physics**, ÉCOLE POLYTECHNIQUE FÉDÉRALE DE LAUSANNE (EPFL), SWITZERLAND

Thesis theme: Growth and investigation of Argon thin films adsorbed on graphite by means of Ultrafast Electron Diffraction  
Laboratory for Ultrafast Microscopy and Electron Scattering (LUMES), Prof. Fabrizio Carbone

**MARCH 2018**

**Master of Science in Physics**, UNIVERSITÀ DEGLI STUDI DI CAGLIARI (UNICA), ITALY

Thesis theme: Characterization of 2D perovskites with time resolved ultrafast techniques  
Photonics and Optoelectronics Lab, Prof. Michele Saba

**MARCH 2014**

**Bachelor of Science in Physics**, UNIVERSITÀ DEGLI STUDI DI CAGLIARI, ITALY

Thesis theme: CdS\CdSe systems for photocatalysis  
Photonics and Optoelectronics Lab, Prof. Michele Saba

## SKILLS

- Supervision and management of laboratory projects for master and bachelor students
- Operation and maintenance of Ultrafast Electron Diffraction setup, including handling of magnetic optics, electron guns with HV sources, RF cavity for temporal compression
- Participation in several beamtimes in ultrafast X-Ray techniques (Synchrotron and Free Electron Laser facilities, X-Ray Diffraction, Absorption and Emission)
- Work with CCD detectors, phosphor screens, gated MCPs and Hybrid-pixel detectors
- Experience in operation, assembly and maintenance of UHV systems, dry and fluid
- Experience in cryogenics, handling of LN<sub>2</sub> and LHe, open cycle cryostats, wiring and positioning of sensors
- Experience in assembling, customizing and aligning optical components and beam paths, including 2<sup>nd</sup> and 3<sup>rd</sup> harmonic generation
- Operation of CW and ns diode lasers in visible range, up to 40W
- Design and assembly of basic analog and digital circuits, soldering on PCBs, extensive experience with Arduino systems and CNC automation and sensors
- Software-Hardware integration with different protocols, serial, ethernet, USB
- Flexibility and quick-learning skills in programming languages: Python (including GUI), C, C++, Fortran, Igor,

- Proficiency in CAD software, part design, drawing, dimensioning and rendering
- Basic machining ability, turning, drilling, tapping, filing and polishing, knowledge of machinery such as lathes and mills
- Experience in handling and maintaining computer hardware and software, extensive experience in Windows and Linux systems, virtual machine environments

## TEACHING

- **Teaching assistant**  
EPFL, assistant to exercise classes and lab for physics bachelor courses
- **Teaching assistant**  
UniCa, designer and assistant to lab experiments for physics bachelor courses

## PUBLICATIONS

- B. Truc\*, P. Usai\*, F. Pennacchio, G. Berruto, R. Claude, I. Madan, S. Benhabib, G. M. Vanacore, T. LaGrange and F. Carbone, "Ultrafast generation of hidden phases via energy-tuned electronic photoexcitation in magnetite", *in preprint*  
\*equal contributors
- P. Usai, R. Claude, S. Benhabib, T. LaGrange and F. Carbone, "Growth and investigation of Argon thin films adsorbed on graphite by means of Ultrafast Electron Diffraction", *in preparation*

## CONFERENCES

- Joint annual meeting SPS-ÖPG  
Poster contribution: "Deposition and imaging of Ar layers on graphite with electron diffraction", Innsbruck, Austria, September 2021
- MUST Annual meeting 2021  
Poster contribution: "Deposition and imaging of Ar layers on graphite with electron diffraction", Grindelwald, Switzerland, September 2021

## ACTIVITIES

Until now, I always managed to partially overlap my passions with my work allowing me to grow on both sides and improve my work environment. I developed interests in: mechanics, machining, robotics, programming, hardware and software, astronomy, astrophysics and astrophotography, analog and digital electronics; I've become adaptable to different environments and methods to achieve the same result, looking for the most suitable solutions to the conditions of the moment.